Phenomenology of Higgs Bosons in QCD at the LHC

Alexander Pedersen Lind

September 2021

A thesis submitted for the degree of

Doctor of Philosophy

University of Sussex

Department of Physics and Astronomy

Declaration

I hereby declare that this thesis has not been and will not be, submitted in whole or in part to another University for the award of any other degree.

Signature:

Alexander Lind

University of Sussex

Alexander Pedersen Lind, Doctor of Philosophy

Phenomenology of Higgs Bosons
in QCD at the LHC

Abstract

This thesis presents two phenomenological research projects focusing on the nature of Higgs bosons in quantum chromodynamics and tool building for precision studies of the Standard Model and beyond at the Large Hadron Collider.

The first project presents H1jet, a fast and easy-to-use program that computes the total cross-section and differential distribution in the transverse momentum of a colour singlet. In its current version, the program implements only leading-order $2 \to 1$ and $2 \to 2$ processes, but could be extended to higher orders. H1jet can be used by theorists to quickly assess deviations of selected new physics models from the Standard Model behaviour, and quickly obtain distributions of relevance for Standard Model phenomenology.

The second project presents a detailed study of Higgs interference effects at next-to-leading-order in the 1-Higgs-singlet extension of the Standard Model for the process $pp\ (\to \{h_1, h_2\}) \to t\bar{t} + X$. The interference effects have been studied for different benchmark points with heavy Higgs masses in the range 700–3000 GeV. For this purpose, `gghtt`, a parton-level NLO Monte Carlo event generator, has been developed, making it possible to study the interference effect between tree-level and loop-induced processes at NLO. Future versions of `gghtt` can easily be generalised to work for any loop-induced process.

Acknowledgements

A lot of people have helped and supported me during my PhD, and I am extremely grateful to all of them.

First I would like to thank my supervisor, Andrea Banfi, for all of his help, support, and encouragement. I am grateful for all the things that I have learned from the many enjoyable discussions we have had.

I would like to thank Jonas M. Lindert for his invaluable support with OpenLoops and all of his useful suggestions and guidance.

I would like to thank Nikolas Kauer for all of his help and advice, and for introducing me to many new concepts.

Thanks to Ryan Wood for his assistance in validating some of the code, and our enjoyable talks.

I am grateful to the Science and Technology Facilities Council (STFC) for studentship funding and the Doctoral School at the University of Sussex for additional financial support.

I am thankful to the Theoretical Particle Physics (TPP) group at the University of Sussex, and the Theoretical Particle Physics group and the Department of Physics at Royal Holloway, University of London for welcoming me so warmly.

Throughout the last four years I have met countless of wonderful people who have helped in making my time as a PhD student an unforgettable experience. I am thankful to all of them.

And last but absolutely not least, I would like to extend my deepest gratitude to my Mom and Dad for all of their love and support. I dedicate this thesis to them.

Contents

1 Introduction **1**
1.1 Thesis Outline . . . 3

2 The Standard Model **4**
2.1 The Standard Model Lagrangian . . . 4
2.1.1 Quantum Chromodynamics . . . 4
2.1.2 Electroweak Theory . . . 5
2.1.3 The Higgs Mechanism . . . 7
2.1.4 Renormalisation . . . 9
2.2 Feynman Rules . . . 9
2.2.1 Propagators . . . 10
2.2.2 Interactions . . . 11
2.3 Beyond the Standard Model . . . 12
2.3.1 Effective Field Theory . . . 13

3 Theoretical Predictions at the LHC **15**
3.1 Cross-Sections . . . 15
3.2 Kinematical Observables . . . 16
3.3 Resonance Particles . . . 17
3.3.1 The Breit–Wigner Line Shape . . . 18
3.3.2 The Narrow-Width-Approximation . . . 19
3.4 Interference Effects . . . 20
3.5 Next-to-Leading-Order Technology . . . 20
3.6 One-Loop Calculations . . . 21
3.6.1 Reduction of One-Loop Integrals . . . 22
3.6.2 Form Factor Representation . . . 24
3.7 Dipole Subtraction . . . 24
3.7.1 The Local Counterterm . . . 25
3.7.2 Integrated Counterterms . . . 27
3.8 Beyond Next-to-Leading-Order . . . 28

4 Phenomenology at Hadron Colliders **29**
4.1 Physical Picture of Hadronic Interactions 29
4.2 Parton Distribution Functions 31
4.3 The Factorisation Theorem 33
4.4 Phase Space Integration 34
4.4.1 The Monte Carlo Method 35

5 H1JET, a Fast Program to Compute p_T Distributions **38**
5.1 Motivation 38
5.2 The Method 40
5.3 Implemented Models 43
5.3.1 CP-Even and CP-Odd Higgs Production 44
5.3.2 Simplified SUSY 45
5.3.3 Simplified Top-Partner Model 45
5.3.4 Explicit Top-Partner Model 46
5.3.5 Multiple Top-Partners 47
5.4 Implementation of Scalar Integrals 47
5.4.1 Bubbles 48
5.4.2 Triangles 49
5.4.3 Boxes 49
5.5 Technical Details 51
5.5.1 Adaptive Gaussian Quadrature Integration 51
5.6 Validation 52
5.7 Adding New Processes to H1JET 53
5.7.1 Example: Axion-Like-Particle Effective Theory 53
5.8 Current Version and Future Plans 58

6 Higgs Interference Effects at NLO in the 1-Higgs-Singlet Model **60**
6.1 Motivation 60
6.2 The 1-Higgs-Singlet Model 63
6.3 NLO QCD Corrections to the Interference 65
6.4 `gghtt`, a NLO Monte Carlo Event Generator 68
6.4.1 Phase Space Generation with KALEU 69
6.4.2 Dipole Subtraction with HELAC-DIPOLES 69
6.4.3 OPENLOOPS Interface 71
6.4.4 Form Factors for Gluon-Fusion Higgs Production 72

6.5 Calculational Details . . . 76
6.5.1 Higgs Decay Widths . . . 76
6.5.2 Numerical Stability . . . 78
6.6 Validation . . . 79
6.7 Results and Discussion . . . 81
6.7.1 Integrated Cross-Sections . . . 81
6.7.2 Differential Distributions . . . 85
6.7.3 Significance Estimations . . . 96
6.7.4 Theoretical Uncertainties from Scale Variations . . . 97
6.8 Conclusion and Outlook . . . 98
6.8.1 Decays of the Top and Anti-Top Quarks . . . 100
6.8.2 Dipole Subtraction for Intermediate Emitters . . . 101
6.8.3 Spin Correlations in the Top Decays . . . 102
6.8.4 Generalising and Extending `gghtt` . . . 103

7 Concluding Remarks **105**

A Manual for `gghtt` **107**
A.1 Dependencies . . . 107
A.2 Installation . . . 108
A.3 Usage . . . 108

B Standard Model Distributions for $t\bar{t}$ Production **111**

C Additional Results for the 1HSM **113**

Bibliography **122**

1

Introduction

The current state of particle physics is not unlike that of chemistry in the 19^{th} century. Chemists knew of the existence of several chemical elements which were placed in a periodic table along with their properties, such as their mass and the way they reacted with each other. However, they were unable to explain why those exact elements existed, why they had the properties they did, and why they reacted in the manners that was observed. Some unsuccessful attempts were made to shed light on the underlying mechanisms, but it wasn't until the beginning of the 20^{th} century, with the advent of atomic theory, quantum mechanics, and subatomic physics, when researchers went further down in scale, that a deeper understanding was reached. However, the careful work of the chemists in the 1800s to discover and categorise the chemical elements was not in vain [1]. Indeed one could argue that each level of the hierarchical structure in science brings about its own fundamental laws [2].

Today, it is known that the chemical elements are atoms consisting of a nucleus with a specific number of protons and neutrons depending on the element and the isotope. The protons and neutrons, in turn, consists of quarks and gluons, collectively known as *partons*. All discovered fundamental particles, such as the partons, along with their interactions make up the *Standard Model* (SM) of particle physics. The theoretical and mathematical framework to explain the SM is *quantum field theory* (QFT). Alas, QFT is descriptive, not explanatory. The particles and their properties are input to the theory – QFT and the SM are unable to explain their origin. Attempts at explaining the underlying structure of the observed fundamental particles have been made. String theory is one such attempt but has its problems [3].

Until a new, more fundamental theory is discovered, the role of the modern particle physicist is to explore the properties and interactions of the known particles, and to theorise, discover, and categorise potential new particles.

The latest addition to the SM was the *Higgs boson*. In 2012, the ATLAS and CMS experiments at the Large Hadron Collider (LHC) at CERN discovered a scalar boson with a mass of 125 GeV [4, 5]. This new boson seems to be consistent with the Higgs boson predicted by the Higgs mechanism [6–10], which explains the generation of mass for the electroweak gauge bosons in a gauge invariant way through electroweak symmetry breaking.

Many *Beyond the Standard Model* (BSM) extensions to the SM Higgs sector exists, adding extra scalar particles to the theory. Additional scalars can explain a large variety of hypothetical new physics, such as supersymmetry, dark matter, and axions among others. However, beyond the Higgs discovery, there has been little sign of new physics at the LHC.

The next 15 years of the LHC program is going to see an increase in the integrated luminosity, resulting in more data, allowing for precision tests of the SM as a search tool for new physics. Very heavy particles that are beyond direct detection of current detectors will still have an impact on SM processes, which can be discerned in precision studies. A lot of interesting new physics extensions to the SM maps nicely to *effective field theories* (EFTs), which can provide a powerful tool to translate theoretical effects and deviations of new physics models onto current experimental hadron colliders.

The current precision era in which particle physics finds itself calls for new phenomenological tools. This thesis presents two new versatile tools, allowing one to easily study new physics models in the form of EFTs, with a specific focus on Higgs phenomenology and the nature of electroweak symmetry breaking.

The first tool, H1JET, allows quick and easy computation of the total cross-section and differential distribution in the transverse momentum of a colour singlet in $2 \to 1$ and $2 \to 2$ processes. H1JET can be used to assess deviations of selected new physics models from the SM behaviour, and can quickly obtain distributions of relevance for precision phenomenology. The current version of H1JET comes with several built-in models, but can easily be extended with a provided user interface.

The second tool, `gghtt`, is a parton-level Monte Carlo event generator at NLO, which is particularly well suited for computing the interference between tree-level and loop-induced processes – something that is missing from the current event generator landscape. The current version of `gghtt` has been used to study Higgs interference

effects at NLO in the process $pp\,(\to\{h_1,h_2\})\to t\bar{t}+X$ in the 1-Higgs-singlet model (1HSM), the results of which are presented in this thesis. However, `gghtt` can easily be generalised to work for any loop-induced process.

1.1 Thesis Outline

This thesis presents two phenomenological research projects focusing on the nature of the Higgs boson, with a focus on tool building for precision studies of the SM and beyond at current and future collider experiments.

Chapter 2 gives a brief description of the Standard Model, its success, and its shortcomings.

Chapter 3 introduces some concepts and tools for theoretical predictions at the LHC, in particular with a focus on higher-order corrections.

Chapter 4 provides an overview of the physics and phenomenology of the proton–proton collisions that happens at the LHC.

Chapter 5 presents H1JET, a fast program for computing the transverse momentum distribution of a colour singlet in $2\to1$ and $2\to2$ processes. H1JET comes with several built-in processes and models, but can easily be extended.

Chapter 6 presents a study on Higgs interference at next-to-leading-order (NLO) for the process $pp\,(\to\{h_1,h_2\})\to t\bar{t}+X$ in the 1HSM for a light and heavy Higgs boson. For this purpose, `gghtt`, a new parton-level NLO Monte Carlo event generator has been developed, which can be generalised to work for any loop-induced process.

Finally, chapter 7 provides concluding remarks on the results and discussions presented in this thesis.

2

The Standard Model

The Standard Model (SM) of particle physics is a commonly accepted, widely successful, and renormalisable quantum field theory describing the fundamental particles and their interactions.

The *gauge group* of the SM is the direct product of three groups,

$$\mathrm{SU}(3)_C \times \mathrm{SU}(2)_L \times \mathrm{U}(1)_Y \,, \tag{2.1}$$

where the subscripts C, L, and Y denotes colour, the left-handed chiral representation, and hypercharge respectively. The $\mathrm{SU}(3)_C$ factor gives rise to the *strong interactions*, while the $\mathrm{SU}(2)_L \times \mathrm{U}(1)_Y$ factor gives rise to the *electroweak sector* of the SM, unifying the *electromagnetic* and *weak interactions*.

The SM has 19 free parameters which are being experimentally determined with increasing precision. These include three charged lepton masses, six quark masses, three CKM mixing angles and a CP violation phase, three gauge couplings, the QCD vacuum angle, and the Higgs mass and vacuum expectation value.

The content of this chapter is based on refs. [11] and [12], unless otherwise noted.

2.1 The Standard Model Lagrangian

2.1.1 Quantum Chromodynamics

Quantum chromodynamics (QCD) is a non-Abelian gauge theory describing the strong interaction between quarks and gluons. QCD corresponds to the $\mathrm{SU}(3)_C$

component of the full SM gauge group.

The first ingredient of the SM Lagrangian is the QCD part with massless quarks, given by

$$\mathcal{L}_{\text{QCD}} = \sum_q \bar{\psi}_{q,a} \left(i\gamma^\mu \partial_\mu \delta_{ab} - g_s \gamma^\mu t^C_{ab} G^C_\mu \right) \psi_{q,b} - \frac{1}{4} G^A_{\mu\nu} G^{A\,\mu\nu} \,, \tag{2.2}$$

where Einstein notation is used, and where γ^μ are the gamma matrices which satisfy the anti-commutation relations $\{\gamma^\mu, \gamma^\nu\} = 2g^{\mu\nu}$.

The $\psi_{q,a}$ is the quark field for flavour q, with mass m_q, and colour a. The quark colour index runs from $1, \ldots, N_c$, with $N_c = 3$.

The field strength tensor $G^A_{\mu\nu}$ is derived from the gluon field G^A_μ and is given by

$$G^A_{\mu\nu} = \partial_\mu G^A_\nu - \partial_\nu G^A_\mu - g_s f_{ABC} G^B_\mu G^C_\nu \,, \tag{2.3}$$

where the indices A, B, and C run over the eight colour degrees of freedom of the gluon field. The third term of Eq. (2.3) includes f_{ABC}, the structure constants of the $\mathrm{SU}(3)_C$ symmetry group, and gives rise to triplet and quartic self-interactions of the gluon. The gluons are massless – indeed, any gluon mass term on the form $m^2 G^\mu G_\mu$ will not be gauge invariant. The representation matrices t^A of $\mathrm{SU}(3)_C$ can be written in terms of the eight Gell-Mann matrices.

The coupling constant $\alpha_s = g_s^2/(4\pi)$ determines the strength of the strong interaction. The strong coupling is a so-called *running coupling*, $\alpha_s(\mu_R^2)$ as a function of the unphysical renormalisation scale μ_R, satisfying the renormalisation group equation with its perturbative expansion,

$$\mu_R^2 \frac{\mathrm{d}\alpha_s}{\mathrm{d}\mu_R^2} = \beta(\alpha_s) = -\left(\beta_0 \alpha_s^2 + \beta_1 \alpha_s^3 + \beta_2 \alpha_s^4 + \ldots \right) \,, \tag{2.4}$$

where β_0, β_1, and β_2 are the 1-, 2-, and 3-loop coefficients. The sign of β_0 is crucial to ensure the asymptotic freedom of QCD, i.e. that the coupling strength decreases with energy, making the use of perturbation theory possible.

2.1.2 Electroweak Theory

The electroweak (EW) interaction is the unified theory of the electromagnetic interaction, described by *quantum electrodynamics* (QED), and the weak interaction. The electroweak theory corresponds to the $\mathrm{SU}(2)_L \times \mathrm{U}(1)_Y$ component of the SM

gauge group. The full Lagrangian for the electroweak sector takes the form

$$\mathcal{L}_{\text{EW}} = \mathcal{L}_{\text{Gauge}} + \mathcal{L}_{\text{Fermions}} + \mathcal{L}_{\text{Higgs}} + \mathcal{L}_{\text{Yukawa}} \,. \tag{2.5}$$

The gauge part of the Lagrangian is

$$\mathcal{L}_{\text{Gauge}} = -\frac{1}{4} W^i_{\mu\nu} W^{i,\,\mu\nu} - \frac{1}{4} B_{\mu\nu} B^{\mu\nu} \,, \tag{2.6}$$

with the field strength tensors

$$W^i_{\mu\nu} = \partial_\mu W^i_\nu - \partial_\nu W^i_\mu - g_W \varepsilon^{ijk} W^j_\mu W^k_\nu \,, \tag{2.7}$$

$$B_{\mu\nu} = \partial_\mu B_\nu - \partial_\nu B_\mu \,, \tag{2.8}$$

where W^i_μ $(i = 1, 2, 3)$ is the $\mathrm{SU}(2)_L$ gauge field, and B_μ is the $\mathrm{U}(1)_Y$ gauge field associated with the hypercharge Y. The group structure constants ε^{ijk} corresponds to the totally antisymmetric Levi-Civita symbol for $\mathrm{SU}(2)_L$. The physical fields for the massive weak gauge bosons $W^\pm$ and Z, and the massless photon are linear combinations,

$$W^\pm_\mu = \frac{1}{\sqrt{2}} \left(W^1_\mu \mp i W^2_\mu \right) \,, \tag{2.9}$$

$$Z_\mu = \cos\theta_W W^3_\mu - \sin\theta_W B_\mu \,, \tag{2.10}$$

$$A_\mu = \sin\theta_W W^3_\mu + \cos\theta_W B_\mu \,, \tag{2.11}$$

with the *Weinberg angle* (or the *weak mixing angle*) defined as

$$\cos\theta_W = \frac{g_W}{\sqrt{g'^2 + g_W^2}} \,, \qquad \sin\theta_W = \frac{g'}{\sqrt{g'^2 + g_W^2}} \,. \tag{2.12}$$

Here g' and g_W are the coupling constants of $\mathrm{U}(1)_Y$ and $\mathrm{SU}(2)_L$ respectively, related to the elementary electric charge through $e = \frac{g' g_W}{\sqrt{g'^2 + g_W^2}}$.

The Lagrangian for the fermion fields is summed over three fermion generations,

$$\mathcal{L}_{\text{Fermions}} = \sum_{j=1}^{3} \left[i \bar{\psi}_{j,L} \gamma^\mu D_\mu \psi_{j,L} + i \bar{\psi}_{j,R} \gamma^\mu D_\mu \psi_{j,R} \right] \,, \tag{2.13}$$

for left- and right-handed fermions, ψ_L and ψ_R, with the gauge-covariant derivative

$$D_\mu = \partial_\mu + ig_W T_L^i W_\mu^i + ig' \frac{Y}{2} B_\mu \,, \tag{2.14}$$

where $T_L^i = \sigma^i/2$ are the three generators of the $\mathrm{SU}(2)_L$ gauge symmetry, with σ^i being the 2×2 Pauli matrices, only acting on left-handed fermions.

In order to allow mass terms for the $W^\pm$ and Z gauge bosons, the EW subgroup $\mathrm{SU}(2)_L \times \mathrm{U}(1)_Y$ has to be *spontaneously broken* in a gauge invariant way. This is done via the *Higgs mechanism*, introducing the scalar part $\mathcal{L}_{\text{Higgs}}$ and the Yukawa interactions $\mathcal{L}_{\text{Yukawa}}$ to Eq. (2.5), which will be described in the next section.

2.1.3 The Higgs Mechanism

The Higgs mechanism generates the masses of the electroweak gauge bosons in a way that preserves the local gauge invariance of the SM. In the Higgs mechanism, a complex scalar doublet,

$$\phi \equiv \begin{pmatrix} \phi^+ \\ \phi^0 \end{pmatrix} = \frac{1}{\sqrt{2}} \begin{pmatrix} \phi_1 + i\phi_2 \\ \phi_3 + i\phi_4 \end{pmatrix} \,, \tag{2.15}$$

is added with the Lagrangian,

$$\mathcal{L}_{\text{Higgs}} = (D_\mu \phi)^\dagger \, (D^\mu \phi) - V(\phi) \,, \tag{2.16}$$

and with the Higgs potential,

$$V(\phi) = -\mu^2 \phi^\dagger \phi + \lambda \left(\phi^\dagger \phi \right)^2 \,, \tag{2.17}$$

where μ^2 is the mass parameter of the Higgs doublet and the quartic parameter λ gives rise to self-interactions of the Higgs boson. For $\mu^2 < 0$, the Higgs potential has an infinite set of degenerate minima satisfying the vacuum condition

$$\phi^\dagger \phi = \frac{v^2}{2} = -\frac{\mu^2}{2\lambda} \,, \tag{2.18}$$

spontaneously breaking the electroweak gauge symmetry, where the Higgs doublet ϕ acquires a *vacuum expectation value* (VEV), $v \approx 246$ GeV,

$$\langle \phi \rangle = \frac{1}{\sqrt{2}} \begin{pmatrix} 0 \\ v \end{pmatrix} , \tag{2.19}$$

This leaves a massive scalar and three massless Goldstone bosons, the latter of which will give the longitudinal degrees of freedom of the $W^{\pm}$ and Z bosons.

After symmetry breaking, the Higgs doublet can be written in the unitary gauge as

$$\phi_{\text{unitary}} = \frac{1}{\sqrt{2}} \begin{pmatrix} 0 \\ v + H \end{pmatrix} , \tag{2.20}$$

with a physical Higgs field H. The potential in Eq. (2.17) becomes

$$V(H) = \frac{2\lambda v^2}{2} H^2 + \lambda v H^3 + \frac{\lambda}{4} H^4 + \text{const.} , \tag{2.21}$$

acquiring a mass term, leading to a physical mass given by

$$m_H = \sqrt{2\lambda} v , \tag{2.22}$$

which has been experimentally measured as $m_H = 125$ GeV [4, 5].

The covariant derivative in Eq. (2.14) acting on the Higgs doublet, will give rise to mass terms that are quadratic in the gauge boson fields. The masses of the physical electroweak gauge bosons can be identified as

$$m_W = \frac{1}{2} g_W v , \qquad m_Z = \frac{m_W}{\cos \theta_W} , \tag{2.23}$$

whereas the photon remains massless.

The VEV is related to the Fermi constant through $v = \left(\sqrt{2} G_F\right)^{-1/2}$.

Mass terms for the fermions on the form

$$\mathcal{L} \supset -m_f \bar{\psi} \psi = -m_f \left(\bar{\psi}_R \psi_L + \bar{\psi}_L \psi_R \right) , \tag{2.24}$$

violates the gauge invariance of the $\mathrm{SU}(2)_L \times \mathrm{U}(1)_Y$ gauge symmetry, due to the different transformation properties of left- and right-handed chiral states. However, the Higgs mechanism can also generate mass terms for the fermions through Yukawa interactions between the Higgs doublet ϕ in the unitary gauge and the fermion fields,

$$\mathcal{L}_{\text{Yukawa}} = -\sum_f \left[-\frac{y_f}{\sqrt{2}} v \left(\bar{\psi}_{f,L} \psi_{f,R} + \bar{\psi}_{f,R} \psi_{f,L} \right) - \frac{y_f}{\sqrt{2}} H \left(\bar{\psi}_{f,L} \psi_{f,R} + \bar{\psi}_{f,R} \psi_{f,L} \right) \right] , \tag{2.25}$$

where the first term gives the mass of the fermion from a coupling to the Higgs field through its VEV, whereas the the second term is a coupling between the fermion and the Higgs boson itself. The coupling factor y_f is referred to as a *Yukawa coupling*,

$$y_f = m_f \frac{g_W}{\sqrt{2} m_W} = \sqrt{2} \frac{m_f}{v} , \tag{2.26}$$

the value of which is not predicted by the Standard Model, but set by the experimentally measured fermion masses.

2.1.4 Renormalisation

Calculations including higher orders in perturbation theory will contain ultra-violet (UV) divergences. These divergences need to be dealt with by renormalising the theory with some scheme-dependent renormalisation scheme.

The total Standard Model Lagrangian then becomes

$$\mathcal{L}_{\text{SM}} = \mathcal{L}_{\text{QCD}} + \mathcal{L}_{\text{EW}} + \mathcal{L}_{\text{fix}} + \mathcal{L}_{\text{ghost}} , \tag{2.27}$$

with the addition of a *gauge-fixing term*, $\mathcal{L}_{\text{fix}}$, in order to handle the redundant degrees of freedom in the gauge fields for the photon, the gluons, and the $W^{\pm}$ and Z bosons. Depending on the gauge choice, it may be necessary to include *Fadeev–Popov ghosts*, $\mathcal{L}_{\text{ghost}}$, in order to cancel unphysical degrees of freedom [13].

2.2 Feynman Rules

The perturbative calculation of any process will require the use of Feynman rules which can be derived from the Lagrangian densities. The action of the theory is given in terms of the Lagrangian as

$$\mathcal{S} = \int \mathcal{L} \, \mathrm{d}^4 x \, . \tag{2.28}$$

For a free non-interacting theory, i.e. a Lagrangian with only kinetic terms, the action will lead to particle propagators in the form of two-point functions. The interaction terms, i.e. the potential terms, of the Lagrangian will lead to vertices which couples different particles to each other. The propagators and vertices of the Standard Model can be used to draw *Feynman diagrams* [14] which are pictorial representations of the contributions to the *matrix element* (or *amplitude*) $\mathcal{M}$, being the quantum mechanical probability amplitude for a given scattering interaction. Each topologically different Feynman diagram corresponds to a term in the perturbative expansion, and can be evaluated with the Feynman rules of the relevant theory.

2.2.1 Propagators

A *propagator* is the probability amplitude for a particle to propagate with a certain four-momentum. Different propagator factors exists for fermions and gauge bosons, but this section will focus on the scalar propagator for the Higgs boson as it plays an important role in this thesis.

The free-field scalar Feynman propagator in momentum space is

$$\Delta(p^2) = \quad \underset{p}{\longrightarrow} \quad = \frac{i}{p^2 - m_0^2 + i\varepsilon}\,, \tag{2.29}$$

where p is the four-momentum, and m_0 is the bare mass which appears in the Lagrangian and which generally differs from the physical observable rest mass of the particle. In order to deal with the two poles at $p_0 = \pm\sqrt{|\boldsymbol{p}|^2 + m^2}$, a term with a positive infinitesimal real number ε is introduced, such that the poles are shifted to $p_0 = \pm\sqrt{|\boldsymbol{p}|^2 + m^2} \mp i\varepsilon$.

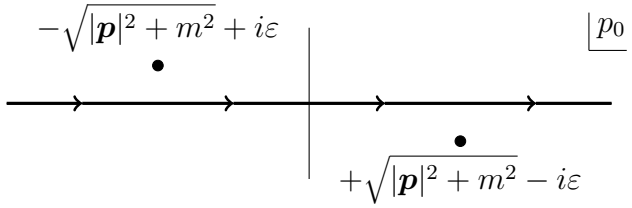

Figure 2.1. The $i\varepsilon$ shift of the two poles of the free propagator in the complex p_0 plane. The arrows indicate the contour when integrating over momentum. Drawn with Ti*k*Z [15].

For an interacting theory, it will be necessary to take quantum fluctuations of the propagator into account. The self-energy contribution of the scalar particle are

part of the Feynman diagrams that will represent the quantum corrections to the free propagator in order to acquire the exact propagator for the interacting theory. The self-energy $\Sigma(p)$ is defined as the the sum of all one-particle-irreducible (1PI) diagrams, i.e. the Feynman diagrams which cannot be split in two by cutting an internal propagator line. With this, the exact scalar propagator can then be written as a geometric series,

$\Pi(p^2) =$ 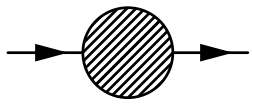

$=$ 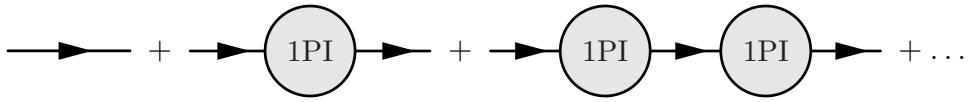

$$= \frac{i}{p^2 - m_0^2} + \frac{i}{p^2 - m_0^2}\left[-i\Sigma(p^2)\right]\frac{i}{p^2 - m_0^2} + \dots$$
$$= \frac{i}{p^2 - m_0^2 - \Sigma(p^2)}\,. \tag{2.30}$$

The exact scalar propagator has a simple pole, shifted away from m_0 by $\Sigma(p^2)$, since the self-energy may be complex.

2.2.2 Interactions

The focus of this thesis is on the nature of the Higgs boson in QCD, hence only a relevant subset of the Feynman rules of the Standard Model will be discussed here.

The interaction between gluons and quarks are generated by the QCD Lagrangian in Eq. (2.2). The Feynman rule for this vertex is shown in Figure 2.2a[1].

Self-interactions of the gluons are generated by the non-Abelian term of Eq. (2.3) leading to three- and four-point vertices as shown in Figure 2.2b and 2.2c.

Due to the Yukawa interactions in Eq. (2.25), the Higgs boson can decay to fermion pairs, $H \to f\bar{f}$, for the kinematically allowed decay channels with $m_H > 2m_f$. The Feynman rule for this decay is shown in Figure 2.3a.

Self-interactions of the Higgs boson are generated by the potential terms in Eq. (2.21), where the coupling strengths can be expressed using g_W, m_H, and m_W instead of λ and v by using Eq. (2.22) and Eq. (2.23).

The Higgs boson does not couple directly to the massless gluons. However, a Higgs boson can be produced via gluon-fusion through a loop-induced diagram with

[1] All Feynman diagrams in this thesis have been drawn using either `feynMF/feynMP` [16] or JaxoDraw [17].

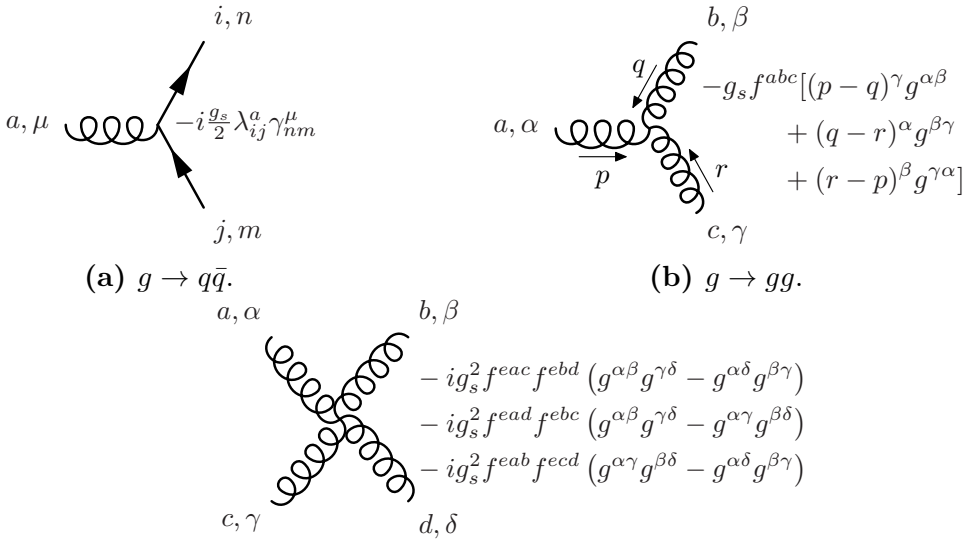

(a) $g \to q\bar{q}$. **(b)** $g \to gg$.

(c) $gg \to gg$.

Figure 2.2. Allowed QCD vertices with Feynman rules.

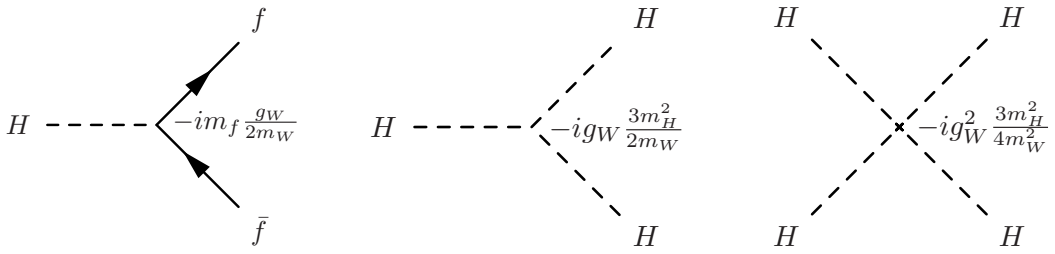

(a) $H \to f\bar{f}$. **(b)** $H \to HH$. **(c)** $HH \to HH$.

Figure 2.3. Some allowed vertices with Feynman rules for the Higgs boson.

a heavy quark loop. This will be discussed in detail later in subsection 3.6.2 and subsection 6.4.4.

2.3 Beyond the Standard Model

The Standard Model has been widely successful in describing experimental results at particle colliders. The discovery of the Higgs boson and recent precision tests of the Standard Model at energies up to the electroweak scale at the LHC have firmly established the validity of the theory. Despite this success, the Standard Model is known to be incomplete, and there are many unanswered questions, including:

- The nature, and possible particle composition, of *dark matter* is still unknown.
- Several *fine tuning* problems exists, such as the *strong CP problem* which can

be resolved by a hypothetical axion field.

- A complex Higgs doublet is the simplest choice for the Higgs mechanism, but is not unique. Several models exists that extends the Higgs sector with additional scalars.

- *Composite Higgs models* explore the possibility that the Higgs is not a fundamental particle, but instead is a bound state in a new strongly interacting sector.

- *Supersymmetry* (SUSY) is a symmetry that relates fermions and bosons, giving rise to supersymmetric partners. As of yet, none of the hypothetical supersymmetric partners have been discovered.

This list is far from exhaustive as there are many other known shortcomings of the SM, the lack of a consistent description of gravity being perhaps the most notable. However, the mentioned topics are particular suited for *Beyond the Standard Model* (BSM) extensions to the Higgs sector and the mechanism behind electroweak symmetry breaking, which is the subject of this thesis.

2.3.1 Effective Field Theory

BSM models can be, with great benefit, mapped onto *effective field theories* (EFTs). An EFT is a framework, based on the idea that short and long-distance physics can be decoupled, for which the Lagrangian can be expanded in powers of operator dimensions [18],

$$\mathcal{L}_{\text{EFT}} = \sum_{D,i} \frac{c_i^{(D)}}{\Lambda^{D-4}} \mathcal{O}_i^{(D)} = \sum_{D} \frac{\mathcal{L}^{(D)}}{\Lambda^{D-4}} \,, \tag{2.31}$$

where $c_i^{(D)}$ are the Wilson coefficients corresponding to the operators $\mathcal{O}_i^{(D)}$ of dimension D. The operators will be effective convolutions of different particle fields. Hence, the EFT Lagrangian is an infinite series in terms of increasing operator dimension expanded in powers of $1/\Lambda$,

$$\mathcal{L}_{\text{EFT}} = \mathcal{L}_{\text{SM}} + \frac{\mathcal{L}^{(5)}}{\Lambda} + \frac{\mathcal{L}^{(6)}}{\Lambda^2} + \dots \,, \tag{2.32}$$

where Λ is the short-distance energy scale where new physics shows up.

EFTs can also be used to approximate SM behaviour by integrating out higher-order corrections. As an example with utility for this thesis, in the *Higgs effective*

field theory (HEFT) the dimension-5 effective Lagrangian for gluon-fusion Higgs production, $gg \to H$, is

$$\mathcal{L}^{(5)}_{\text{HEFT}} \supset \frac{\alpha_s}{12\pi}\frac{H}{v}G^A_{\mu\nu}G^{A\,\mu\nu}\,, \tag{2.33}$$

which is a valid approximation for $m_H \ll m_t$, resulting in an effective tree-level gluon-gluon-Higgs coupling [19, 20]. EFTs are powerful tools that facilitates the application of higher-order corrections and BSM models at hadron colliders.

3

Theoretical Predictions at the LHC

This chapter will introduce some relevant concepts and calculational tools for theoretical predictions of cross-sections at the LHC, in particular with a focus on higher-order corrections.

3.1 Cross-Sections

The relevant measure of the quantum mechanical interaction probability of any given particle scattering is the *cross-section* σ defined as [12]

$$\sigma = \frac{\text{number of interactions per unit time per target particle}}{\text{incident flux}}, \tag{3.1}$$

with the units of an area, usually barn, 1 b $= 10^{-28}$ m^2. The cross-section will be proportional to the process-specific squared matrix element, $\sigma \propto |\mathcal{M}|^2 = \mathcal{M}^*\mathcal{M}$.

Besides the total cross-section, the distributions with respect to some kinematical variables are also of interest. The *differential* cross-section corresponding to an observable $\mathcal{O}$ is defined as

$$\frac{\mathrm{d}\sigma}{\mathrm{d}\mathcal{O}} = \frac{\text{number of particles scattered in } \mathrm{d}\mathcal{O} \text{ per unit time per target particle}}{\text{incident flux}}, \tag{3.2}$$

where the integral over the differential cross-section gives the total cross-section,

$$\sigma = \int \frac{\mathrm{d}\sigma}{\mathrm{d}\mathcal{O}} \, \mathrm{d}\mathcal{O} \, . \tag{3.3}$$

3.2 Kinematical Observables

This section introduces the relevant kinematical observables that are usually considered in phenomenological studies. See section 7.4 of ref. [21] for more details.

The four-momenta of a particle is usually written as

$$p^\mu = (E, \mathbf{p}) = (E, p_x, p_y, p_z) \ , \tag{3.4}$$

however it is often simply denoted by p, without the index. The coordinate system is aligned such that the longitudinal p_z component is along the beam axis in collider experiments. For a time-like metric with signature $(+,-,-,-)$, the square of the four-momenta is

$$p^2 = p^\mu p_\mu = p^\mu p^\nu g_{\mu\nu} = E^2 - \mathbf{p}^2 = m^2 \, , \tag{3.5}$$

where m is the mass.

For a system of n particles, the sum of the four-momenta,

$$p^\mu = \sum_{i=1}^{n} p_i^\mu \, , \tag{3.6}$$

is also a four-vector, from which the squared *invariant mass* can be defined as

$$M^2 = \left(\sum_{i=1}^{n} E_i \right)^2 - \left(\sum_{i=1}^{n} \mathbf{p}_i \right)^2 \, . \tag{3.7}$$

Hence, the invariant mass of a system of decay products is equal to the mass of the decayed particle.

The *transverse momentum* p_T is defined as

$$p_T = \sqrt{p_x^2 + p_y^2} \, . \tag{3.8}$$

The *transverse mass* m_T is defined as

$$m_T = \sqrt{m^2 + p_x^2 + p_y^2} = \sqrt{m^2 + p_T^2} \, . \tag{3.9}$$

The *rapidity* y is defined as

$$y = \frac{1}{2} \ln \left(\frac{E + p_z}{E - p_z} \right) = \ln \left(\frac{E + p_z}{m_T} \right) . \tag{3.10}$$

For massless particles, the rapidity will be equal to the *pseudorapidity* η, which can be written in terms of the *scattering* (or *polar*) *angle* θ,

$$\eta = \frac{1}{2} \ln \left(\frac{|\mathbf{p}| + p_z}{|\mathbf{p}| - p_z} \right) = \ln \left(\frac{|\mathbf{p}| + p_z}{p_T} \right) = - \ln \left[\tan \left(\frac{\theta}{2} \right) \right] , \tag{3.11}$$

where $p_z = |\mathbf{p}| \cos \theta$ has been used.

Note that rapidity y is not Lorentz-invariant, but the difference in rapidity, Δy, is invariant under longitudinal boosts,

$$y_2' - y_1' = y_2 - y_1 . \tag{3.12}$$

This is however not the case, in general, for differences in pseudorapidity, $\Delta \eta$,

$$\eta_2' - \eta_1' \neq \eta_2 - \eta_1 . \tag{3.13}$$

The rapidity (or pseudorapidity) is often paired with the *azimuthal angle* ϕ, to create a coordinate pair (y, ϕ), or the purely angular (η, ϕ). Using this, an angular distance ΔR between two objects can be defined as

$$\Delta R = \sqrt{(\Delta \eta)^2 + (\Delta \phi)^2} , \tag{3.14}$$

which is invariant under longitudinal boosts for massless particles.

Hard scattering QCD-only matrix elements will generally dominate at the LHC and be steeply falling for increasing invariant mass M. However, BSM models will often introduce heavy resonances that gives rise to Breit–Wigner line shapes in large M regions.

3.3 Resonance Particles

The notion of a particle is most commonly assigned to stable entities, such as electrons and photons, which can travel for sufficiently large time scales in order to be detected experimentally by particle detectors. However, a lot of known unstable particles

exists, also known as *resonances*, which decays before any direct measurement can be performed. This section will introduce the commonly used descriptions of heavy resonances.

3.3.1 The Breit–Wigner Line Shape

The exact scalar propagator was given in Eq. (2.30) to all orders as

$$\Pi(p^2) = \frac{i}{p^2 - m_0^2 - \Sigma(p^2)} \,. \tag{3.15}$$

For a stable particle with $\Gamma = 0$, the self-energy $\Sigma(p^2)$ is a real number, and the location of the pole is the physical scalar mass m,

$$m^2 = m_0^2 + \Sigma(p^2 = m^2) \,. \tag{3.16}$$

However, for an unstable particle, the self-energy will be complex. In this case, the physical mass m is defined as

$$m^2 = m_0^2 + \operatorname{Re}\Sigma(p^2 = m^2) \,. \tag{3.17}$$

From the optical theorem it can be derived that [22]

$$\operatorname{Im}\Sigma(p^2 = m^2) = -m\Gamma \,, \tag{3.18}$$

hence, the exact propagator can be approximated, in the on-shell case where $p^2 \sim m^2$ and $\Gamma \ll m$, as

$$\Pi(p^2) \sim \frac{i}{p^2 - m^2 + im\Gamma} \,. \tag{3.19}$$

In an s-channel scattering diagram, this propagator will result in a *Breit–Wigner line shape* for the cross-section,

$$\sigma \sim \left| \frac{i}{p^2 - m^2 + im\Gamma} \right|^2 = \frac{1}{(p^2 - m^2)^2 + m^2\Gamma^2} \,. \tag{3.20}$$

The Breit–Wigner line shape is shown in Figure 3.1[1]. Note that the Breit–Wigner is significantly more fat-tailed than a Gaussian distribution, and one should be careful when cutting off the distribution at $p^2 = m^2 \pm nm\Gamma$ for low values of $n \in \mathbb{N}$.

[1] All plots in this thesis have been drawn using Matplotlib [23], unless otherwise noted.

Since most unstable particles in the Standard Model are long-lived, $\Gamma \ll m$, and hence approximately on-shell, the Breit–Wigner approximation is reasonable for most resonances.

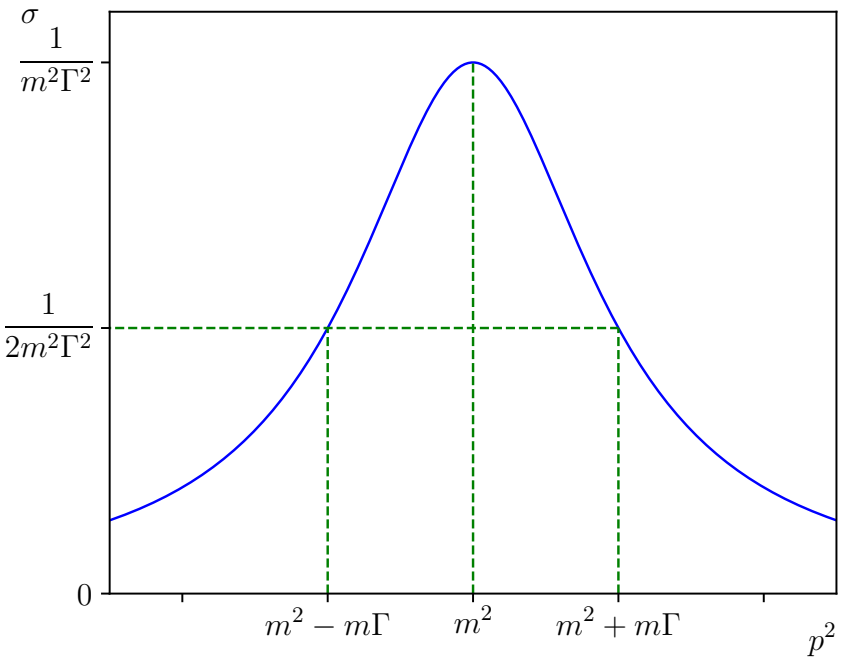

Figure 3.1. The Breit–Wigner line shape as a function of p^2. Centered at m^2 with a FWHM equal to $2m\Gamma$.

3.3.2 The Narrow-Width-Approximation

In the limit $\Gamma/m \to 0$, the Breit–Wigner line shape vanishes except near the on-shell condition $p^2 = m^2$. Hence, the Breit–Wigner resonance can be further approximated as a Dirac delta distribution,

$$\frac{1}{(p^2 - m^2)^2 + m^2\Gamma^2} \xrightarrow{\Gamma/m \to 0} \frac{\pi}{m\Gamma}\delta^{(4)}(p^2 - m^2) + \mathcal{O}\left(\frac{\Gamma}{m}\right), \tag{3.21}$$

where the normalisation was found by integrating over momentum,

$$\int_{-\infty}^{\infty} \mathrm{d}p^2 \frac{1}{(p^2 - m^2)^2 + m^2\Gamma^2} = \frac{\pi}{m\Gamma}. \tag{3.22}$$

The result in Eq. (3.21) is known as the *narrow-width-approximation (NWA)*, which applies as long as Γ/m is much smaller than the required precision.

3.4 Interference Effects

It is often the case in experimental and phenomenological analyses that one is interested in looking for a BSM process, denoted as the *signal* process, compared to the SM denoted *background* processes.

The total contribution to a process can then be written as a sum of the signal and background,

$$\mathcal{M} = \mathcal{M}_{\mathrm{S}} + \mathcal{M}_{\mathrm{B}} \,. \tag{3.23}$$

The absolute square of this matrix element will then be

$$\begin{aligned} |\mathcal{M}|^2 &= |\mathcal{M}_{\mathrm{S}} + \mathcal{M}_{\mathrm{B}}|^2 \\ &= |\mathcal{M}_{\mathrm{S}}|^2 + |\mathcal{M}_{\mathrm{B}}|^2 + 2\,\mathrm{Re}\left(\mathcal{M}_{\mathrm{S}}^* \mathcal{M}_{\mathrm{B}}\right) \,. \end{aligned} \tag{3.24}$$

The last term of Eq. (3.24) is referred to as the *interference term*. Note that, unlike the other two terms, it may be negative. It is common in experimental and phenomenological studies that the word "signal" refers to $|\mathcal{M}_{\mathrm{S}}|^2$ alone. Moreover, it is also common to neglect the interference as it is usually smaller than the experimental precision. However, this is not always the case, and the interference may be a significant part of the contribution from BSM models.

The interference may especially be enhanced when taking off-shell effects of heavy resonances into account. The tail ends of a Breit–Wigner line shape can overlap with a region of the phase space that is populated by the background, leading to a significant signal–background interference effect. This has been studied for the SM Higgs case for final-states with $\gamma\gamma$ [24, 25], ZZ [26–29], and W^+W^- [30–32].

Furthermore, in EFTs, the absolute-squared contribution will be suppressed by two powers of the new physics scale, $1/\Lambda^2$, leaving the signal being predominantly given by the interference terms with factors of $1/\Lambda$.

3.5 Next-to-Leading-Order Technology

In order to achieve a higher precision for the theoretical predictions of fixed-order calculations of QCD processes at the LHC, it is vital to include higher-order corrections. Beyond the *leading-order* (LO), also known as *Born* or *tree-level*, the first perturbative correction is the *next-to-leading-order* (NLO), which can give a sizeable contribution especially for gluon-fusion Higgs production as shown later in

Eq. (6.32). NLO corrections tends to be large for processes with a large amount of colour annihilation, and in $gg \to H$ the gluons are colour octets producing a colour singlet Higgs. On the other hand, NLO corrections tend to decrease with increasing final-state particles, and the $gg \to H + \text{jet}$ correction is comparably tiny.

The finite LO cross-section,

$$\sigma_{\text{LO}} = \int_m \mathrm{d}\sigma_B \,, \tag{3.25}$$

consist of a m-parton phase space integral over the differential Born cross-section.

The NLO cross-section,

$$\sigma_{\text{NLO}} = \int_m \Big[\mathrm{d}\sigma_B + \mathrm{d}\sigma_V \Big] + \int_{m+1} \mathrm{d}\sigma_R \,, \tag{3.26}$$

additionally consists of a virtual one-loop correction with m-kinematics and an exclusive real emission correction with $m+1$-kinematics. The following sections will briefly introduce the general ideas behind the calculation of the real $\mathrm{d}\sigma_R$ and virtual $\mathrm{d}\sigma_V$ contributions, the latter taking the form of tree–loop interferences.

See refs. [11] and [22] for comprehensive reviews of NLO calculations.

3.6 One-Loop Calculations

This section will focus on the virtual corrections in the form of one-loop amplitudes.

A generic one-loop diagram with n external legs and n propagators is shown in Figure 3.2. Here k denotes the loop four-momentum. The propagators will then have four-momentum $q_i = k + \sum_{j=1}^{i} p_j$. Defining all $p_1, p_2, \ldots, p_n$ four-momenta as incoming will lead to four-momentum conservation $\sum_{i=1}^{n} p_i = 0$ and hence $q_n = k$.

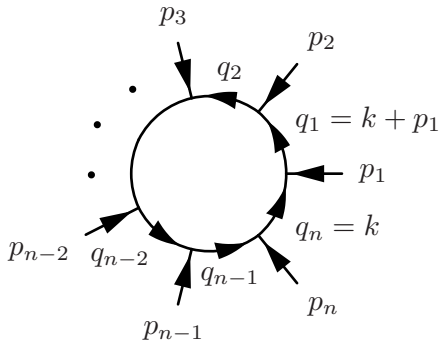

Figure 3.2. Generic one-loop Feynman diagram showing the four-momenta conventions.

The most general form of the integral for the generic one-loop diagrams is

$$I_n^{D,\mu_1\dots\mu_r} = \int \frac{\mathrm{d}^D k}{(2\pi)^D} \frac{k^{\mu_1}\dots k^{\mu_r}}{\prod_i (q_i^2 - m_i^2 + i\delta)}\,, \tag{3.27}$$

where m_i are the propagator masses. Here r refers to the *rank* of the tensor integral. In the case of scalar propagators, the Lorentz-tensor structure in the numerator is equal to one, and the integral is referred to as a *scalar integral*. The denominator is the free propagator as in Eq. (2.29).

In $D = 4$ dimensions, the scalar integral is divergent in two cases:

- *Ultraviolet* (UV) divergences, in the limit $k \to \infty$.
- *Infrared* (IR) divergences, when the loop momenta becomes soft or collinear to one of the external particles.

The loop integrals can be made finite using *dimensional regularisation* [33, 34] using $D = 4 - 2\varepsilon$. The UV divergences will then manifest themselves as simple poles $1/\varepsilon$. The advantage of dimensional regularisation is that Lorentz and gauge invariance are guaranteed, compared to e.g. momentum cut-off methods. The regularisation is then followed by a standard renormalisation scheme of the Lagrangian, adding corresponding counterterms.

Loop calculations can be cumbersome and several methods exists to simplify the expressions, such as *Feynman parameterisation*. The loop calculations can be simplified by collecting the loop propagators into a single denominator using the general identity

$$\frac{1}{A_1^{\nu_1}\dots A_n^{\nu_n}} = \frac{\Gamma(\sum_i \nu_i)}{\prod_i \Gamma(\nu_i)} \int_0^1 \mathrm{d}^n x_i \delta\left(\sum_i x_i - 1\right) \frac{\prod_i x_i^{\nu_i - 1}}{(\sum_i x_i A_i)^{\sum_i \nu_i}}\,. \tag{3.28}$$

This is valid for any complex $A_1, \dots, A_n$, provided that $\mathrm{Re}(\nu_i) > 0$. The integration parameters x_i are called *Feynman parameters*. Note that $\nu_i = 1 \,\forall\, i$ for the generic one-loop diagram.

3.6.1 Reduction of One-Loop Integrals

The number of Feynman diagrams will grow significantly for each increasing order of perturbation theory and for each additional number of final-state particles. Fortunately, every one-loop integral with an arbitrary number n of external legs

can be reduced to a linear combinations of basis integrals with $n \leq 4$. These basis integrals are usually referred to as *n–point functions*, with a further naming scheme referring to them as *tad-poles* (1–point), *bubbles* (2–point), *triangles* (3–point), and *boxes* (4–point). Reduction methods greatly lower the computational complexity of one-loop calculations, making them useful for automatic tools. In addition to reduction, automatic tools will often represent all four-momenta as outgoing to simplify the momentum conservation expression – with this convention it is also easy obtain results for any crossed process.

The Passarino and Veltman reduction method [35] can be used to reduce tensor integrals into scalar integrals, by using the fact that the scalar products between loop momenta and external momenta in the Lorentz structure can be expressed as a linear combination of propagators. Solving for this expansion in terms of scalar integrals will introduce a *Gram determinant* G. Each loop momentum factor in the numerator of the loop integral will introduce an inverse power of the Gram determinant, leading to an overall factor $1/(\det G)^r$, where r is the rank of the tensor integral. In kinematical regions where $\det G \to 0$, this can cause issues with numerical instability. This can be alleviated with various rescue procedures.

The OPP reduction method [36], implemented in the program `CutTools` [37], is based on a decomposition of the one-loop amplitude to a simple sum of coefficients multiplied by basis scalar integrals at the integrand level. This is achieved by numerically exploiting the kinematical equations for the integration momentum [38], which extends the unitarity cut method [39–41]. The OPP method is well suited for numerical programs, as it requires minimal information about the form of the one-loop sub-amplitudes.

The open-loops algorithm [42–44], used in OpenLoops 2 [45], recursively generates loop amplitudes in terms of cut-open loop diagrams, called open loops, with tree topology but loop momenta. The algorithm combines tensor integral reduction and the OPP method on the loop momenta that is stripped of colour and helicity structures. The latest version of OpenLoops implements on-the-fly reduction which avoids high-rank tensors by performing the reduction of the open-loop diagrams on-the-fly at the integrand level [46].

The possibility of switching between the OPP method and tensor integral reduction is also implemented in MadLoop5 in MadGraph5_aMC@NLO [47].

3.6.2 Form Factor Representation

The loop integrals can written in a *form factor representation* where the Lorentz structure has been extracted. In this case, each Lorentz tensor is multiplied with a scalar quantity known as a *form factor*. As an example, the matrix element for gluon-fusion Higgs production, $gg \to H$, can be written in the form factor representation as [48]

$$\mathcal{M} = \frac{\alpha_s}{3\pi v} F \delta^{ab} \left(q_1 q_2 g^{\mu\nu} - q_1^\nu q_2^\mu \right) , \tag{3.29}$$

where q_1 and q_2 are the four-momenta of the incoming gluons. The $gg \to H$ form factor F at the one- and two-loop level is given later in Eq. (6.15).

3.7 Dipole Subtraction

The infrared (IR) divergences in the loop diagrams will manifest themselves in double and single poles, $1/\varepsilon^2$ and $1/\varepsilon$, after dimensional regularisation. Due to the Bloch–Nordsieck (BN) and Kinoshita–Lee–Nauenberg (KLN) theorems [49–51], these will cancel with the corresponding IR divergences in the real emission diagrams. However, the integrals over $\mathrm{d}\sigma_V$ and $\mathrm{d}\sigma_R$ in Eq. (3.26) are separately divergent, and it will be impossible to integrate each in D dimensions in numerical calculations. Hence, subtraction methods are used to isolate and subtract the IR divergences before integration can be performed.

Several different IR subtraction schemes exists, such as Frixione–Kunst–Signer (FKS) subtraction [52, 53] and Nagy–Soper subtraction [54]. This thesis will employ the dipole subtraction method of Catani and Seymour [55], originally developed for massless particles but extended to the massive case in ref. [56]. This section will sketch the method in a schematic way with some relevant details.

Removal of IR divergences can be done by introducing a *local counterterm* $\mathrm{d}\sigma_A$ with the same pointwise IR divergent behaviour as $\mathrm{d}\sigma_R$. The NLO cross-section then becomes

$$\sigma_{\mathrm{NLO}} = \int_m \mathrm{d}\sigma_B + \int_{m+1} \Big[(\mathrm{d}\sigma_R)_{\varepsilon=0} - (\mathrm{d}\sigma_A)_{\varepsilon=0} \Big] + \int_m \Big[\mathrm{d}\sigma_V + \int_1 \mathrm{d}\sigma_A \Big]_{\varepsilon=0} , \tag{3.30}$$

where the integrand in the second integral can be safely evaluated in the $\varepsilon \to 0$ limit and can integrated numerically in four dimensions. In the third integral, the one-parton integral over $\mathrm{d}\sigma_A$ cancels the poles in $\mathrm{d}\sigma_V$ for infrared-safe jet observables.

The local counterterm is constructed by a phase space convolution and sum over

colour and spins indices of the colour and spin projected Born cross-section, $\mathrm{d}\sigma_B$, and the process-independent, universal dipole factors, $\mathrm{d}V_{\text{dipole}}$, which has the same singular behaviour as $\mathrm{d}\sigma_R$. Symbolically this can be written as

$$\mathrm{d}\sigma_A = \sum_{\text{dipoles}} \mathrm{d}\sigma_B \otimes \mathrm{d}V_{\text{dipole}} \,, \tag{3.31}$$

where each dipole corresponds to a $m+1$-parton configuration in $\mathrm{d}\sigma_R$ which is degenerate with a m-parton configuration in the soft and collinear limit.

Since $\mathrm{d}V_{\text{dipole}}$ is fully integrable analytically, the integrated counterterm in the last integral of Eq. (3.30) can be written symbolically as

$$\int_{m+1} \mathrm{d}\sigma_A = \sum_{\text{dipoles}} \int_m \mathrm{d}\sigma_B \otimes \int_1 \mathrm{d}V_{\text{dipole}} = \int_m \left[\mathrm{d}\sigma_B \otimes \mathbf{I}\right] \,, \tag{3.32}$$

with the universal factor,

$$\mathbf{I} = \sum_{\text{dipoles}} \int_1 \mathrm{d}V_{\text{dipole}} \,, \tag{3.33}$$

which contains the ε poles necessary to cancel the poles in $\mathrm{d}\sigma_V$.

For hadronic initial states, the cross-section will be convoluted with parton distribution functions, containing collinear singularities. Hence, the NLO cross-section is supplemented with a collinear subtraction term. The final result for the subtraction procedure becomes

$$\begin{aligned} \sigma_{\text{NLO}} = &\int_m \mathrm{d}\sigma_B + \int_{m+1} \Big[\left(\mathrm{d}\sigma_R\right)_{\varepsilon=0} - \left(\mathrm{d}\sigma_A\right)_{\varepsilon=0} \Big] \\ &+ \int_m \Big[\mathrm{d}\sigma_V + \mathrm{d}\sigma_B \otimes \mathbf{I} \Big]_{\varepsilon=0} + \int_0^1 \mathrm{d}x \int_m \Big[\mathrm{d}\sigma_B \otimes (\mathbf{P} + \mathbf{K}) \Big]_{\varepsilon=0} \,, \end{aligned} \tag{3.34}$$

where the universal $\mathbf{P}$ and $\mathbf{K}$ factors depends on the longitudinal momentum fraction x, and are finite parts of the initial-state collinear singularities.

3.7.1 The Local Counterterm

The singular part of any given real emission matrix element, $|\mathcal{M}_{m+1}|^2$, is universal, i.e. process-independent. Hence, the soft and collinear singularities can be factorised as

$$|\mathcal{M}_{m+1}|^2 \to |\mathcal{M}_m|^2 \otimes \mathbf{V}_{ij,k} \,, \tag{3.35}$$

where $\mathbf{V}_{ij,k}$ is the singular factor and depends on the four-momenta and quantum numbers of the partons i, j, and k. Parton $ij \to i+j$ is called the *emitter* while k is the *spectator*.

The dipole contribution to the local counterterm, $\mathrm{d}\sigma_A = \mathcal{D}\,\mathrm{d}\Phi_{m+1}$, is composed of four terms,

$$\mathcal{D} = \underbrace{\sum_{\{i,j\}}\sum_{k\neq i,j}\mathcal{D}_{ij,k}}_{\substack{\text{Final-state emitter}\\ \text{Final-state spectator}}} + \underbrace{\sum_{\{i,j\}}\sum_{a}\mathcal{D}^{a}_{ij}}_{\substack{\text{Final-state emitter}\\ \text{Initial-state spectator}}} + \underbrace{\sum_{\{a,i\}}\sum_{j\neq i}\mathcal{D}^{ai}_{j}}_{\substack{\text{Initial-state emitter}\\ \text{Final-state spectator}}} + \underbrace{\sum_{\{a,i\}}\sum_{b\neq a}\mathcal{D}^{ai,b}}_{\substack{\text{Initial-state emitter}\\ \text{Initial-state spectator}}}, \tag{3.36}$$

which approximate the divergent part of the real matrix element $|\mathcal{M}_{m+1}|^2$ in different singular regions. The four different terms corresponds to different pairs of emitter and spectator as shown in Figure 3.3.

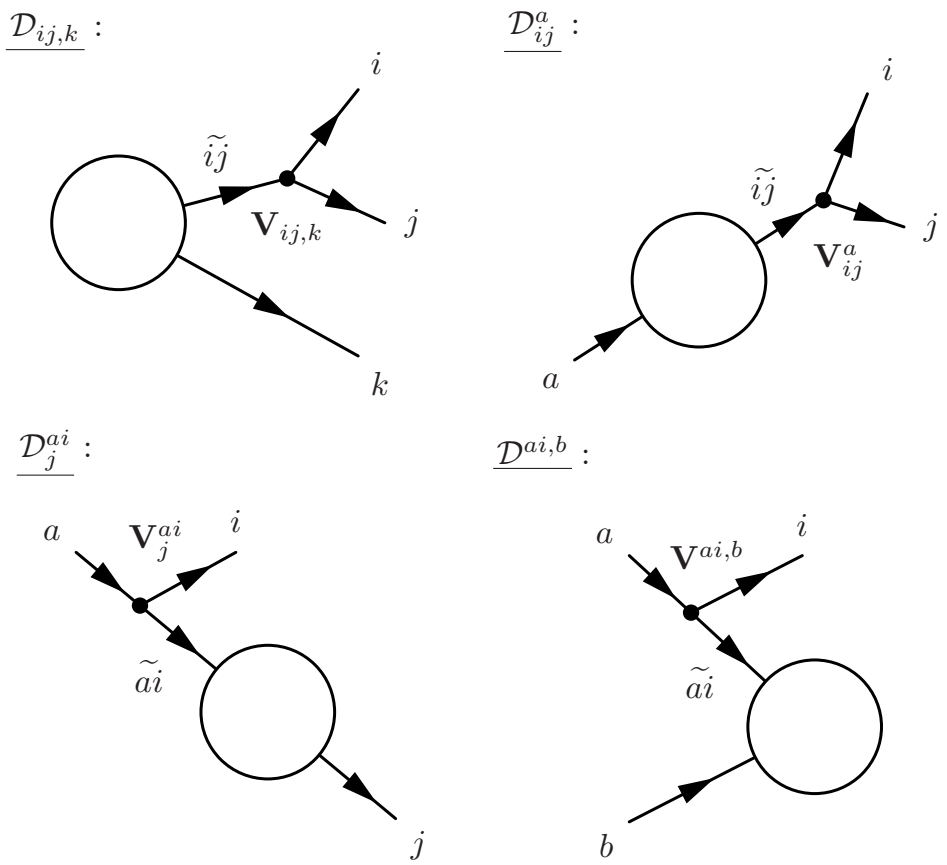

Figure 3.3. Diagrams of the four dipole terms in Eq. (3.36). Arrows denote directions of momenta.

3.7.2 Integrated Counterterms

The insertion operator $\mathbf{I}$ cancels all divergences in the virtual one-loop matrix elements and is given by

$$\mathbf{I}(\{p\};\varepsilon) = -\frac{\alpha_s}{2\pi} C_\varepsilon \sum_I \frac{1}{\mathbf{T}_I^2} \mathcal{V}_I(\varepsilon) \sum_{J\neq I} \mathbf{T}_I \cdot \mathbf{T}_J \left(\frac{\mu^2}{2p_I \cdot p_J}\right)^\varepsilon , \tag{3.37}$$

where $\{p\}$ is a set of parton four-momenta, I, J are momenta indices, $\mathcal{V}_I(\varepsilon)$ is a universal singular function depending only on parton flavour, and with C_ε being the conventional $\overline{\text{MS}}$ normalisation factor,

$$C_\varepsilon = \frac{(4\pi)^\varepsilon}{\Gamma(1-\varepsilon)} = 1 + \varepsilon\left[\ln(4\pi) - \gamma_E\right] + \mathcal{O}(\varepsilon^2) , \tag{3.38}$$

where $\gamma_E \approx 0.577$ is the Euler–Mascheroni constant.

For hadronic initial-states, the NLO cross-section obtains finite remainders from the subtraction into the parton distribution functions. These finite remainders comes in terms of two insertion operators, $\mathbf{P}$, which is factorisation-scale dependent, and $\mathbf{K}$, which is the factorisation-scheme dependent initial-state operator[2]. For initial-state partons,

$$\mathbf{P}^{a,b}(\{p\}, xp_a, x, \mu_F^2) = \frac{\alpha_s}{2\pi} P^{ab}(x) \frac{1}{\mathbf{T}_b^2} \sum_{I\neq b} \mathbf{T}_I \mathbf{T}_b \ln \frac{\mu_F^2}{2xp_a \cdot p_I} , \tag{3.39}$$

while for final-state partons,

$$\mathbf{P}_{b,a}(\{p\}, p_a/z, z, \mu_F^2) = \frac{\alpha_s}{2\pi} P_{ba}(z) \frac{1}{\mathbf{T}_b^2} \sum_{I\neq b} \mathbf{T}_I \mathbf{T}_b \ln \frac{z\mu_F^2}{2p_a \cdot p_I} , \tag{3.40}$$

where $P^{ab} = P_{ba}$ are the Altarelli–Parisi probabilities and μ_F is the factorisation scale. For two initial-state hadrons,

$$\begin{aligned}\mathbf{K}^{a,a'}(x) = \frac{\alpha_s}{2\pi} &\left\{ \bar{K}^{aa'}(x) - K_{\text{F.S.}}^{aa'}(x) + \delta^{aa'} \sum_i \frac{\mathbf{T}_b \cdot \mathbf{T}_{a'}}{\mathbf{T}_{a'}^2} \gamma_i \left[\left(\frac{1}{1-x}\right)_+ + \delta(1-x) \right] \right\} \\ &- \frac{\alpha_s}{2\pi} \frac{\mathbf{T}_b \cdot \mathbf{T}_{a'}}{\mathbf{T}_{a'}^2} \widetilde{K}^{aa'}(x) ,\end{aligned} \tag{3.41}$$

where $\bar{K}^{aa'}(x)$, $K_{\text{F.S.}}^{aa'}(x)$, and $\widetilde{K}^{aa'}(x)$ are flavour kernels.

[2]Final-state collinear singularities from fragmentation functions are handled by an additional insertion operator, $\mathbf{H}$. However, this is not relevant for this thesis.

3.8 Beyond Next-to-Leading-Order

Beyond next-to-leading-order in QCD lies *next-to-next-to-leading-order* (NNLO) and above (N^3LO). The situation at NNLO in QCD calls for the square of one-loop diagrams, the interference between two-loop and tree-level, the interference between one-loop and tree-level with an additional parton, and finally the squared tree-level with two additional partons. In particular the evaluation of two-loop diagrams is highly non-trivial. Furthermore, while IR subtraction schemes are fully solved at NLO, they are much more complicated at NNLO, calling for new methods such as q_T slicing [57] and Antenna subtraction [58]. All of this renders NNLO significantly more difficult than NLO. While tree-level and one-loop amplitudes are fully automated for up to a relatively large number of final-state particles, only a few tools provide NNLO calculations. For gluon-fusion Higgs boson production the state-of-the-art fixed-order calculation of the total cross-section is at N^3LO [48, 59].

Beyond fixed-order calculations, which are exact to a given perturbative order, one can use *resummation techniques* in QCD to obtain results at all orders. The real emission contribution in NLO QCD describes the production of the Born final-state along with an additional parton which is experimentally reconstructed as a QCD jet. NNLO will include a contribution with two additional partons, and so on. Hence, taking all orders into account will mean considering a tower of increasing jet multiplicities. The problem is that for any fixed order of perturbation theory the diagrams with additional jets will diverge in the limit $p_T \to 0$. However, a finite result can be obtained by resumming the soft and collinear limits of the additional parton emissions to all orders. This idea is also used in *parton shower algorithms*, which simulates the effects of higher-order corrections by iteratively evolving down in e.g. the virtuality of the emitted partons, resulting in a shower of radiated jets.

4

Phenomenology at Hadron Colliders

This chapter describes in detail the physics and phenomenology of hadron–hadron interactions (also known as *events*). This chapter is based on refs. [11, 21, 60–62] unless otherwise noted.

4.1 Physical Picture of Hadronic Interactions

This section will focus on proton–proton collisions on the form

$$pp \to n + X\,, \tag{4.1}$$

as that is the prevalent type of interactions currently happening at the LHC. The full time-dependent picture of a proton–proton collision is illustrated in Figure 4.1, with time moving from left to right.

The steps are, more or less chronologically, as follows:

1. The structure of the incoming colliding protons are described by *parton distribution functions* (PDFs), giving the number density of partons in the proton.

2. Two partons a and b, one from each colliding proton, will interact in a *hard scattering interaction*. This can be calculated in perturbative QFT by drawing all Feynman diagrams up to a certain order in the perturbative expansion and evaluate the matrix elements.

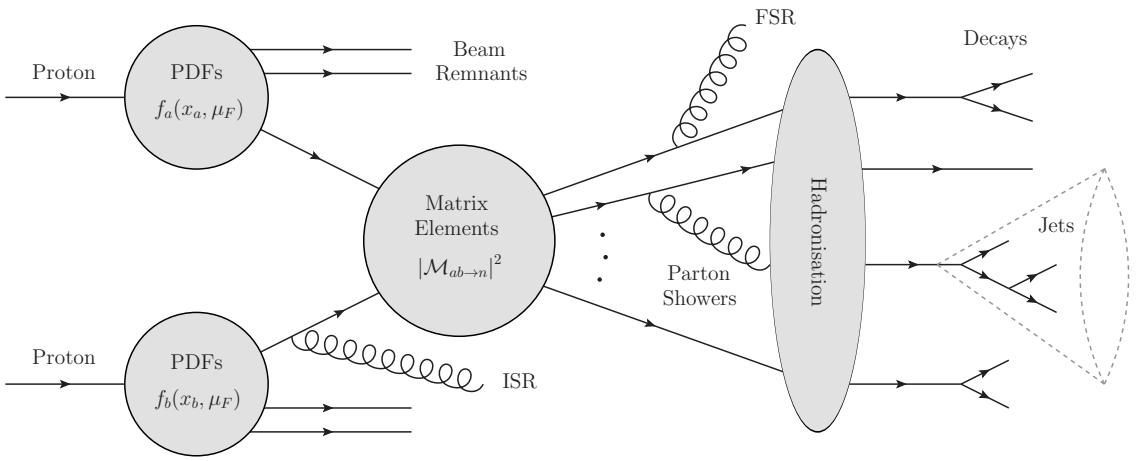

Figure 4.1. An illustration of the full physical picture of a proton-proton collision. Time moves from left to right. Note that the initial-state radiation (ISR) and final-state radiation (FSR) involving non-colour-singlets will of course also incur hadronisation.

3. Each incoming proton will dissociate, leaving behind *beam remnants* which do not take part in the hard scattering interaction.

4. Cascades of partons emitted from the initial- and final-states can be simulated by *parton shower* algorithms.

5. Any produced partons from the hard scattering will undergo *hadronisation*.

6. Heavy shorter-lived hadrons will *decay* before reaching the detector, resulting in the detector-level final-state consisting mostly of pions and some kaons.

7. *Jet algorithms* are used to identify any final-state jets, i.e. collimated bunches of stable particles after hadronisation and decays. Such algorithms will likewise be employed on experimental data.

8. The composite nature of the colliding protons will result in the possibility of multiple simultaneous scatterings of partons called *multiple parton interactions (MPI)*.

The full interaction picture is simulated by general-purpose *Monte Carlo event generators*, while specialised tools focus on individual parts. Specialised tools are often best at their given task, but usually needs to be a part of larger pipeline with a general-purpose core. Table 4.1 lists some existing tools, but is far from exhaustive.

	General-purpose	Specialised
PDFs	SHERPA [63], PYTHIA [64], Herwig++ [65] ...	LHAPDF [66], HOPPET [67]
Matrix elements		OPENLOOPS [45], COMIX [68], a lot more...
Resonance decays		HDECAY [69, 70], PROPHECY4F [71–73]
Parton Showers		DIRE [74], VINCIA [75], ...
Hadronisation		–

Table 4.1. An incomplete snapshot of the landscape of high-energy physics generators and tools.

Often in theoretical studies, only the parton-level result[1] – which includes the PDFs and hard-scattering matrix element – is considered. Parton-level results allows for quick assessment of deviations of new physics models from the Standard Model behaviour. Several parton-level Monte Carlo event generators exists, such as MCFM [76–79]. Other frameworks such as MADGRAPH5_AMC@NLO [47] and POWHEG BOX V2 [80–82] implements NLO calculations with parton shower matching. Since parton-level studies are what is most relevant for this thesis, they will be discussed in closer details in the following sections.

4.2 Parton Distribution Functions

Protons are not elementary particles but are complicated objects consisting of three valence quarks and a virtual sea of quarks and gluons. The distribution of partons inside the proton can be described by *parton distribution functions* (PDFs).

A PDF $f_i(x, Q^2)$ is the number density for parton i in the proton, with a giving momentum fraction x, and when probing the proton at an energy scale Q^2.

Figure 4.3 shows some PDFs for different partons. The up and down quark PDFs exhibit a peak around $x \sim 1/3$ due to the valence quarks. All of the PDFs are peaked at small x values, due to virtual QCD corrections in the form of sea partons, with the gluon dominating at low x, especially at higher energy scales.

The evolution of the PDFs in x–Q^2 space can be calculated from first principles in perturbative QCD. The evolution in Q^2 is handled by the Dokshitzer–Gribov–

[1]Here *parton-level* refers to the final-state immediately after the hard scattering, i.e. before hadronisation and decays.

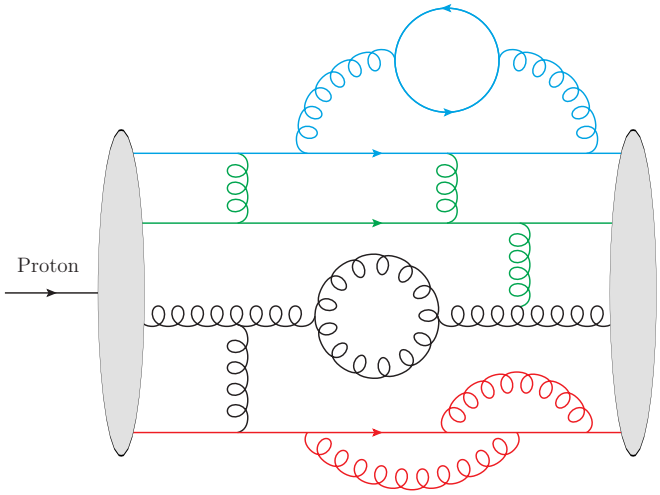

Figure 4.2. Illustration of the QCD fluctuations in a proton. The proton consists of three valence quarks with around $\sim 1/3$ of the total momentum each. In addition, there are several virtual gluons and sea quarks peaked at low momentum fraction. The structure of the fluctuations becomes more pronounced when the proton is probed at larger Q^2 energies.

Lipatov–Altarelli–Parisi (DGLAP) equation [83–85],

$$Q^2 \frac{\partial f_b(x,Q^2)}{\partial Q^2} = \frac{\alpha_s(Q^2)}{2\pi} \sum_a \int_x^1 \frac{\mathrm{d}z}{z} P_{ba}\left(z, \alpha_s(Q^2)\right) f_a\left(\frac{x}{z}, Q^2\right) , \tag{4.2}$$

with $P_{ba}(z,\alpha_s) = P_{ba}^{(0)}(z) + \mathcal{O}(\alpha_s)$ being the splitting kernels. The physical interpretation of $P_{ba}^{(0)}(z)$ is the leading-order probability for a parton a to split into a parton b. Note however, that for energies below 1–2 GeV, the perturbative regime of QCD breaks down and it is therefore necessary to use empirical fits of the PDFs to data as the starting point. Such fits takes the form of

$$xf(x,Q^2) = ax^b(1-x)^c , \tag{4.3}$$

where a is an overall factor, b is associated with small-x Regge behaviour, and c is for large-x valence counting rules. For example, the gluon PDF at large x and low Q^2 is approximately given by $xf_g(x,Q^2) \sim (1-x)^6$. Additional factors can be introduced to improve PDF fits. Several different PDF fits exists, which can differ in the initial scale of the Q^2 evolution, the parameterisation of the PDF itself, the value of $\alpha_s(M_Z^2)$, the selection of data used in the fits, and the analysis of uncertainties. Usual methods include Hessian eigenvectors [86] and artificial neural networks [87].

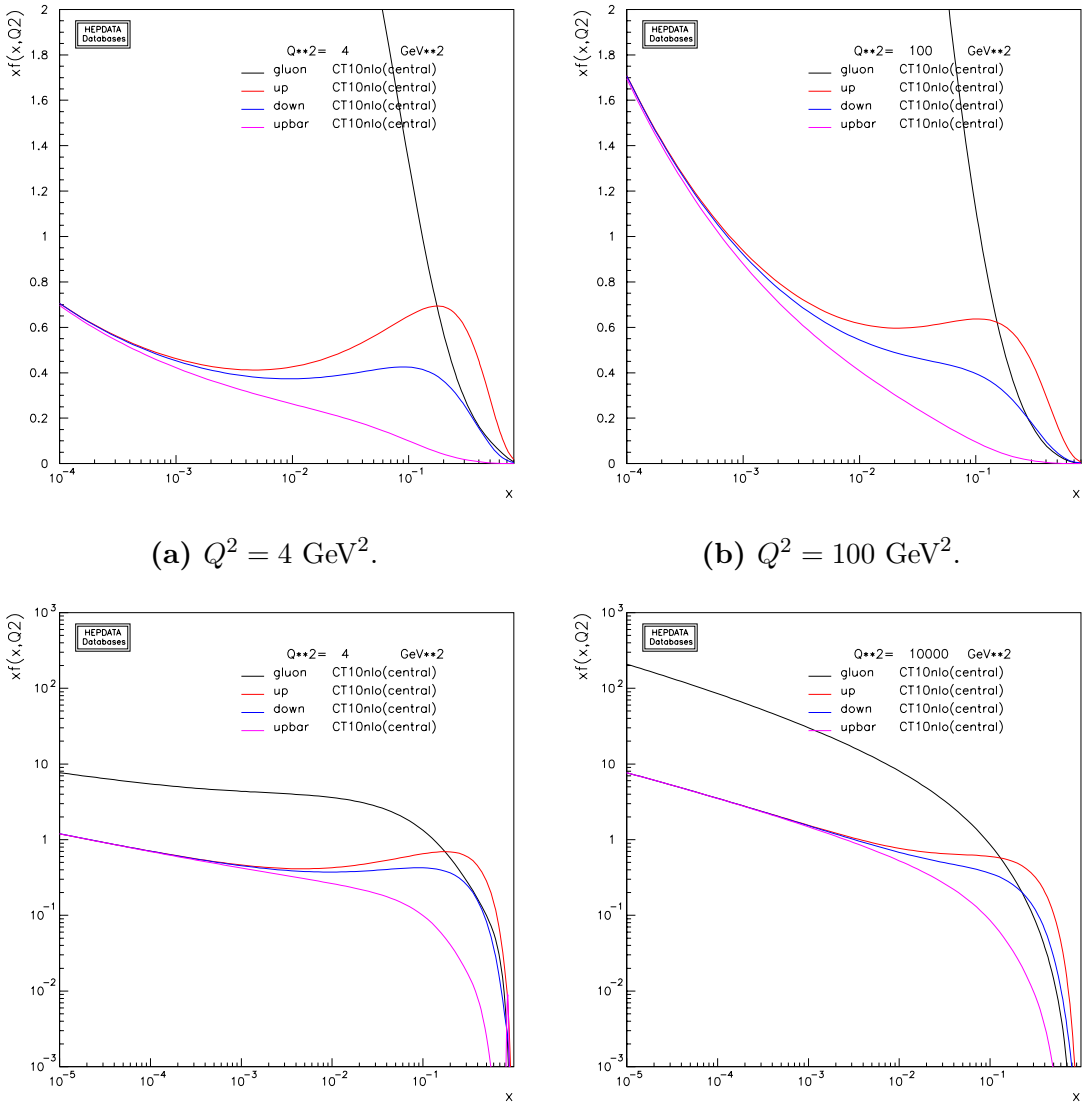

(a) $Q^2 = 4$ GeV^2.

(b) $Q^2 = 100$ GeV^2.

(c) Log–log plot, $Q^2 = 4$ GeV^2.

(d) Log–log plot, $Q^2 = 10000$ GeV^2.

Figure 4.3. The PDFs for the gluon as well as for the up, down, and anti-up quarks from the CT10 NLO PDF set for different energy scales Q^2. Plotted using the Durham HepData Project PDF plotter, available at `http://hepdata.cedar.ac.uk/pdf/pdf3.html`.

4.3 The Factorisation Theorem

The QCD factorisation theorem takes the form

$$\sigma = \sum_{a,b} \int_0^1 \mathrm{d}x_a \, \mathrm{d}x_b \int f_a(x_a, \mu_F) f_b(x_b, \mu_F) \, \mathrm{d}\hat{\sigma}_{ab\to n}(\mu_F, \mu_R) \,, \tag{4.4}$$

where the sum is over a and b partons in the protons, with f_a and f_b being their respective PDFs. Here $\mathrm{d}\hat{\sigma} \sim |\mathcal{M}|^2$ is the parton-level differential cross-section,

$$\mathrm{d}\hat{\sigma} = \frac{1}{2\hat{s}} \left|\mathcal{M}_{ab\to n}(\Phi_n; \mu_F, \mu_R)\right|^2 \mathrm{d}\Phi_n \,, \tag{4.5}$$

which is integrated over the n-body phase-space, $\mathrm{d}\Phi_n$. The factor in front is the incoming partonic flux with $\hat{s} = x_1 x_2 s$ being the squared centre-of-mass energy for the partonic collision, while s is that of the hadronic (proton–proton) collision. This particular flux is in the case of massless initial-state partons.

The PDFs can be considered as the probability[2] of taking some given partons out of the proton, while the partonic cross-section can be considered as the probability amplitude for those partons to interact in a certain manner. The multiplication rule for a joint probability of events A and B, $P(A \cap B) = P(A) \times P(B)$, only holds if the events A and B are independent, meaning their probabilities $P(A)$ and $P(B)$ are uncorrelated. Hence, the factorisation theorem implies that any quantum coherence between the non-perturbative proton structure and the subsequent perturbative interaction is negligible. This is only the case for high energy collisions.

4.4 Phase Space Integration

The n-particle Lorentz-invariant phase space $\mathrm{d}\Phi_n$ for a $2 \to n$ process is given by

$$\mathrm{d}\Phi_n = (2\pi)^4 \delta^{(4)} \left(p_a + p_b - \sum_{i=1}^{n} p_i\right) \prod_{i=1}^{n} \frac{\mathrm{d}^3 p_i}{(2\pi)^3 2E_i} \,, \tag{4.6}$$

with the Dirac delta requiring overall four-momentum conservation, p_a and p_b being the incoming four-momenta, and the product is over the phase space differential for each final-state particle.

For a $2 \to 1$ process with massless initial-state particles and four-momenta $p_1 + p_2 \to p_3$, for which $p_3^2 = m^2$, the phase space measure becomes simply

$$\mathrm{d}\Phi_1 = (2\pi)^4 \delta^{(4)} (p_1 + p_2 - p_3) \frac{\mathrm{d}^3 p_3}{(2\pi)^3 2E_3} = 2\pi \delta(\hat{s} - m^2) \,, \tag{4.7}$$

where $\hat{s} = (p_1 + p_2)^2$ is the Mandelstam variable, i.e. the squared partonic collision energy.

[2]They are in fact *number densities*.

For $2 \to 2$ processes, with four-momenta $p_1 + p_2 \to p_3 + p_4$, for which the final-state may be massive, the phase space measure in the centre-of-mass frame becomes

$$\begin{aligned} \mathrm{d}\Phi_2 &= (2\pi)^4 \delta^{(4)}\left(p_1 + p_2 - p_3 - p_4\right) \frac{\mathrm{d}^3 p_3}{(2\pi)^3 2E_3} \frac{\mathrm{d}^3 p_4}{(2\pi)^3 2E_4} \\ &= \frac{|\mathbf{p_3}|}{16\pi^2 \sqrt{\hat{s}}} \, \mathrm{d}\Omega \,, \end{aligned} \tag{4.8}$$

where $\mathrm{d}\Omega = \sin\theta \, \mathrm{d}\theta \, \mathrm{d}\phi$ is the differential solid angle for the scattering angle θ between p_3 and p_1, and ϕ is the azimuthal angle.

For $n > 2$ final-state particles the phase space can be recursively written as

$$\mathrm{d}\Phi_n(P; p_1, \ldots, p_n) = \mathrm{d}m^2_{12\ldots(n-1)} \, \mathrm{d}\Phi_2(P; p_{12\ldots(n-1)}, p_n) \, \mathrm{d}\Phi_{n-1}(P; p_1, \ldots, p_{n-1}) \,, \tag{4.9}$$

where P is for the respective initial-state. This can be considered as a sequential decay chain with intermediate masses. As an example, the factorised three-body phase space for $p_a + p_b \to p_1 + p_2 + p_3$ is given by

$$\mathrm{d}\Phi_3(p_a, p_b; p_1, p_2, p_3) = \mathrm{d}m^2_{12} \, \mathrm{d}\Phi_2(p_a, p_b; p_{12}, p_3) \, \mathrm{d}\Phi_2(p_{12}; p_1, p_2) \,. \tag{4.10}$$

Most tools for automatic phase space generation uses this recursive method.

4.4.1 The Monte Carlo Method

The often high complexity of the differential cross-section calls for the use of numerical integration. The full phase space $\mathrm{d}x_a \mathrm{d}x_b \mathrm{d}\Phi_n$ will have a dimensionality of $3n - 2$ for n final-state particles, due to three degrees of freedom from the on-shell four-momentum of each n final-state particle plus two degrees of freedom from the two momentum fractions, and finally subtracting four degrees of freedom from the overall dimensionality due to energy conservation. For normal LHC processes the number of final-state particles can be rather large, and therefore the *Monte Carlo (MC) method* is the most suitable, due to its relatively fast convergence at high dimensions compared to other methods, as seen in Table 4.2.

The basis of the Monte Carlo method is that a definite integral can be written in terms of the average of the integrand [88],

$$I = \int_a^b f(x) \, \mathrm{d}x = (b - a) \langle f(x) \rangle \,. \tag{4.11}$$

Method	Error	Faster convergence for MC
Monte Carlo method	$N^{-1/2}$	–
Midpoint rule	$N^{-1/d}$	$d > 2$
Trapezoidal rule	$N^{-2/d}$	$d > 4$
Simpson's rule	$N^{-4/d}$	$d > 8$
m-th Gaussian quadrature	$N^{-(2m-1)/d}$	$d > 4m - 2$

Table 4.2. Comparison of how the error scales for different methods of numerical integration of a d-dimensional function for a comparable number of points N [88,89].

This can be done numerically by taking N uniformly random numbers, $\rho_i \sim \mathcal{U}(0,1)$, and transforming each to be within the integration range,

$$x_i = (b-a)\rho_i + a\,, \tag{4.12}$$

which can be used to provide an estimate of the integral,

$$I \approx (b-a)\frac{1}{N}\sum_{i=1}^{N} f(x_i)\,. \tag{4.13}$$

In practice, it is typical to define a *weight*, $W_i = (b-a)f(x_i)$, with the integral estimate I_N simply being the average of the weights,

$$I_N = \frac{1}{N}\sum_{i=1}^{N} W_i\,. \tag{4.14}$$

An advantage of the Monte Carlo method is that it provides an easy estimate of the error. Due to the Central Limit Theorem, the distribution of $\langle f(x)\rangle$ will tend towards a Gaussian distribution with standard deviation $\sigma_{\mathrm{MC}} = \sigma/\sqrt{N}$, hence the error will decrease with the number of points N as $1/\sqrt{N}$. The variance is defined as

$$V_N = \frac{1}{N}\sum_{i=1}^{N} W_i^2 - \left(\frac{1}{N}\sum_{i=1}^{N} W_i\right)^2\,. \tag{4.15}$$

The integral is then estimated by

$$I \approx I_N \pm \sqrt{\frac{V_N}{N}}\,. \tag{4.16}$$

The Monte Carlo error estimate is independent of the dimensionality of the integrand

function f, as opposed to other methods for numerical integration. A comparison of the error estimates for different numerical integration methods as functions of N and the dimensionality is shown in Table 4.2. Most "well-behaved" functions, i.e. with finite variance, will tend to a Gaussian distribution very quickly, so σ_{MC} can be regarded as a good error estimate. In general, few points are needed to get a first estimate.

An additional advantage of the Monte Carlo method is that it naturally maps to reality at particle collider experiments by generating random phase space points, i.e. *events*, as a by-product. These can then be saved alongside the associated event weights in the standard HepMC [90, 91] or LHEF [92] format, or they can be used to generate histograms for differential distributions.

The main disadvantage of Monte Carlo integration is the slow convergence for low dimensions. This can be remedied by using *importance sampling*, where more samples are taken in regions where the integrand function is large, and less in regions where it is small. This is an attempt to minimise the variance, and make the integration more effective. The integrands encountered in particle physics will take the form of the differential cross-section $\mathrm{d}\sigma \sim |\mathcal{M}|^2 \,\mathrm{d}\Phi_n$, as in Eq. (4.5). For many processes of interest, these will often consist of heavy resonances with Breit–Wigner line shapes as introduced in Eq. (3.20). In this case, the integral to obtain the total cross-section will take the form

$$\sigma = \int \mathrm{d}\sigma = \int_{\hat{s}_{\min}}^{\hat{s}_{\max}} \frac{1}{(\hat{s} - m^2)^2 + m^2\Gamma^2} \,\mathrm{d}\hat{s}\,. \tag{4.17}$$

Using the transformation $\hat{s} \to \rho$ [89], with

$$\hat{s} = m\Gamma \tan\rho + m^2\,, \tag{4.18}$$

with the Jacobian

$$J = \left|\frac{\partial\hat{s}}{\partial\rho}\right| = m\Gamma \sec^2\rho\,, \tag{4.19}$$

the integrand can be rewritten as a constant function,

$$\sigma = \frac{1}{m\Gamma}\int_{\rho_{\min}}^{\rho_{\max}} \mathrm{d}\rho\,, \tag{4.20}$$

for which the variance vanishes, $V_N = 0$. For more complicated integrands with multiple peaks, a *multi-channel* approach can be used. Such a method is implemented in the commonly used code VEGAS [93, 94].

5

H1JET, a Fast Program to Compute p_T Distributions

This chapter will introduce H1JET, a fast and easy-to-use program that computes the total cross-section and the differential distribution in the transverse momentum distribution of a colour singlet, for leading-order $2 \to 1$ and $2 \to 2$ processes. H1JET can be used to quickly assess deviations of selected new physics models from the Standard Model behaviour, and quickly obtain distributions of relevance for Standard Model phenomenology.

H1JET has been published in ref. [95], and the code is available at ref. [96].

5.1 Motivation

After the observation of the Higgs boson in 2012 by the ATLAS and CMS experiments [4, 5] the pressing issue is to explore and fully characterise the Higgs sector in order to understand the mechanism behind electroweak symmetry breaking.

The effective low-energy CP-invariant Lagrangian for Higgs production through gluon fusion is [97]

$$\mathcal{L}_{\text{eff.}} \supset -\kappa_t \frac{m_t}{v} t\bar{t}H + \kappa_g \frac{\alpha_s}{12\pi} \frac{H}{v} G^a_{\mu\nu} G^{\mu\nu\, a}\,, \tag{5.1}$$

where the first term is the short-distance top-loop contribution parameterised by κ_t, and the second term is the long-distance direct contribution parameterised by κ_g.

The terms in Eq. (5.1) are dimension-5, as they refer to the physical Higgs field H after electroweak symmetry breaking. The parameters, κ_t and κ_g, are anomalous couplings, i.e. they allow for deviations from the SM behaviour.

The total cross-section will only allow access to the sum of the κ's,

$$\frac{\sigma(\kappa_t, \kappa_g)}{\sigma^{\mathrm{SM}}} \propto (\kappa_t + \kappa_g)^2 \,, \tag{5.2}$$

which makes it difficult to separate the short- and long-distance contributions [98]. To solve this problem, one can consider the process $pp \to t\bar{t}H$, i.e. the production of a Higgs with a top–anti-top pair, to study the top Yukawa coupling directly [99–101]. Unfortunately, this has a low rate and a complicated final-state, which makes experimental detector study problematic.

Instead, the production of a boosted Higgs recoiling off a high-p_T jet can be considered [97, 98, 102]. This will occur through diagrams with a heavy quark loop as shown in Figure 5.1.

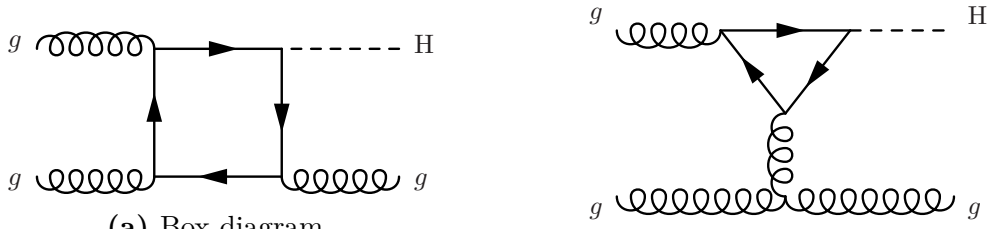

(a) Box diagram. **(b)** Triangle diagram.

Figure 5.1. Some of the leading-order Feynman diagrams for H + jet production.

For a high-p_T jet in the triangle diagram of Figure 5.1b, the internal gluon will have a high virtuality q^2, which will resolve the loop at shorter distance scales than the total $gg \to H$ cross-section will. Therefore, Higgs + jet production at large p_T will be sensitive to the mass and Yukawa coupling of the loop particle, and the structure of the heavy quark loop can be explored. The caveat of this method should be noted – it relies on considering small deviations from the SM in a kinematical region where the phase space closes. It can, nevertheless, provide a direct access to exploring new couplings to the Higgs through loops.

Production of colour singlets at high p_T is commonly used as a probe of new physics. A relevant example is the production of monojets, which can recoil either against dark matter, or a SM particle decaying into invisible particles [103, 104].

Theoretical predictions for the p_T distribution of a colour singlet, both in the SM and in new physics models, can be currently obtained with Monte Carlo event

generators, such as MadGraph5_aMC@NLO [47] or SusHi [105, 106]. These programs are general, but can be quite slow. In addition, interference terms between new physics and the SM, which carry information on the strength of new interactions, are difficult to extract from Monte Carlo event generators because they are not positive definite.

5.2 The Method

H1jet is a tool for the fast calculation of the jet p_T distribution for the production of a colour singlet X along with a jet at the LHC. The main process implemented is

$$pp \to H + \text{jet}\,, \tag{5.3}$$

where the initial-state consists of gluons and light quarks, and Higgs production proceeds via quark loops. This process can be calculated for various models as explained in section 5.3. In addition, the $b\bar{b} \to H + \text{jet}$ and $pp \to Z + \text{jet}$ processes for the SM are implemented. Moreover, H1jet is very flexible and can be easily interfaced to use a custom user-specified process.

This section will explain the method underlying H1jet, but first it is instructive to consider how to compute the Born cross-section for producing a colour singlet X, e.g. a Higgs, of mass m_X.

The partonic Born cross-section for the $ij \to X$ process is

$$\hat{\sigma}_{ij} = \frac{\pi}{m_X^2} \left|\mathcal{M}_{ij}(m_X^2)\right|^2 \delta\left(\hat{s} - m_X^2\right)\,. \tag{5.4}$$

where the $2 \to 1$ phase space in Eq. (4.7) has been used, and where $i, j = g, q, \bar{q}$.

The corresponding hadronic cross-section is given by

$$\begin{aligned}\sigma &= \frac{\pi}{m_X^2} \sum_{i,j} \int_0^1 \mathrm{d}x_1\, f_{i/p}(x_1, \mu_F) \int_0^1 \mathrm{d}x_2\, f_{i/p}(x_2, \mu_F) \sum_{i,j} |\mathcal{M}_{ij}(m_X^2)|^2 \delta\left(x_1 x_2 s - m_X^2\right) \\ &= \frac{\pi}{m_X^4} \sum_{i,j} |\mathcal{M}_{ij}(m_X^2)|^2 \mathcal{L}_{ij}\left(\frac{m_X^2}{s}, \mu_F\right)\,,\end{aligned} \tag{5.5}$$

where $\mathcal{L}_{ij}\left(\tau, \mu_F\right)$ is the partonic luminosity

$$\mathcal{L}_{ij}\left(\tau, \mu_F\right) = \tau \int_\tau^1 \frac{\mathrm{d}x}{x}\, f_{i/p}(x, \mu_F)\, f_{j/p}\left(\frac{\tau}{x}, \mu_F\right)\,, \tag{5.6}$$

with $\tau = \hat{s}/s = m_X^2/s$. H1JET obtains $\mathcal{L}_{ij}\left(m_X^2/s, \mu_F\right)$ from an interface to HOPPET [67], which tabulates and interpolates the luminosities with high efficiency, and makes it possible to compute the Born cross-section given the amplitudes $\mathcal{M}_{ij}$. This procedure is the same adopted in the program JETVHETO [107], which computes cross-sections for colour singlets with a veto on additional jets.

Considering now the differential distribution in p_T, a non-zero p_T for X is obtained via a $2 \to 2$ partonic process $p_1 p_2 \to p_3 X$, where p_1, p_2, and p_3 are massless partons, and p_X is the momentum of the colour singlet X. The goal is to compute $\mathrm{d}\sigma/\,\mathrm{d}p_T$, where p_T is the transverse momentum of p_X with respect to the beam axis. At Born level only, p_T is also the transverse momentum of the recoiling jet originated by p_3.

The amplitudes $\mathcal{M}_{ij}$ are functions of the three Mandelstam invariants

$$\begin{aligned} \hat{s} &= (p_1 + p_2)^2 = (p_3 + p_X)^2\,, \\ \hat{t} &= (p_1 - p_3)^2 = (p_2 - p_X)^2\,, \\ \hat{u} &= (p_2 - p_3)^2 = (p_1 - p_X)^2\,. \end{aligned} \tag{5.7}$$

In the centre-of-mass frame of the partonic collision, the four-momenta can be parameterised as

$$p_1 = \frac{\sqrt{\hat{s}}}{2}(1,0,0,1)\,, \qquad p_3 = p_T(\cosh\eta, 1, 0, \sinh\eta)\,, \tag{5.8}$$

$$p_2 = \frac{\sqrt{\hat{s}}}{2}(1,0,0,-1)\,, \qquad p_X = \left(\sqrt{m_X^2 + p_T^2\cosh^2\eta}, -p_T, 0, -p_T\sinh\eta\right)\,, \tag{5.9}$$

where η is the rapidity of the parton p_3 in the centre-of-mass frame.

The *partonic* p_T spectrum for the process initiated by partons ij is given by

$$\frac{\mathrm{d}\hat{\sigma}_{ij}}{\mathrm{d}p_T} = \frac{p_T}{16\pi}\int \mathrm{d}\eta \frac{|\mathcal{M}_{ij}(\hat{s},\hat{t},\hat{u})|^2}{E_X\,\hat{s}}\delta\left(\sqrt{\hat{s}} - p_T\cosh\eta - \sqrt{m_X^2 + p_T^2\cosh^2\eta}\right)\,, \tag{5.10}$$

where $E_X = \sqrt{m_X^2 + p_T^2\cosh^2\eta}$ is the energy of the colour-singlet particle p_X. The above equation selects two values of η, as follows

$$\eta = \ln\left(\hat{x}_M \pm \sqrt{\hat{x}_M^2 - 1}\right)\,, \qquad \hat{x}_M \equiv \frac{\hat{s} - m_X^2}{2p_T\sqrt{\hat{s}}}\,. \tag{5.11}$$

The corresponding hadronic cross section reads

$$\frac{\mathrm{d}\sigma}{\mathrm{d}p_T} = \sum_{i,j} \int_0^1 \mathrm{d}x_1\, f_{i/p}(x_1,\mu_F) \int_0^1 \mathrm{d}x_2\, f_{i/p}(x_2,\mu_F) \left[\frac{\mathrm{d}\hat{\sigma}_{ij}}{\mathrm{d}p_T}\,\Theta\left(\hat{s} - p_T - \sqrt{m_X^2+p_T^2}\right)\right], \tag{5.12}$$

with $\hat{s} = x_1 x_2 s$. Since Eq. (5.11) gives two monotonic functions of $\hat{s}$ for $s > p_T + \sqrt{m_X^2+p_T^2}$, varying $\hat{s}$ in the allowed range spans all possible values of η in the range $-\eta_M < \eta < \eta_M$ with

$$\eta_M \equiv \ln\left(x_M + \sqrt{x_M^2-1}\right), \qquad x_M \equiv \frac{s-m_X^2}{2p_T\sqrt{s}}. \tag{5.13}$$

Because of this it is possible to perform the η integration last, and obtain, after some manipulations,

$$\frac{\mathrm{d}\sigma}{\mathrm{d}p_T} = \frac{p_T}{8\pi}\int_{-\eta_M}^{\eta_M}\mathrm{d}\eta \sum_{i,j}\left[\frac{|\mathcal{M}_{ij}(\hat{s},\hat{t},\hat{u})|^2}{E_X \hat{s}^{3/2}}\mathcal{L}_{ij}\left(\frac{\hat{s}}{s},\mu_F\right)\right], \tag{5.14}$$

with $\hat{s} = \left(p_T\cosh\eta + \sqrt{m_X^2+p_T^2\cosh^2\eta}\right)^2$, $\hat{t} = -p_T e^{-\eta}\sqrt{\hat{s}}$, and $\hat{u} = -p_T e^{\eta}\sqrt{\hat{s}}$. The p_T spectrum becomes a one-dimensional integral over rapidity, where the integrand is the product of an amplitude squared $\left|\mathcal{M}_{ij}(\hat{s},\hat{t},\hat{u})\right|^2$, which can be provided by built-in models or by the user, and a parton luminosity, which is extracted from HOPPET. Section 5.3 presents the implemented amplitudes while section 5.7 explains the user-interface in which custom processes can be supplied to H1JET. The one-dimensional integration can be performed very quickly with a Gaussian numerical integrator as explained in subsection 5.5.1.

As shown, H1JET predicts the p_T distribution of a colour singlet fully integrated over rapidity, and completely inclusive with respect to all coloured particles, i.e. the recoiling jets. Such an approximation is not too unrealistic, because the higher the p_T, the more the colour singlet is central, and the more its decay products will be likely to pass the detector acceptance cuts.

Note that, if one were able to perform the analytic integration over the phase space of final-state partons, the method can also be applied to higher-order cross-sections and differential spectra.

H1JET will print out a brief summary of the settings and parameters used, along with the Born cross-section σ_0, followed by a five-column table. The first three entries of each row specifies the lower end, the midpoint, and the upper end of each

p_T bin. The fourth entry is $\mathrm{d}\sigma/\,\mathrm{d}p_T$ evaluated at the midpoint of the corresponding p_T bin. The fifth entry is the integrated cross-section $\sigma(p_T)$ with a lower bound in p_T corresponding to the lower end of the given p_T bin. It should be emphasised that the fundamental object computed is $\mathrm{d}\sigma/\,\mathrm{d}p_T$. The integrated cross-section $\sigma(p_T)$ is obtained by summing $\mathrm{d}\sigma/\,\mathrm{d}p_T$ over the range and multiplying by the bin width. Hence, a reliable estimate of $\sigma(p_T)$ is obtained only if the binning is fine enough.

An example of the resulting p_T spectrum with default settings from H1JET is shown in Figure 5.2.

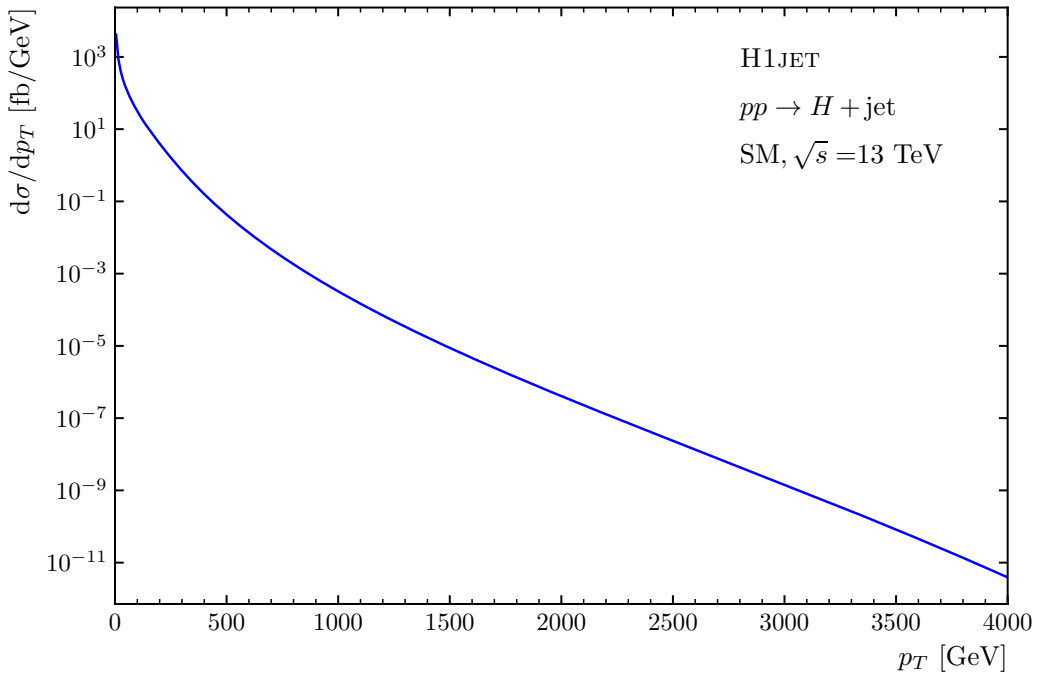

Figure 5.2. The p_T distribution for the SM process $pp \to H + \text{jet}$ from H1JET with default settings.

5.3 Implemented Models

This section explains the different physics models that are built-in and available in H1JET, including the SM, a CP-odd Higgs, a simplified SUSY model, and composite Higgs models with a single or multiple top-partners. In addition, H1JET is very flexible and can be easily interfaced to use a custom user-specified process, as explained in section 5.7.

A comparison between the various built-in models is shown in Figure 5.3. Default SM parameters has been used with $m_{\tilde{t}_1} = 600$ GeV, $\Delta m = 200$ GeV, $\tan\beta = 5$,

$m_T = 1.7$ TeV, $\sin^2\theta_{\tilde{t}} = \sin^2\theta_T = 0.1$, and $f = 900$ GeV, and considering the **M4$_5$** model as the explicit top-partner model.

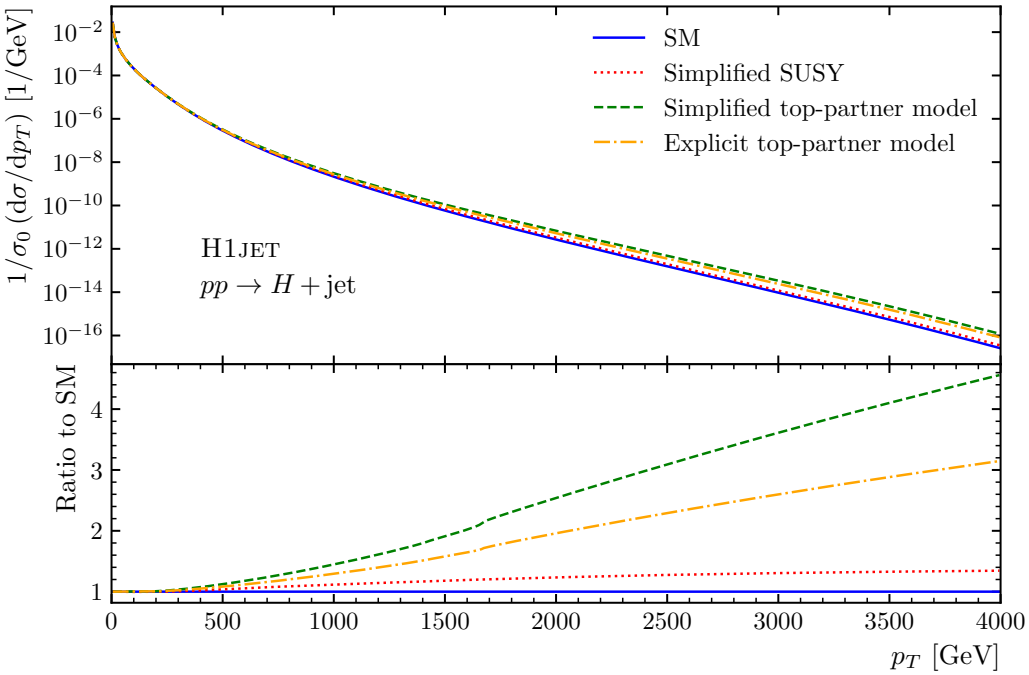

Figure 5.3. Comparison between the CP-even Higgs p_T distributions for various built-in models.

5.3.1 CP-Even and CP-Odd Higgs Production

Both CP-even and CP-odd Higgs production are loop-induced processes. The amplitudes for $2 \to 1$ processes are taken from ref. [108]. For CP-even Higgs production in $2 \to 2$, the amplitudes are taken from ref. [109], and their interface is adapted from HERWIG 6 [110]. The CP-odd $2 \to 2$ amplitudes are from ref. [97].

The interaction between the CP-odd Higgs H and a SM quark q is,

$$\mathcal{L} \supset i\tilde{\kappa}_q \frac{m_q}{v} \bar{q}\gamma_5 q H\,, \tag{5.15}$$

where the implementation in H1JET uses by default $\tilde{\kappa}_t = 1$ and $\tilde{\kappa}_b = 0$. Both parameters can be changed in the program.

5.3.2 Simplified SUSY

H1JET includes a simplified SUSY model with two stops $\tilde{t}_1$ and $\tilde{t}_2$ in the quark loops, as considered in refs. [111] and [112]. The first stop mass $m_{\tilde{t}_1}$ will need to be set to a non-zero value by the user. The second stop mass will then be given by

$$m_{\tilde{t}_2} = \sqrt{m_{\tilde{t}_1}^2 + (\Delta m)^2}\,, \tag{5.16}$$

where the mass separation Δm can likewise be set by the user.

The stop Yukawa coupling factors will be given by

$$\kappa_{\tilde{t}_1} = \frac{m_t^2}{m_{\tilde{t}_1}^2}\left[\alpha_1 \cos^2\theta_{\tilde{t}} + \alpha_2 \sin^2\theta_{\tilde{t}} + 2 - \frac{(\Delta m)^2}{2m_t^2}\sin^2(2\theta_{\tilde{t}})\right], \tag{5.17}$$

$$\kappa_{\tilde{t}_2} = \frac{m_t^2}{m_{\tilde{t}_2}^2}\left[\alpha_1 \sin^2\theta_{\tilde{t}} + \alpha_2 \cos^2\theta_{\tilde{t}} + 2 + \frac{(\Delta m)^2}{2m_t^2}\sin^2(2\theta_{\tilde{t}})\right], \tag{5.18}$$

where

$$\alpha_1 = \frac{m_Z^2}{m_t^2}\cos(2\beta)\left[1 - \frac{4}{3}\sin^2\theta_W\right], \tag{5.19}$$

$$\alpha_2 = \frac{4}{3}\frac{m_Z^2}{m_t^2}\cos(2\beta)\sin^2\theta_W\,. \tag{5.20}$$

Note that m_t, m_Z, $\sin^2\theta_W$, $\sin^2\theta_{\tilde{t}}$, and $\tan\beta$ can all be specified by the user.

5.3.3 Simplified Top-Partner Model

H1JET allows the calculation of Higgs production via loops of top-partners in addition to SM top loops, for a simplified composite Higgs model, where the compositeness scale f is set to infinity. The user can specify the top-partner mass m_T and the top-partner mixing angle, θ_T.

The SM top Yukawa factor can be modified by the mixing angle,

$$\kappa_t \to \kappa_t \cos^2\theta_T\,. \tag{5.21}$$

The top-partner Yukawa factor will likewise be modified

$$\kappa_T \to \kappa_T \sin^2\theta_T\,. \tag{5.22}$$

Both Yukawa factors, κ_t and κ_T, can be specified by the user.

5.3.4 Explicit Top-Partner Model

The top-partner can also be considered in the explicit composite Higgs models of ref. [113], all with finite f. Four different models are implemented, $\mathbf{M1_5}$, $\mathbf{M1_{14}}$, $\mathbf{M4_5}$, and $\mathbf{M4_{14}}$, which modify the Yukawa coupling factors in the following way

$\mathbf{M1_5}$	$\kappa_b \to \kappa_b c_\varepsilon$ $\kappa_t \to \kappa_t c_\varepsilon \cos^2\theta_L$ $\kappa_T \to \kappa_T c_\varepsilon \sin^2\theta_L$ $\tilde{\kappa}_b = \tilde{\kappa}_t = \tilde{\kappa}_T = 0$
$\mathbf{M1_{14}}$	$\kappa_b \to \kappa_b \frac{2c_\varepsilon^2-1}{c_\varepsilon}$ $\kappa_t \to \kappa_t \frac{2c_\varepsilon^2-1}{c_\varepsilon} \cos^2\theta_L$ $\kappa_T \to \kappa_T \frac{2c_\varepsilon^2-1}{c_\varepsilon} \sin^2\theta_L$ $\tilde{\kappa}_b = \tilde{\kappa}_t = \tilde{\kappa}_T = 0$
$\mathbf{M4_5}$	$\kappa_b \to \kappa_b c_\varepsilon$ $\kappa_t \to \kappa_t c_\varepsilon \left(\cos^2\theta_R - \frac{s_\varepsilon^2}{1+c_\varepsilon^2}\left(\cos^2\theta_L - \cos^2\theta_R\right)\right)$ $\kappa_T \to \kappa_T c_\varepsilon \left(\sin^2\theta_R - \frac{s_\varepsilon^2}{1+c_\varepsilon^2}\left(\sin^2\theta_L - \sin^2\theta_R\right)\right)$ $\tilde{\kappa}_b = 0$ $\tilde{\kappa}_t = \frac{4c_\varepsilon s_\varepsilon}{\sqrt{2(1+c_\varepsilon^2)}}\mathrm{Im}(c_1)\sin\theta_R\cos\theta_R$ $\tilde{\kappa}_T = -\tilde{\kappa}_t$
$\mathbf{M4_{14}}$	$\kappa_b \to \kappa_b \frac{2c_\varepsilon^2-1}{c_\varepsilon}$ $\kappa_t \to \kappa_t \left(\frac{(2c_\varepsilon^2-1)}{c_\varepsilon}\cos^2\theta_R - \frac{s_\varepsilon^2 c_\varepsilon(8c_\varepsilon^2-3)}{1-3c_\varepsilon^2+4c_\varepsilon^4}\left(\cos^2\theta_L - \cos^2\theta_R\right)\right)$ $\kappa_T \to \kappa_T \left(\frac{(2c_\varepsilon^2-1)}{c_\varepsilon}\sin^2\theta_R - \frac{s_\varepsilon^2 c_\varepsilon(8c_\varepsilon^2-3)}{1-3c_\varepsilon^2+4c_\varepsilon^4}\left(\sin^2\theta_L - \sin^2\theta_R\right)\right)$ $\tilde{\kappa}_b = 0$ $\tilde{\kappa}_t = \frac{4s_\varepsilon(1-2s_\varepsilon^2)}{\sqrt{2(1-3c_\varepsilon^2+4c_\varepsilon^4)}}\mathrm{Im}(c_1)\sin\theta_R\cos\theta_R$ $\tilde{\kappa}_T = -\tilde{\kappa}_t$

where the $\tilde{\kappa}$'s are the CP-odd couplings, and,

$$s_\varepsilon = \frac{v}{f}\,, \qquad \text{and} \qquad c_\varepsilon = \sqrt{1-s_\varepsilon^2}\,. \tag{5.23}$$

For $\mathbf{M1_5}$ and $\mathbf{M1_{14}}$, the user can set the mixing angle θ_L, while for $\mathbf{M4_5}$ and $\mathbf{M4_{14}}$, the user sets the angle θ_R. The reason for this is to be able to reproduce the $f \to \infty$

limit, where $\theta_T = \theta_L, \theta_R$ depending on the chosen model. When needed, the angles θ_L and θ_R are derived one from the other by using the relation

$$m_t^2 \tan^2 \theta_L = m_T^2 \tan^2 \theta_R \,. \tag{5.24}$$

Beyond that the user can set the imaginary part of the c_1 coefficient, $\mathrm{Im}(c_1)$, and the compositeness scale, f.

5.3.5 Multiple Top-Partners

H1JET makes it possible to include multiple top-partners in the particle loops. To do that, it will be necessary to specify an input file with the masses and Yukawa coupling factors for each particle running in the loop, including SM quarks.

The dimensionless Yukawa couplings can be specified for both the CP-even case, κ_q, and the CP-odd case, $\tilde{\kappa}_q$, with the following Lagrangian,

$$\mathcal{L} \supset -m_q \bar{q} q - \kappa_q \frac{m_q}{v} \bar{q} q H + i \tilde{\kappa}_q \frac{m_q}{v} \bar{q} \gamma_5 q H \,, \tag{5.25}$$

where m_q is the mass of the given top-partner.

The loop approximation for each top-partner can also be specified, allowing exact mass effects and large mass approximations for both fermionic and scalar top-partners.

By using such an input file, it is possible to explicitly specify masses, couplings and loop approximations for an arbitrary number of fermions and scalars. This would also allow a user to implement a specific SUSY model with more supersymmetric partners, each with the appropriate coupling.

5.4 Implementation of Scalar Integrals

Particular care has been taken to the implementation of the scalar integrals relevant for Higgs production, and the handling of the harmonic dilogarithms that shows up in the expressions.

The relevant scalar integrals are the two-point (bubbles), three-point (triangles), and four-point (boxes) scalar functions. These will depend on an internal mass m, and the Mandelstam variables, s, t, and u. The scalar integrals can be written in terms of logarithms and dilogarithms with complex arguments which require appropriate

analytic continuations. These have been recast into harmonic polylogarithms $H(\vec{w}, z)$ which are evaluated using Chaplin [114]. Real arguments, $z \in \mathbb{R}$, are interpreted by Chaplin as $z + i\varepsilon$ for a vanishing ε, i.e. with the *plus* prescription. It is therefore important to ensure that the sign of the imaginary part of the argument of the scalar integrals is consistent with the convention of Chaplin.

5.4.1 Bubbles

The bubble integral is defined as

$$B_0(s) = 2 - \sqrt{1 - \frac{4(m^2 - i\varepsilon)}{s}} \ln\left[-\frac{z}{1-z}\right], \tag{5.26}$$

where

$$z = \frac{1}{2}\left(1 + \sqrt{1 - \frac{4(m^2 - i\varepsilon)}{s}}\right). \tag{5.27}$$

The argument of the logarithm in Eq. (5.26) has a different form according to the value of s,

$$-\frac{z}{1-z} = \begin{cases} -\dfrac{1+\sqrt{1+\frac{4m^2}{|s|}}}{1-\sqrt{1+\frac{4m^2}{|s|}}}, & s < 0\,, \\ -\dfrac{1+i\sqrt{\frac{4m^2}{s}-1}}{1-i\sqrt{\frac{4m^2}{s}-1}}, & 0 < s < 4m^2\,, \\ -\dfrac{1-\sqrt{1-\frac{4m^2}{s}}}{1-\sqrt{1-\frac{4m^2}{s}}} - i\varepsilon\,, & s > 4m^2\,. \end{cases} \tag{5.28}$$

Note that the only case in which one needs a small imaginary part is the case $s > 4m^2$. This imaginary part has the opposite convention as in Chaplin. As a solution, the argument of the logarithm is inverted and the identity $\ln z = -\ln(1/z)$ can be used. In practice, after an appropriate analytic continuation of the square root, the z is defined as

$$z \equiv \begin{cases} \dfrac{1}{2}\left(1 + \sqrt{1 - \dfrac{4m^2}{s}}\right), & \dfrac{4m^2}{s} < 1\,, \\ \dfrac{1}{2}\left(1 + i\sqrt{\dfrac{4m^2}{s} - 1}\right), & \dfrac{4m^2}{s} > 1\,, \end{cases} \tag{5.29}$$

and the bubble can implemented as

$$B_0(s) = 2 - (2z-1)\, H\left(1; \frac{1}{z}\right) . \tag{5.30}$$

Note that a logarithm of a negative number can also be correctly analytically continued by using the default Fortran implementation of the complex logarithm. As for CHAPLIN, Fortran assumes that a negative number has a small positive imaginary part. Therefore, in the case of a small negative imaginary part, the relation $\ln z = -\ln(1/z)$, which gives the correct analytic continuation, can still be used.

5.4.2 Triangles

The triangle integral $C_0(s)$ is defined as

$$C_0(s) = \frac{1}{2s} \ln^2\left[-\frac{z}{1-z}\right] , \tag{5.31}$$

where z is given in Eq. (5.27). For $s > 4m^2$, again, the argument of the logarithm has the opposite sign with respect to what is implicitly assumed by CHAPLIN. Therefore, the argument of the logarithm is inverted again, and using the definition of z in Eq. (5.29), the triangle is implemented as

$$s\, C_0(s) = H\left(1, 1; \frac{1}{z}\right) . \tag{5.32}$$

5.4.3 Boxes

The scalar four-point function with three massless (the gluons) and one massive (the Higgs boson) external lines is given by [109],

$$\begin{aligned} D(s,t) = \frac{1}{st} \int_0^1 \frac{\mathrm{d}x}{x(1-x) + m^2 u/(ts)} \Bigg[&- \ln\left(1 - i\varepsilon - \frac{m_H^2}{m^2} x(1-x)\right) \\ &+ \ln\left(1 - i\varepsilon - \frac{s}{m^2} x(1-x)\right) + \ln\left(1 - i\varepsilon - \frac{t}{m^2} x(1-x)\right)\Bigg] , \end{aligned} \tag{5.33}$$

which can be expressed in terms of complex dilogarithms by using the exact result

$$\frac{1}{st}\int_0^1 \frac{\mathrm{d}x}{x(1-x)+m^2u/(ts)} \ln\left(1-i\varepsilon-\frac{v}{m^2}x(1-x)\right) = \frac{2}{\sqrt{1+4m^2u/(ts)}}\times \\ \times\left[\mathrm{Li}_2\left(\frac{x_-}{x_--y}\right)-\mathrm{Li}_2\left(\frac{x_+}{x_+-y}\right)+\mathrm{Li}_2\left(\frac{x_-}{y-x_+}\right)-\mathrm{Li}_2\left(\frac{x_+}{y-x_-}\right)\right. \\ \left.+\ln\left(\frac{-x_-}{x_+}\right)\ln\left(1-i\varepsilon-\frac{v}{m^2}x_-x_+\right)\right], \quad (5.34)$$

where

$$x_\pm \equiv \frac{1}{2}\left(1\pm\sqrt{1+\frac{4m^2u}{ts}}\right), \quad (5.35)$$

are real numbers, with $x_+ > 1$ and $x_- < 0$, and

$$y \equiv \frac{1}{2}\left(1+\sqrt{1-\frac{4(m^2-i\varepsilon)}{v}}\right), \quad (5.36)$$

acquires an imaginary part according to the value of v. In particular, keeping track of the imaginary part of y yields

$$y = \begin{cases} \frac{1}{2}\left(1+\sqrt{1+\frac{4m^2}{|v|}}\right)-i\varepsilon\,, & v<0\,, \\ \frac{1}{2}\left(1+i\sqrt{\frac{4m^2}{v}-1}\right), & 0<v<4m^2\,, \\ \frac{1}{2}\left(1+\sqrt{1-\frac{4m^2}{v}}\right)+i\varepsilon\,, & v>4m^2\,. \end{cases} \quad (5.37)$$

For the case $0 < v < 4m^2$, Chaplin can be used to evaluate the dilogarithms without issues. However, for $v < 0$, $x_-/(x_- - y)$ and $x_+/(y - x_-)$ will acquire a small positive imaginary part, while $x_+/(x_+ - y)$ and $x_-/(y - x_+)$ will acquire a small negative imaginary part. The reverse happens for $v > 4m^2$. Hence, some formal manipulations are necessary to use the harmonic polylogarithms provided by Chaplin.

For a complex argument, $z \in \mathbb{C}$, to the dilogarithms, the usual definitory relation $\mathrm{Li}_2(z) = H(0,1,z)$ will be used in the code. For an argument $z = x - i\varepsilon$ with $x \in \mathbb{R}$

and the '$-i\varepsilon$' prescription, the identities

$$\begin{aligned}\mathrm{Li}_2\left(z = x - i\varepsilon\right) &= -H(0,-1;-z) \\ &= -H\left(0,1;\frac{1}{z}\right) - \frac{\pi^2}{6} - H(0,0;-z) \\ &= -H\left(0,1,1-z\right) + \frac{\pi^2}{6} + H(1;1-z)H(-1;-z)\,, \end{aligned} \tag{5.38}$$

has been used to ensure the correct sign, since both $-z$ and $1/z$ will be with the '$+i\varepsilon$' prescription. The identities in Eq. (5.38) may differ due to numerical instability, hence the identity giving the smallest imaginary part will be selected by the code.

5.5 Technical Details

H1JET is written in Fortran 95, with two helper scripts written in Python 3.

Luminosities are provided by HOPPET [67], while PDF sets are provided by LHAPDF [66]. Evaluation of the harmonic polylogarithms that shows up in the scalar integrals is handled by CHAPLIN [114].

An online interface is available at

`https://h1jet.hepforge.org/online`

written in HTML, JavaScript, and PHP. Such an online interface is possible due to the speed and ease-of-use of H1JET. Besides printing the normal output of H1JET, the online interface includes automatic plotting of the histogram.

5.5.1 Adaptive Gaussian Quadrature Integration

The one-dimensional integration in Eq. (5.14) is handled numerically by an *adaptive Gaussian quadrature integration* routine implemented in HOPPET. The method first approximates the definite integral with Gaussian quadratures, which is a weighted sum of values of the function at specific points in the interval. Applying a n-point Gaussian quadrature rule provides an approximation

$$g_n = \frac{b-a}{2}\sum_{i=1}^{n} w_i f\left(\frac{b-a}{2}\xi_i + \frac{a+b}{2}\right) \approx \int_a^b f(x)\,\mathrm{d}x\,, \tag{5.39}$$

where w_i are the weights and ξ_i are from a change of variables $\mathrm{d}x/\,\mathrm{d}\xi = (b-a)/2$. An error is then estimated and compared to the specified accuracy. If the accuracy

has not yet been met, the adaptive algorithm uses the additive property of definite integrals,

$$\int_a^b f(x)\,\mathrm{d}x = \int_a^m f(x)\,\mathrm{d}x + \int_m^b f(x)\,\mathrm{d}x\,, \tag{5.40}$$

for a midpoint $m = (a+b)/2$. The adaptive integration runs recursively on subdivisions of the interval until the desired accuracy is met. Pseudocode for the numerical integration procedure is given in Algorithm 1.

Algorithm 1 Adaptive Gaussian quadrature integration

procedure INTEGRATE(f, a, b, ε) ▷ Integrate f in range $[a, b]$ to accuracy ε
  $g_8 \approx \int_a^b f(x)\,\mathrm{d}x$ ▷ 8-point Gaussian quadrature approximation
  $g_{16} \approx \int_a^b f(x)\,\mathrm{d}x$ ▷ 16-point Gaussian quadrature approximation
  $r \leftarrow |g_{16} - g_8|$ ▷ Estimate error
  if $r \leq \varepsilon\,(1 + |g_{16}|)$ **then** ▷ Compare error to specified accuracy
    $Q \leftarrow g_{16}$ ▷ Reached accuracy
  else
    $m \leftarrow (a+b)/2$ ▷ Subdivide interval
    $Q \leftarrow$ INTEGRATE(f, a, m, ε) + INTEGRATE(f, m, b, ε) ▷ Run recursively
  end if
  return Q
end procedure

This method for numerical integration results in a very fast runtime for H1JET of usually less than one second, depending of course on the specified integration accuracy. However, it requires a specific formulation of $\mathrm{d}\sigma/\,\mathrm{d}\mathcal{O}$ for any observable $\mathcal{O}$, so any new differential distribution will have to be hard-coded in the code, in contrast to the Monte Carlo method which provides complete kinematical information for each phase space point, but with the payoff of a much longer runtime.

5.6 Validation

All of the processes implemented in H1JET have been compared to the corresponding implementations in SUSHI [105,106], and have all been found to be in agreement. The relative ratio between the H1JET result and the SUSHI result for the p_T distribution for the CP-odd Higgs is shown in Figure 5.4, and is found to be in agreement within the Monte Carlo error of SUSHI for a large range of p_T values. Overall the agreement with SUSHI is within 3×10^{-4}. Note that the largest discrepancies were observed in the low p_T region. The H1JET results for low p_T values can be validated by

comparing them to the approximate expression valid at low p_T,

$$\frac{\mathrm{d}\sigma}{\mathrm{d}p_T} \xrightarrow{p_T \to 0} \sigma_0 \left[4\, C_A \frac{\alpha_s}{\pi} \frac{1}{p_T} \left(\ln \frac{m_H}{p_T} + \mathcal{O}(1) \right) \right] , \tag{5.41}$$

where σ_0 is the total Born cross-section for $gg \to H$. Figure 5.5 shows $\frac{p_T}{\sigma_0} \left(\frac{\mathrm{d}\sigma}{\mathrm{d}p_T} \right)$ with the first term of Eq. (5.41) subtracted, as a function of $\ln \frac{p_T}{m_H}$. For $p_T \to 0$ this goes nicely towards a constant as expected.

The relative ratio between the H1JET and SUSHI results for the simplified SUSY model are shown in Figure 5.6 and is within 2×10^{-4}. Again the low p_T behaviour can be checked by comparing to the resummed expression in Figure 5.7.

It should be noted that the numerical accuracy of H1JET depends not only on the accuracy of the numerical integration, but also on the numerical accuracy of HOPPET, which is used to compute the PDF evolution, and of CHAPLIN, which computes the scalar integrals. Various internal parameters of the two libraries have been modified, and the obtained differences are less than permille level. So, a conservative estimate of the numerical uncertainty of H1JET is 1×10^{-3}.

5.7 Adding New Processes to H1JET

H1JET can be interfaced to use the squared matrix element evaluated from a custom Fortran code. The Fortran code should provide a Born-level $\left|\mathcal{M}(\hat{s}, \hat{t}, \hat{u})\right|^2$ for each channel, gg, gq, qg, and $q\bar{q}$. A helper script, written in Python 3, will read in the input Fortran code, identify new model parameters, and dress the code such that it can be compiled with H1JET.

A potential pipeline would be to start with a FEYNRULES [115] model file, convert it to a FEYNARTS [116] model, produce a squared matrix element with FEYNCALC [117–119], and write it to a Fortran output file. However, the matrix element could just as well be written by some other program, or even by hand.

5.7.1 Example: Axion-Like-Particle Effective Theory

The example considered in this section is the production of a light axion-like-particle (ALP), a, along with a jet. For simplicity, only the gluon-fusion channel is considered,

$$gg \to ga\,, \tag{5.42}$$

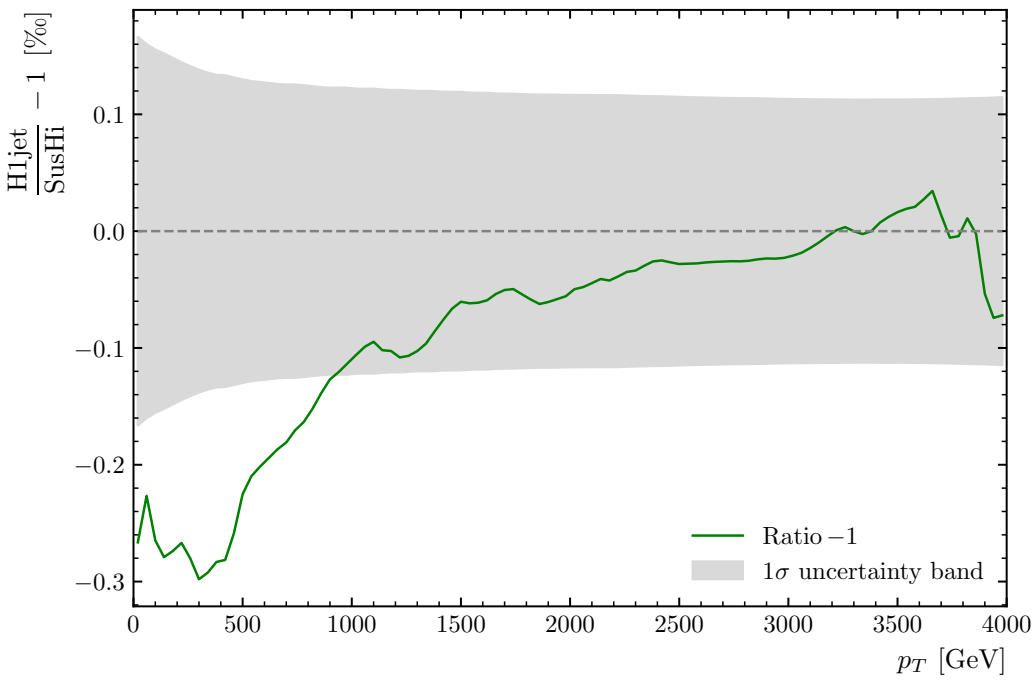

Figure 5.4. The relative difference in permille between the H1JET result and that of SUSHI for the p_T distribution for a CP-odd Higgs. The grey band indicates the Monte Carlo error of SUSHI.

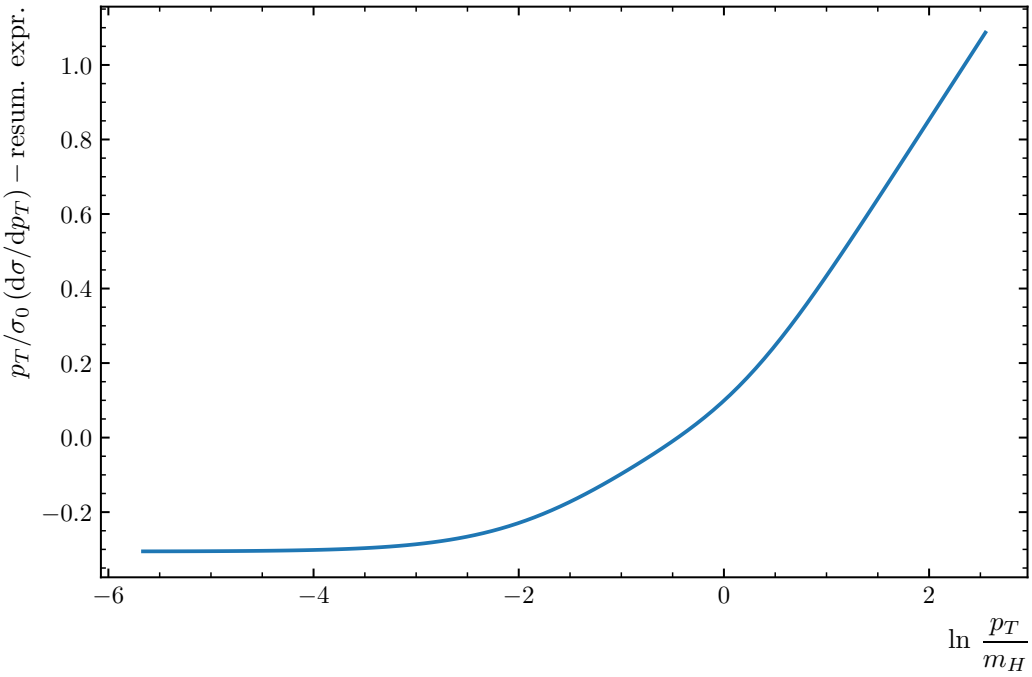

Figure 5.5. The CP-odd distribution $\frac{p_T}{\sigma_0}\left(\frac{\mathrm{d}\sigma}{\mathrm{d}p_T}\right)$ with the first term of the p_T resummation subtracted, as a function of $\ln \frac{p_T}{m_H}$. For low p_T values it convergences to a constant value.

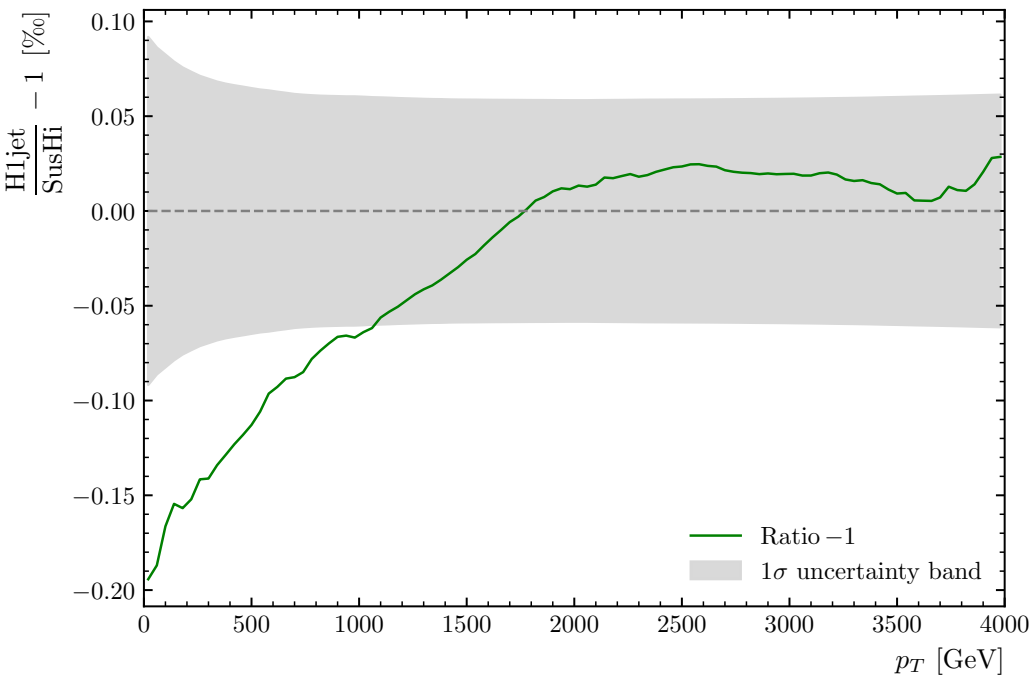

Figure 5.6. The relative difference in permille between the H1JET result and that of SUSHI for the p_T distribution in SUSY. The grey band indicates the Monte Carlo error of SUSHI.

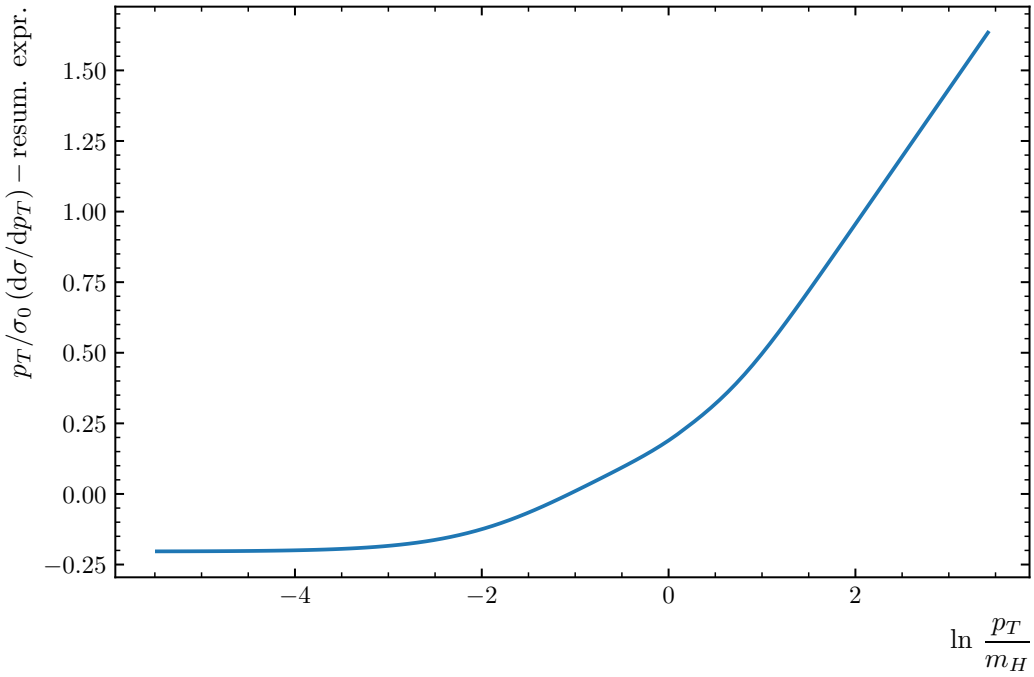

Figure 5.7. The SUSY distribution $\frac{p_T}{\sigma_0}\left(\frac{\mathrm{d}\sigma}{\mathrm{d}p_T}\right)$ with the first term of the p_T resummation subtracted, as a function of $\ln\frac{p_T}{m_H}$. For low p_T values it convergences to a constant value.

but all other channels could likewise have been considered in H1JET. Gluon-fusion ALP production is a tree-level process due to an effective ALP-gluon coupling,

$$\delta\mathcal{L}_a \supset -c_{\tilde{G}}\frac{a}{f_a}G^a_{\mu\nu}\tilde{G}^{\mu\nu\,a} \tag{5.43}$$

where $c_{\tilde{G}}$ is the Wilson coefficient and f_a is the ALP suppression scale, and where $G^a_{\mu\nu}$ is the gluon field strength tensor and $\tilde{G}^a_{\mu\nu} = (1/2)\epsilon_{\mu\nu\rho\sigma}G^{a\rho\sigma}$ is its dual.

The BSM model and the associated FEYNRULES implementation are described and provided in ref. [120]. After converting to a FEYNARTS model, the amplitudes have been generated with FEYNCALC in Mathematica.

The squared matrix element for $gg \to ga$ as a function of Mandelstam variables s, t, and u, and ALP mass m_a is

$$\sum|\mathcal{M}|^2 = \frac{3c^2_{\tilde{G}}g_s^2}{f_a^2 stu}\Big[m_a^8 - 2m_a^6(t+u) + 3m_a^4(t+u)^2 - 2m_a^2(t+u)^3 + (t^2+tu+u^2)^2\Big]\,. \tag{5.44}$$

The p_T distribution of the implementation of gluon-fusion ALP-production in H1JET is shown in Figure 5.8.

Phenomenologically the ALP is similar to the CP-odd Higgs, and therefore the ALP result can be compared to the H1JET result for the CP-odd Higgs by using a single top quark in the loop with an infinite mass limit, resulting in an effective coupling between the CP-odd Higgs and the gluons. In fact, the respective ALP and CP-odd couplings are related by

$$\frac{c^2_{\tilde{G}}}{f_a^2} = \frac{\alpha_s^2}{64\pi^2 v^2}\,. \tag{5.45}$$

The comparison is shown in Figure 5.9, where the agreement is within 4×10^{-6}.

The ALP result have also been compared to the same FEYNRULES model used with MADGRAPH5_AMC@NLO [47]. While H1JET takes ~ 1 s to run, MADGRAPH5_AMC@NLO can take up to several hours to get comparable statistics due to it running a full Monte Carlo integration. Both programs agree within the Monte Carlo errors. In addition, MADGRAPH5_AMC@NLO runs into numerical instabilities at low p_T, while H1JET has by construction the correct behaviour. It should be stressed, however, that H1JET is not a replacement for a full Monte Carlo study implementing realistic experimental cuts and non-perturbative QCD effects. Instead, H1JET provides fast parton-level result, useful to phenomenologists or BSM physicists to quickly assess deviations of a specified new physics model to the SM.

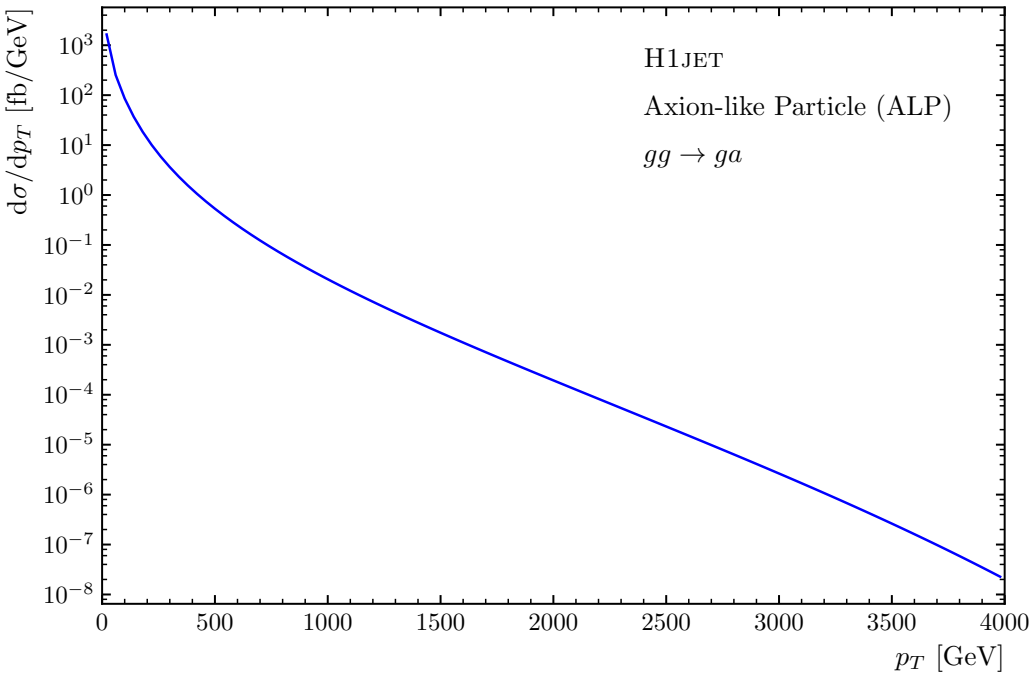

Figure 5.8. The p_T distribution for the process $gg \to ga$ from H1JET with the amplitude from the user interface.

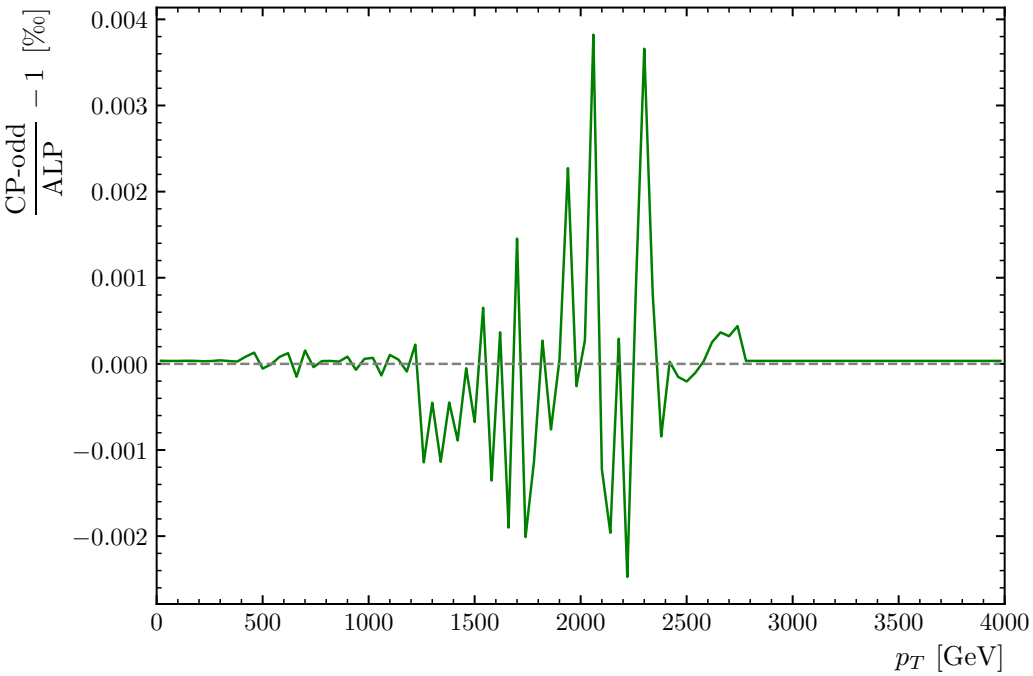

Figure 5.9. The relative ratio in permille between the CP-odd result and the result with the ALP amplitude.

An added benefit of H1JET not being based on a Monte Carlo integration, is that it is possible to separate the interference terms between different contributions very precisely, which is difficult with Monte Carlo event generators.

5.8 Current Version and Future Plans

H1JET allows for a fast computation of the transverse momentum distribution of a colour singlet. H1JET is similar in spirit to SUSHI, but is incomparably faster, returning the p_T spectrum in about a second. This speed is achieved by utilising an adaptive Gaussian quadrature integration method instead of traditional Monte Carlo integration, and allows H1JET to perform parameter scans in seconds, and to take into account mass effects in specific models. H1JET can therefore be used to assess deviations of selected new physics models from the SM behaviour, and can quickly obtain distributions of relevance for precision phenomenology.

H1JET implements various processes and models out-of-the-box, including SUSY and composite Higgs. Loop integrals can be computed either exactly or in the infinite-mass limit. H1JET is very flexible, with the only process-dependent input being the specified amplitude in terms of Mandelstam variables. This amplitude can be computed by the user either manually, or with the use of automated programs such as FEYNCALC, and connected to the program through a simple interface.

An additional strength of H1JET is the possibility to provide input files to obtain results for an arbitrary number of fermions and scalars in the loops, by providing appropriate masses and couplings. This could be used, for instance, to implement the full MSSM instead of the provided simplified SUSY model. A future version of H1JET could include a helper script allowing for automatic calculation of the necessary MSSM couplings for H1JET given input model parameters.

The functionality of H1JET can be extended in various ways. The currently implemented processes are computed at the lowest order in QCD, but nothing prevents the inclusion of higher orders, provided that all coloured particles are integrated over. In addition, besides the p_T spectrum, the jet rapidity spectrum could be computed by implementing the corresponding expression for the differential cross-section.

HOPPET is able to efficiently evaluate convolutions of parton luminosities with externally defined coefficient functions. This can be utilised in a future version of H1JET, wherein a user can specify a coefficient function for a given process, allowing

quick computation of a given differential distribution. This could greatly extend the flexibility of H1JET.

As an example, for the Drell-Yan process, $q\bar{q} \to Z \to \ell^+\ell^-$, the invariant mass spectrum takes the schematic form

$$\frac{\mathrm{d}\sigma}{\mathrm{d}M_{\ell\ell}^2} = \int_\tau^1 \frac{\mathrm{d}z}{z}\, C(z)\, \mathcal{L}\left(\frac{\tau}{z}, \mu_F\right) , \tag{5.46}$$

with a convolution between the coefficient function C and the parton luminosity $\mathcal{L}$, where $\tau = M_{\ell\ell}^2/s$.

Finally, an educational version of the online interface is planned for the purposes of public outreach. Due to the fast run-time and relative simplicity of the input parameters, plans are to create a simplified version of H1JET as a web application with pedagogical explanations of the underlying physics. The intended audience are, in particular, high school or undergraduate students focusing on physics.

6

Higgs Interference Effects at NLO in the 1-Higgs-Singlet Model

The research study outlined in this chapter is partially published in ref. [121], but further includes a full NLO calculation of the signal-background interference[1] that was not included in the original publication. The code used for the additional results is available at ref. [122].

6.1 Motivation

Many BSM models maintain the assumption of a complex SU(2) doublet which acquires a vacuum expectation value leading to a physical Higgs boson, while also allowing for an extension of the Higgs sector with additional Higgs-like scalar particles. The simplest of such extensions is the *1-Higgs-singlet model* (1HSM) which introduces an additional real scalar singlet field which is neutral under the SM gauge groups. The 1HSM has been studied extensively [123–153], with the remaining viable parameter space after LHC Run 1 having been studied in refs. [154–157].

At the LHC, the ATLAS and CMS experiments have conducted searches for heavier Higgs-like bosons in various decay channels, including $t\bar{t}$ [158, 159]. The top quark is expected to play a large role in the search for new physics at the LHC, due to its large mass and its corresponding strong Yukawa coupling to the Higgs boson.

[1] With the exception of the non-factorisable contributions, which are expected to be small.

So far, most heavy Higgs searches have been focused on so-called "bump-hunting", which attempts to establish a significant excess of events in the invariant mass spectrum of the final-state particles of the heavy resonance. However, as shown in Figure 6.1, the "bump" caused by the Breit–Wigner line shape for the heavy resonance can be a tiny correction to the overall signal. The majority of the signal will come from the interference between the heavy Higgs resonance and the continuum QCD background[2]. In addition, there is little resemblance in the line shape of the interference and the signal. The interference exhibits a large dip structure around the resonance mass. A shoulder in the heavy Higgs signal extending down to $2m_t$ can be observed in Figure 6.1, due to the low-mass tail of the Breit–Wigner line shape being enhanced by the convolution with the gluon PDFs which are peaked at $M_{t\bar{t}} \to 0$. The low-mass shoulder does not effectuate an increase in the signal alone but instead enhances the interference.

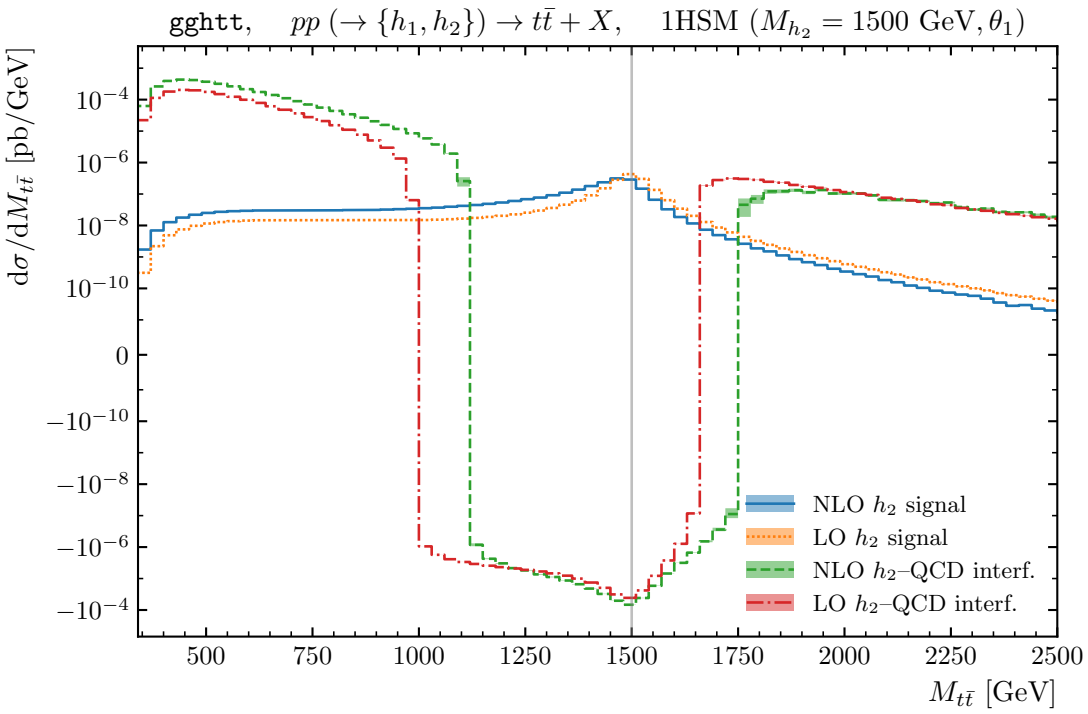

Figure 6.1. The differential distribution over the invariant mass $M_{t\bar{t}}$ for the process $pp\ (\to \{h_1, h_2\}) \to t\bar{t} + X$ in the 1HSM extension for a benchmark point with a heavy Higgs mass $M_{h_2} = 1.5$ TeV.

[2]Here "continuum" refers to the fact that no heavy resonances shows up in the SM QCD process $pp \to t\bar{t} + X$, which means no Breit–Wigner line shape, and the invariant mass spectrum will therefore be monotonically decreasing for increasing $M_{t\bar{t}}$.

It should be noted that the term "signal" in Figure 6.1 refers to the resonance line shape from the heavy Higgs only. However, the Higgs resonance–QCD background interference is just as much a part of the signal, as it would vanish if the BSM amplitude was not present. This point should be stressed, as the interference effect is crucial to heavy Higgs searches.

This study considers an additional Higgs boson that is heavier than the discovered 125 GeV Higgs boson. Hence, the heavy Higgs signal is not only affected by the interference to the continuum QCD background but also by the interference between the heavy Higgs h_2 and the high-mass tail of the light Higgs h_1 [160], which has been taken into account in this study. Schematically, at LO, this has the form

$$|\mathcal{M}_{\mathrm{S}}|^2 = |\mathcal{M}_{h_1}|^2 + |\mathcal{M}_{h_2}|^2 + 2\,\mathrm{Re}\left(\mathcal{M}_{h_1}^{*}\mathcal{M}_{h_2}\right) , \tag{6.1}$$

with the last term giving the h_1–h_2 interference.

This study focus on the decay of the heavy Higgs resonance to a $t\bar{t}$ final-state at NLO,

$$pp\ (\to \{h_1, h_2\}) \to t\bar{t} + X\,. \tag{6.2}$$

Naturally, a more comprehensive study will also include other final-states such as W^+W^- and ZZ, but the top quark might play a special role in electroweak symmetry breaking due to its large Yukawa coupling – something that has been exploited in a wide range of BSM models, as well as in experimental settings to look for hints of new physics.

The peak-dip deformation of the Higgs resonance in $gg \to t\bar{t}$ due to signal–background interference was first studied for the SM in ref. [161], and in two-Higgs models for masses up to 750 GeV in refs. [162–164]. A detailed analytic study of the heavy Higgs line shape modification due to the signal-background interference in LO $gg \to t\bar{t}$ for scalar masses up to 1 TeV was presented in ref. [165]. The experimental sensitivity to additional heavy scalar resonances with a mass up to 1 TeV in several models for $gg \to t\bar{t}$ at the LHC, taking into account the signal–background interference, was studied in ref. [166]. In both ref. [166] and [163], the interference was calculated at LO and rescaled with the geometric average of inclusive K-factors for the signal and QCD background in order to approximate higher-order corrections. The study presented in this chapter extends this work by considering Higgs resonances in the mass range of 700 GeV to 3 TeV for integrated cross-sections and differential distributions. In particular, distributions over the invariant mass of

the $t\bar{t}$ system, $M_{t\bar{t}}$, as defined in Eq. (3.7), are considered.

Significantly, this study presents a full NLO calculation of the signal–background interference. As discussed in section 3.5, NLO corrections can be large for processes with a lot of colour annihilation such as Higgs production. It is also well known that flat, inclusive K-factors rarely model differential NLO corrections well. The results in ref. [121] considered the interference between the LO Higgs signal and the one-loop continuum QCD background. However, this is infrared (IR) divergent and additional contributions are required, as will be explained in section 6.3. The results presented here considers the heavy Higgs interference to the continuum QCD background at NLO. Hence, this study is an extension of the studies in ref. [121] and [166]. The effect of the NLO corrections to the signal and the interference can be seen in Figure 6.1. The NLO distribution of the heavy Higgs signal is shifted towards lower $M_{t\bar{t}}$ values compared to the LO distribution, due to gluon emissions from final-state radiation not being included in the calculation of the invariant mass.

6.2 The 1-Higgs-Singlet Model

As a minimal theoretically consistent BSM model with two Higgs bosons, this study will consider the 1-Higgs-singlet model (1HSM), which has a smaller parameter space compared to e.g. the two-Higgs-doublet model (2HDM). The next section will present the model and the considered benchmark points.

In the 1HSM, the SM Higgs sector is extended by an additional real scalar field, which is a singlet under all of the gauge groups of the SM, and which, like the SM Higgs, acquires a vacuum expectation value (VEV) under electroweak symmetry breaking. A detailed description of the model can be found in refs. [144, 167].

The most general gauge-invariant potential can be written as [124, 126]

$$V = \lambda\left(\phi^\dagger\phi - \frac{v^2}{2}\right)^2 + \frac{1}{2}M^2 s^2 + \lambda_1 s^4 + \lambda_2 s^2\left(\phi^\dagger\phi - \frac{v^2}{2}\right) + \mu_1 s^3 + \mu_2 s\left(\phi^\dagger\phi - \frac{v^2}{2}\right), \tag{6.3}$$

where s is the real singlet scalar, which mixes with the SM SU(2) Higgs doublet ϕ, given in Eq. (2.15).

To avoid vacuum instability, and that the potential is unbounded from below, the quartic couplings must satisfy

$$\lambda > 0\,, \quad \lambda_1 > 0\,, \quad \lambda_2 > -2\sqrt{\lambda\lambda_1}\,, \tag{6.4}$$

whereas the trilinear couplings μ_1 and μ_2 can be either positive or negative.

By considering the unitary gauge in Eq. (2.20), the potential in Eq. (6.3) can be rewritten in terms of the SM Higgs scalar H and the new singlet scalar s as

$$V = \frac{\lambda}{4}H^4 + \lambda v^2 H^2 + \lambda v H^3 + \frac{1}{2}M^2 s^2 + \lambda_1 s^4 + \frac{\lambda_2}{2}H^2 s^2 + \lambda_2 v H s^2 + \mu_1 s^3 + \frac{\mu_2}{2}H^2 s + \mu_2 v H s\,. \tag{6.5}$$

The mass eigenstates can be parameterised in terms of a mixing angle θ,

$$\begin{aligned} h_1 &= H\cos\theta - s\sin\theta\,, \\ h_2 &= H\sin\theta + s\cos\theta\,, \end{aligned} \tag{6.6}$$

where h_1 and h_2 constitutes the physical Higgs bosons of the 1HSM extension, and

$$\tan(2\theta) = \frac{-\mu_2 v}{\lambda v^2 - \frac{1}{2}M^2}\,, \qquad \text{with} \qquad -\frac{\pi}{4} < \theta < \frac{\pi}{4}\,, \tag{6.7}$$

under the condition $M^2 > 2\lambda v^2$. The model has six independent parameters, which are chosen to be M_{h_1}, M_{h_2}, θ, μ_1, λ_1, and λ_2. The dependent model parameters are

$$\lambda = \frac{\cos(2\theta)\left(M_{h_1}^2 - M_{h_2}^2\right) + M_{h_1}^2 + M_{h_2}^2}{4v^2}\,, \tag{6.8}$$

$$M^2 = \frac{M_{h_2}^2 - M_{h_1}^2 + \sec(2\theta)\left(M_{h_1}^2 + M_{h_2}^2\right)}{2\sec(2\theta)}\,, \tag{6.9}$$

$$\mu_2 = -\tan(2\theta)\frac{\lambda v^2 - \frac{1}{2}M^2}{v}\,. \tag{6.10}$$

The physical h_1 is assumed to be the light Higgs boson with a mass of $M_{h_1} = 125$ GeV in accordance with the experimentally observed boson.

The Yukawa couplings of the light and heavy Higgs bosons to the top quark will be modified by the mixing angle,

$$y_t^{h_1} = \cos^2(\theta)\sqrt{2}\frac{m_t}{v}\,, \qquad y_t^{h_2} = \sin^2(\theta)\sqrt{2}\frac{m_t}{v}\,. \tag{6.11}$$

This study considers four different masses of the heavy Higgs, $M_{h_2} = \{700, 1000, 1500, 3000\}$ GeV. For each heavy Higgs mass, two different values of the mixing angle, θ_1 and θ_2, are considered. These are given in Table 6.1 and constitute the eight different benchmark points considered in this study. The lower values of θ are consistent with theoretical and current experimental constraints [156, 157]. The perturbativity constraint $|\lambda| < 4\pi$ along with Eq. (6.8) imposes the condition $|\theta| < \theta_0$

which is satisfied of all eight benchmark points, as $\theta_0 \geq 0.42$ for 200 GeV $\lesssim M_{h_2} \leq 3$ TeV. The renormalisation group running of λ to high scales has not been taken into account.

M_{h_2} [GeV]	700	1000	1500	3000
θ_1	$\pi/15$ ≈ 0.21	$\pi/15$ ≈ 0.21	$\pi/22$ ≈ 0.14	$\pi/45$ ≈ 0.07
θ_2	$\pi/8$ ≈ 0.39	$\pi/8$ ≈ 0.39	$\pi/12$ ≈ 0.26	$\pi/24$ ≈ 0.13

Table 6.1. Higgs mixing angles θ_1 and θ_2 in the 1HSM for different masses of the heavy Higgs h_2, all with $M_{h_1} = 125$ GeV and $\mu_1 = \lambda_1 = \lambda_2 = 0$. These constitute the eight different model benchmark points.

The benchmark points are considered with vanishing coupling parameters μ_1, λ_1, and λ_2, with $\lambda_1 > 0$ in Eq. (6.4) treated as approximately zero. Despite of this, the decay widths for $h_2 \to h_1 h_1$ and $h_2 \to h_1 h_1 h_1$ are not zero, due to the H–s mixing. The partial decay widths $\Gamma(h_2 \to n \times h_1)$ for $n = \{2, 3, 4\}$ are given in Table 6.2.

6.3 NLO QCD Corrections to the Interference

This section will consider the QCD corrections to the interference between the Higgs signal and the continuum QCD background at NLO. Feynman diagrams will be used to illustrate the different contributions to the interference term, but it should be noted that only a subset of the relevant diagrams are shown here.

The interference between the loop-induced LO $gg \to \{h_1, h_2\} \to t\bar{t}$ signal and the LO continuum QCD background $gg \to t\bar{t}$ is at $\mathcal{O}(\alpha_s^2 \alpha)$ and shown in Figure 6.2.

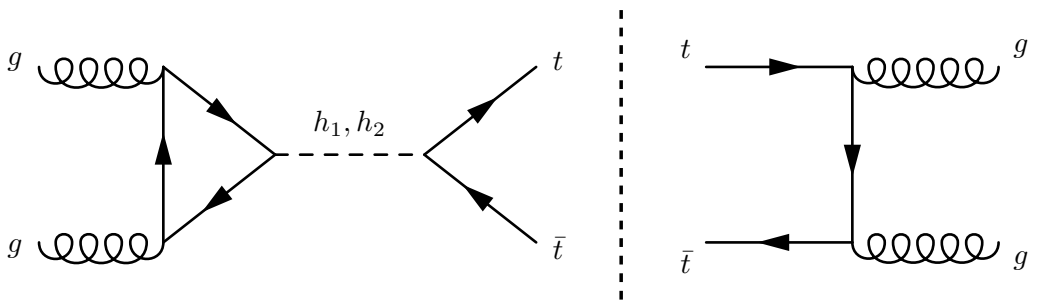

Figure 6.2. The interference between the loop-induced LO Higgs signal and the LO continuum QCD background.

The NLO QCD corrections to the interference is at $\mathcal{O}(\alpha_s^3\alpha)$ and will include both virtual and real corrections. The virtual corrections will include the interference between the loop-induced LO Higgs signal and the one-loop continuum QCD background shown in Figure 6.3. These contributions were considered in ref. [121]. However, the interference in Figure 6.3 is IR singular and requires dipole subtraction and real corrections to be predictive. The real corrections are not expected to be negligible, since soft-collinear gluon emissions can give a sizeable contribution to higher-order corrections to gluon-initiated processes. In addition, the normalisation of the bare IR divergent virtual amplitude will be arbitrary.

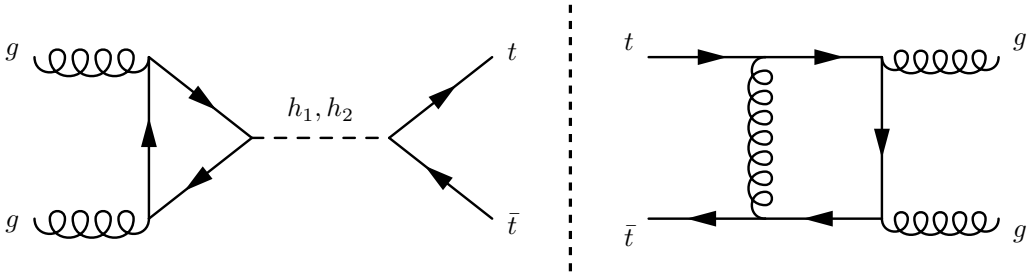

Figure 6.3. The interference between the LO Higgs signal and the virtual correction to the continuum QCD background at NLO.

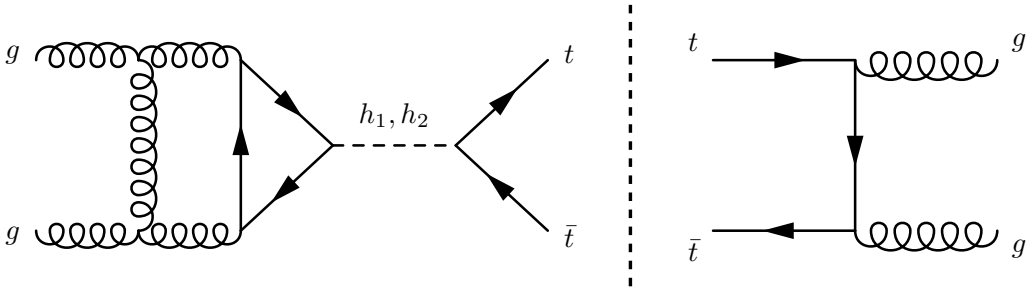

Figure 6.4. The interference between the two-loop corrections to the Higgs signal and the tree-level continuum QCD background.

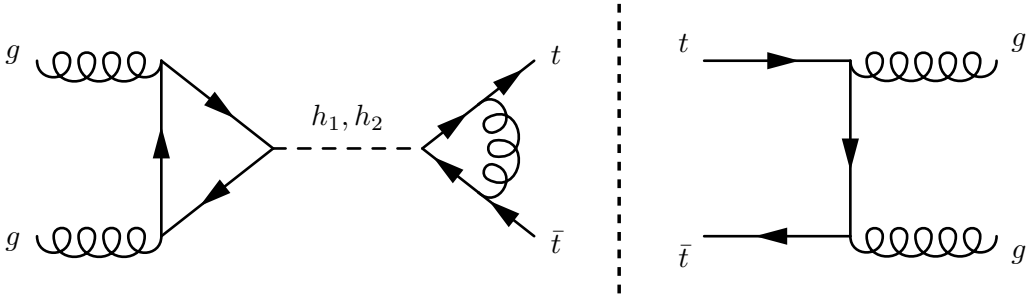

Figure 6.5. The interference between the loop corrections to the final-state of the Higgs signal and the tree-level continuum QCD background.

The virtual corrections at $\mathcal{O}(\alpha_s^3\alpha)$ will also include the interference between the two-loop virtual corrections to the Higgs signal and the tree-level continuum QCD background. These show up in three forms: *initial-state*, *final-state*, and *non-factorisable* corrections [163]. The initial-state corrections are well known [108, 168] and shown in Figure 6.4. The final-state corrections are likewise well known [169] and shown in Figure 6.5.

However, the non-factorisable corrections, connecting the initial- and final-state, are not currently known, as they are beyond current multi-loop technology. The non-factorisable corrections show up in double-box diagrams as in Figure 6.6.

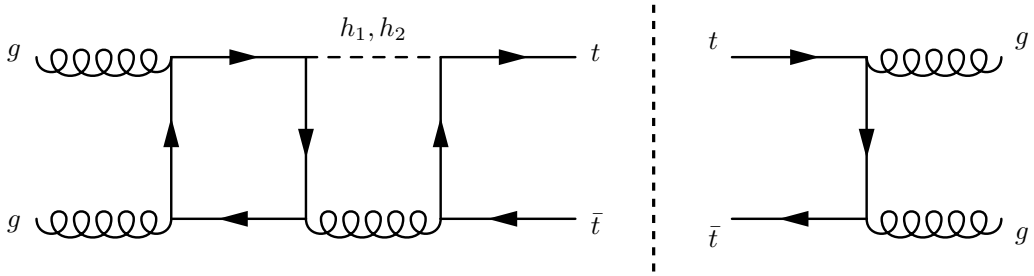

Figure 6.6. The interference between the non-factorisable corrections to the Higgs signal at NLO and the LO continuum QCD background.

The non-factorisable corrections to the two-loop amplitude can be considered in the *Higgs Effective Field Theory* (HEFT), where the top quark mass running in the loop is taken to be infinite, as in ref. [170]. In the HEFT model, the quark loop is replaced by an effective Higgs-gluon coupling, and the double-box reduces to a one-loop diagram [162]. This is shown in Figure 6.7. The factorisable corrections could still be considered with full top mass dependence. This will produce the correct IR structure, but will not be a good approximation in the case of a significantly off-shell light or heavy Higgs, which is the case in this study.

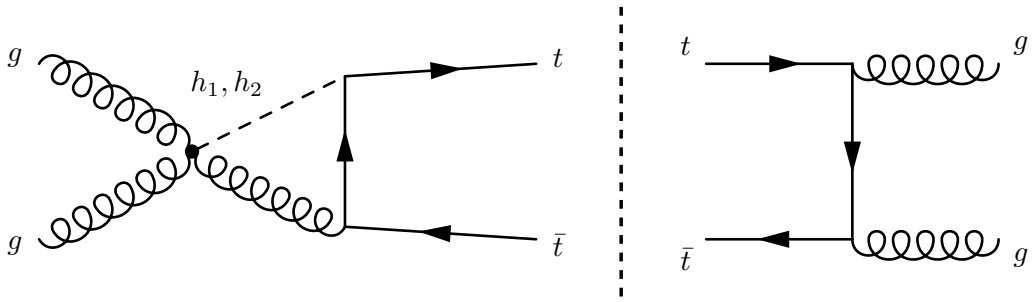

Figure 6.7. The interference between the non-factorisable corrections to the Higgs signal at NLO and the LO continuum QCD background, in the HEFT.

Alternatively, the non-factorisable double-box diagrams can be attempted to be calculated in the limit $p_T \gg m_t$, similar to what is done in ref. [171]. A third option is to perform a partial fractioning of the Higgs propagator to define the non-factorisable corrections in a gauge-invariant way. Then the soft-collinear approximation can be used in which the non-factorisable corrections factorise from the corresponding Born amplitudes [172, 173]. For the top case the non-factorisable corrections are expected to be small, suppressed by a factor $\Gamma_t/m_t \sim 1\%$ for the inclusive cross-section [174], and can be reasonably neglected. However, this is not true for the Higgs case for models with significant Higgs decay widths. In Table 6.3, the heavy Higgs decay width reach $\Gamma_{h_2}/m_{h_2} \sim 18\%$. In this case, the non-factorisable corrections may be important. The non-factorisable corrections are not included in this study, but future work could study their impact by considering them in an expansion in Γ_{h_2}/m_{h_2}.

Finally, in the unresolved IR limit, it is necessary to include the $\mathcal{O}(\alpha_s^3\alpha)$ interference between the $pp \to \{h_1, h_2\} \to t\bar{t} + \text{jet}$ signal and the $pp \to t\bar{t} + \text{jet}$ continuum QCD background as illustrated in Figure 6.8.

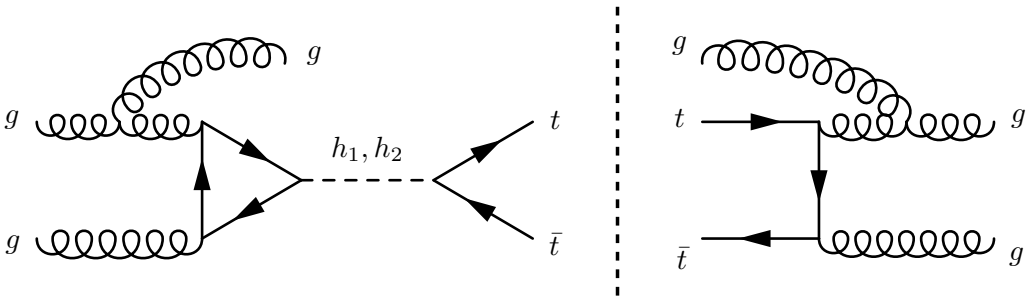

Figure 6.8. The interference between the real corrections to the Higgs signal and the real corrections to the continuum QCD background.

While the Born and virtual interference terms contributes to the gg-channel only, the real emission contributions will include the $q\bar{q}$ and qg/gq-channels as well. The finite real corrections in the gg-channel will include box diagrams similar to Figure 5.1a, which are not IR divergent. The $q\bar{q}$-channel will be finite with no dipole contribution.

6.4 `gghtt`, a NLO Monte Carlo Event Generator

No known available tool is able to compute the interference between tree-level and loop-induced processes. Therefore, for the purposes of this study, `gghtt`, a new parton-level Monte Carlo event generator, has been developed, which is able to handle

interference terms at NLO for loop-induced processes such as Higgs production. This section will describe the different parts making up the event generator. A technical manual can be found in Appendix A.

The code for `gghtt` is available at ref. [122].

6.4.1 Phase Space Generation with KALEU

Parton-level phase space generation is handled by an interface to KALEU [175], a Fortran code that provides importance sampled random phase space points for $2 \to n$ processes, along with their respective weights. KALEU uses the method of the recursive phase space generator from ref. [68].

KALEU is first supplied with all masses and decay widths of the particles for the relevant model. KALEU then decomposes the n-body phase space in a sequence of 2-body phase spaces as in Eq. (4.9). The total weight for each event is then fed back into KALEU for further on-the-fly optimisation of the recursive decomposition.

The Born m-kinematics and the real $m+1$-kinematics are both generated with KALEU separately, as KALEU allows for separate instances to run simultaneously. Generating them in a correlated way would only result in marginal improvements in run-time, as the bottlenecks are the explicit loop calculations in OPENLOOPS and the dipole subtraction as discussed later. This was made evident after time profiling the generation of each event, where the phase space generation happened in the order of 10^{-5} s, whereas the virtual amplitudes where evaluated in 10^{-3} s.

The convergence of the Monte Carlo integration using KALEU for a test example is shown in Figure 6.9 as a function of generated events. Fine-tuning the provided model or the optimisation parameters in KALEU for each process may provide an improvement.

6.4.2 Dipole Subtraction with HELAC-DIPOLES

The code for the dipole subtraction and the integrated counterterms at NLO in `gghtt` has been adapted from HELAC-DIPOLES [176].

The HELAC-DIPOLES code implements the massless dipole subtraction formalism by Catani–Seymour [55] and its massive version by Catani, Dittmaier, Seymour, and Trócsányi [56]. The subtraction scheme has been briefly described in section 3.7, but has been further extended to arbitrary helicity eigenstates of the external partons, as explained in ref. [176].

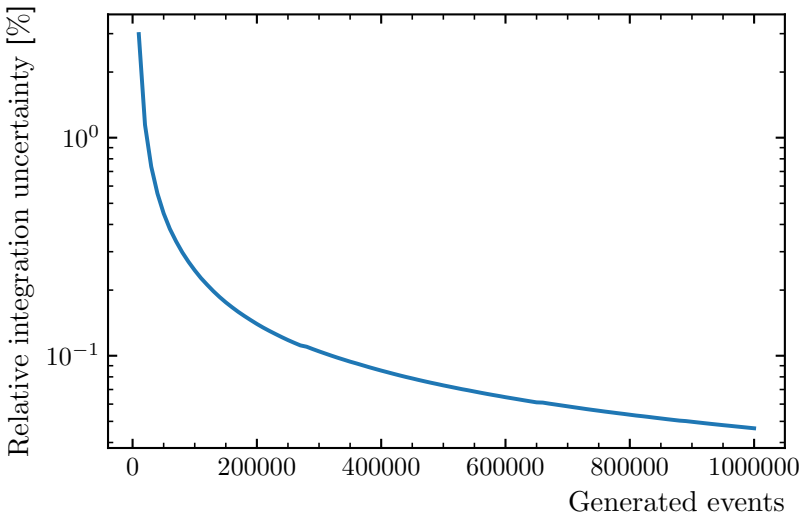

Figure 6.9. The relative uncertainty of the Monte Carlo integration as a function of generated events for a test run of $pp \to t\bar{t} + X$ at NLO QCD.

The subtracted real radiation contribution takes the schematic form

$$\int \mathrm{d}\Phi \sum \left(|\mathcal{M}_{m+1}|^2 - \mathcal{D} \right) , \tag{6.12}$$

where the sum is over colour and spin, along with implicit averages over initial-state colour and spins, and a symmetry factor. All the polarisations, but those of the emitter pair, must be taken over from the real matrix element $\mathcal{M}_{m+1}$.

The implementation currently performs a sum over all helicity configurations, but a future version can allow for a flat Monte Carlo sampling over helicity configurations which may speed up the event generation. Not all helicity configurations contribute equally to the amplitudes, hence further optimisation can be achieved with importance sampling by attributing weights corresponding to each helicity amplitude.

In general, the schematic form of the dipole contributions in Eq. (3.36) is

$$\mathcal{D} \sim \langle \mathcal{M}_0 | \frac{\mathbf{T}_k \cdot \mathbf{T}_{ij}}{\mathbf{T}_{ij}^2} \mathbf{V}_{ij,k} | \mathcal{M}_0 \rangle \, , \tag{6.13}$$

for an emitter ij and spectator k, with the Casimir operator $\mathbf{T}_{ij}^2 = 3$ for a gluon emitter, and $\mathbf{T}_{ij}^2 = 4/3$ for a quark emitter. Here, $\mathcal{M}_0$ refers to the Born matrix element. As the polarisation sum is separate for the ij emitter, $\mathcal{M}_0$ is required to be in the form of helicity amplitudes. The exact forms of $\mathcal{D}$ and in turn $\mathbf{V}_{ij,k}$ depends on whether the emitter and spectator are in the initial or final-state respectively.

Emission of soft-collinear radiation from external gluons will, aside from colour correlations, also generate spin-correlation effects. Hence, in the case of gluon emitters, the dipole contributions acquire terms with $\langle\lambda'|\mathbf{V}_{ij,k}|\lambda\rangle$ for helicity states λ' and λ.

6.4.3 OpenLoops Interface

All Born and virtual amplitudes are provided by an interface to OpenLoops 2 [45], based on the open loops algorithm [42–44], and in turn interfaced to Collier [177], `CutTools` [37], and OneLOop [178].

A simple implementation of the 1HSM have been added to OpenLoops, taking the light and heavy Higgs masses, widths, and the mixing angle as arguments using the `mass(25)`, `hsm_hs_mass`, `width(25)`, `hsm_hs_width`, and `hsm_alpha` parameters respectively. A fifth parameter, `hsm_hs_select`, allow selecting h_1 or h_2 contributions separately. The 1HSM model implementation in OpenLoops can be invoked by setting the `model` parameter string to `hsm`.

The OpenLoops source code has been further modified to allow for the insertion of form factors in the vertices. The one- and two-loop form factors for gluon-fusion Higgs production has been implemented as described in subsection 6.4.4. Both the Born and virtual amplitudes for $gg \to H$ can be evaluated with the `evaluate_tree` subroutine, when setting the `model` parameter in OpenLoops to `ff` rather than the default `sm_yuksel`. If amplitudes in the 1HSM with the form factors are desired, the `model` parameter needs to be set to `hsmff`. The loop order of the form factor can be set with the parameter `ff_loop_order`.

The loop-induced real corrections to $pp \to H + X$ can be generated as usual with the `evaluate_loop2` subroutine. Note that the real corrections have not been generated with the form factors as they would not include the finite contributions from the box diagrams. The box contributions are not IR divergent but they contribute to the finite result.

The virtual final-state corrections to $gg \to H \to t\bar{t}$, using the one-loop form factor and with loop corrections to the $Ht\bar{t}$ vertex, can be generated with `evaluate_loop` using the `ff` or `hsmff` model.

While the absolute-squared Higgs signal amplitudes are selected by setting the `approx` parameter to `FF` or `Higgs1L-squared`, the Higgs–QCD interference can be selected with either `FF2`, `FF-QCD0L`, `FF-QCD1L`, `FF1LFS-QCD0L`, `Higgs1L-QCD0L`, depending on the desired contribution.

The new form factor interface in OpenLoops is useful for considering loop-induced processes at NLO, and can easily be extended to allow for e.g. Higgs pair production $gg \to HH$.

OpenLoops also provides colour and spin-correlated Born amplitudes necessary for the dipole contributions.

The `evaluate_ccmatrix` subroutine in OpenLoops provides a matrix of colour correlated squared tree amplitudes, $\langle \mathcal{M}_0 | \mathbf{T}_i \cdot \mathbf{T}_j | \mathcal{M}_0 \rangle$, for exchanges of soft gluons between two external legs i and j. This is necessary for the integrated counterterms due to the $\mathbf{I}$, $\mathbf{K}$, and $\mathbf{P}$ insertion operators in subsection 3.7.2. OpenLoops can also provide the $\mathbf{I}$ operator with the `evaluate_iop` subroutine, but this is significantly slower than the implementation from Helac-Dipoles as it evaluates the virtual amplitudes as well.

The `evaluate_sc` subroutine in OpenLoops provides the spin-colour correlators on the form

$$\langle \mathcal{M}_0 | \mathbf{T}_{ij} \cdot \mathbf{T}_k | p, ij \rangle \langle p, ij | \mathcal{M}_0 \rangle \,, \tag{6.14}$$

with four-momenta p for the corresponding splitting of emitter ij and spectator k. The exact mapping of p depends on the type of dipole contribution.

An additional custom interface function, `evaluate_cchel`, was added to the OpenLoops source code, providing the colour-correlated squared tree-level helicity amplitudes for each helicity configuration, along with the corresponding helicity configurations.

6.4.4 Form Factors for Gluon-Fusion Higgs Production

The one- and two-loop form factors for $gg \to H$ production [108, 168] have been implemented in OpenLoops with finite top and bottom mass corrections. Some of the contributing diagrams are shown in Figure 6.10. Exact mass dependence of the form factors are especially important for a BSM model with a light Higgs mass, $M_{h_1} < m_t$, and a heavy Higgs mass, $M_{h_2} > m_t$, such as the one studied here. The code for the form factors was adapted partly from JetVHeto [107] and partly from the `gg_H_quark-mass-effects` process [179] in `POWHEG BOX V2` [80–82].

The form factors for the coupling of a Higgs doublet to two gluons, can be decomposed into one- and two-loop parts,

$$F = F_1 + \frac{\alpha_s}{\pi} F_2 + \mathcal{O}(\alpha_s^2) \,. \tag{6.15}$$

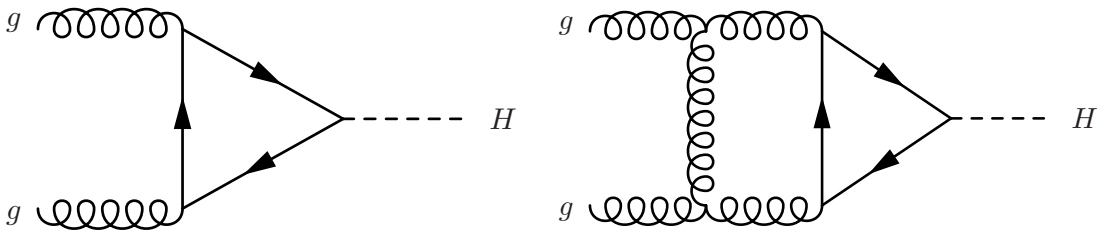

(a) One-loop contribution. **(b)** Two-loop contribution.

Figure 6.10. Some of the diagrams for $gg \to H$ production at NLO.

The form factors will depend on the variables τ_q and x_q defined as

$$\tau_q \equiv \frac{m_H^2}{4m_q^2}\,, \tag{6.16}$$

and

$$x_q \equiv \frac{\sqrt{1-\tau_q^{-1}}-1}{\sqrt{1-\tau_q^{-1}}+1}\,, \tag{6.17}$$

where $q = b, t$ refers to to the quark flavours in the loop, with quark mass m_q either in the on-shell renormalisation scheme, m_q^{OS}, or the $\overline{\text{MS}}$ renormalisation scheme, $m_q(\mu)$, for the scale μ. The on-shell scheme has been used in this study.

The one-loop form factor is [168]

$$F_1 = \sum_q \frac{3}{2\tau_q^2}\left[\tau_q + (\tau_q - 1)f(\tau_q)\right]\,, \tag{6.18}$$

with

$$f(\tau_q) = \begin{cases} \arcsin^2\left(\sqrt{\tau_q}\right), & \tau_q \leq 1 \\ -\frac{1}{4}\left[\ln\dfrac{1+\sqrt{1-\tau_q^{-1}}}{1-\sqrt{1-\tau_q^{-1}}} - i\pi\right]^2, & \tau_q > 1\,. \end{cases} \tag{6.19}$$

The purely virtual two-loop form factor is

$$F_2 = \frac{1}{2}F_1\left[\text{Re}\,(\mathcal{H}) + \frac{C_A}{2}\pi^2 - \frac{C_A}{2}\ln^2\left(\frac{m_H^2}{\mu_R^2}\right)\right]\,, \tag{6.20}$$

corresponding to the virtual part in ref. [180].

The $\mathcal{H}$ term is given by [181]

$$\mathcal{H} = \frac{1}{F_1}\sum_q \Big[T_R C_F\Big(\mathcal{F}_a(x_q) + B\mathcal{F}_b(x_q)\Big) + T_R C_A \mathcal{F}_c(x_q)\Big] + \text{h.c.}\,. \tag{6.21}$$

For the on-shell renormalisation scheme $B = C_F$, while for the $\overline{\text{MS}}$ scheme $B = \ln\left(m_q^2/\mu^2\right)$ for the scale μ. The QCD factors are $T_R = 1/2$, $C_A = 3$, and $C_F = 4/3$. The functions $\mathcal{F}_a$, $\mathcal{F}_b$, and $\mathcal{F}_c$ can be written in terms of harmonic polylogarithms, and are available from refs. [168] and [181],

$$\begin{aligned}\mathcal{F}_a(x) = {} & \frac{36x}{(x-1)^2} - \frac{4x(1-14x+x^2)}{(x-1)^4}\zeta_3 - \frac{4x(1+x)}{(x-1)^3}H(0,x) \\ & - \frac{8x(1+9x+x^2)}{(x-1)^4}H(0,0,x) + \frac{2x(3+25x-7x^2+3x^3)}{(x-1)^5}H(0,0,0,x) \\ & + \frac{4x(1+2x+x^2)}{(x-1)^4}\Big[\zeta_2 H(0,x) + 4H(0,-1,0,x) - H(0,1,0,x)\Big] \\ & + \frac{4x(5-6x+5x^2)}{(x-1)^4}H(1,0,0,x) - \frac{8x(1+x+x^2+x^3)}{(x-1)^5}\left[\frac{9}{10}\zeta_2^2\right. \\ & + 2\zeta_3 H(0,x) + \zeta_2 H(0,0,x) + \frac{1}{4}H(0,0,0,0,x) + \frac{7}{2}H(0,1,0,0,x) \\ & \left. -2H(0,-1,0,0,x) + 4H(0,0,-1,0,x) - H(0,0,1,0,x)\right]\,, \end{aligned} \tag{6.22}$$

and

$$\mathcal{F}_b(x) = -\frac{12x}{(x-1)^2} - \frac{6x(1+x)}{(x-1)^3}H(0,x) + \frac{6x(1+6x+x^2)}{(x-1)^4}H(0,0,x)\,, \tag{6.23}$$

and finally

$$\begin{aligned}\mathcal{F}_c(x) = {} & \frac{4x}{(x-1)^2}\left[3 + \frac{x(1+8x+3x^2)}{(x-1)^3}H(0,0,0,x) - \frac{2(1+x)^2}{(x-1)^2}\left(\frac{4}{5}\zeta_2^2 + 2\zeta_3\right.\right. \\ & + \frac{3\zeta_3}{2}H(0,x) + 3\zeta_3 H(1,x) + \zeta_2 H(1,0,x) + \frac{1}{4}(1+2\zeta_2)H(0,0,x) \\ & - 2H(1,0,0,x) + H(0,0,-1,0,x) + \frac{1}{4}H(0,0,0,0,x) + 2H(1,0,-1,0,x) \\ & \left.\left. -H(1,0,0,0,x)) + \zeta_3 - H(1,0,0,x)\right]\,, \end{aligned} \tag{6.24}$$

where the ζ's refers to the values of the Riemann zeta function. The harmonic polylogarithms $H(\vec{w},x)$ are provided by Chaplin [114].

In the heavy top mass limit, $m_q \to \infty$, the form factors reduce to

$$F_1 \to 1 \qquad \text{and} \qquad \mathcal{H} \to \frac{11}{2}\,. \tag{6.25}$$

The form factors F_1 and $\mathcal{H}$ have been plotted as a function of τ_q in Figure 6.11 and 6.12. Note the limits for $\tau_q \to 0$ and the peaks around $\tau_q = 1$. Note that in the form factors, m_H may refer to an off-shell Higgs mass. For s-channel diagrams, the substitution $m_H^2 \to \hat{s}$ applies.

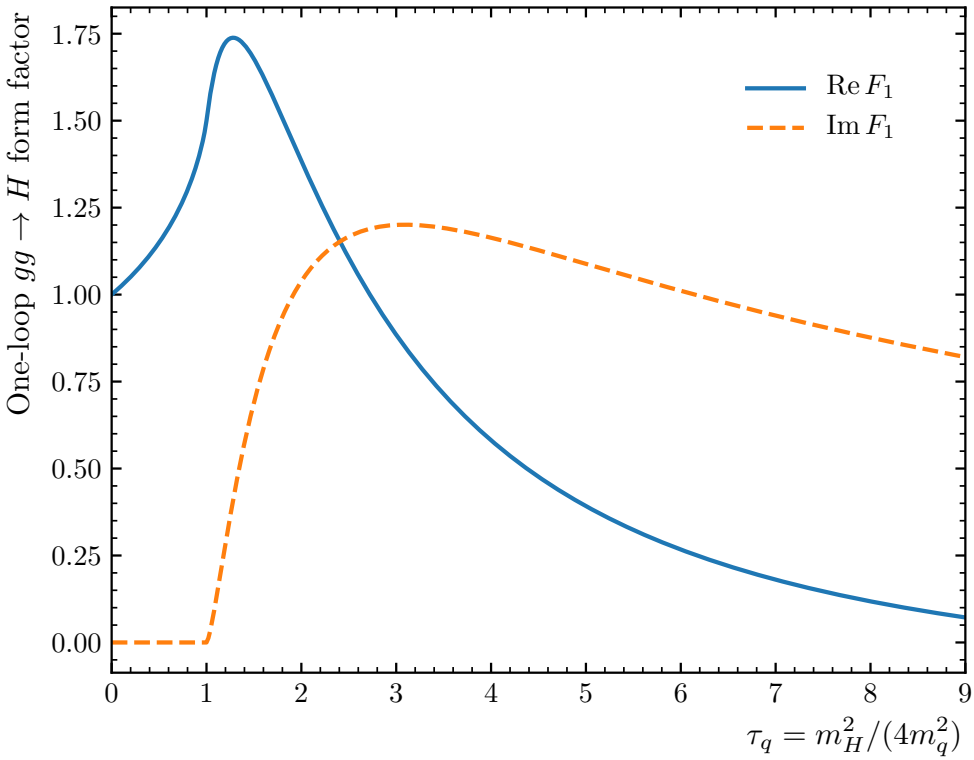

Figure 6.11. The one-loop form factor for $gg \to H$ production as a function of τ_q.

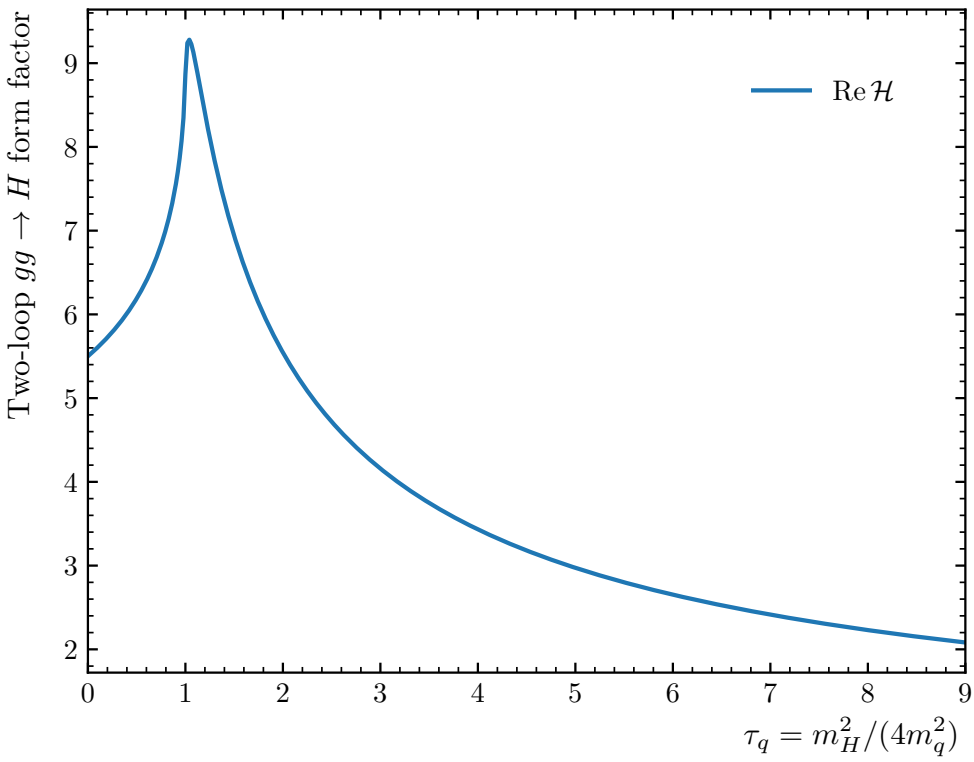

Figure 6.12. The $\mathcal{H}$ term of the two-loop form factor for $gg \to H$ production as a function of τ_q.

6.5 Calculational Details

This section will go over the technical details of the calculations performed.

The recommendations for input parameters from the LHC Higgs Working Group (LHCHWG)[3] [182] have been employed. For the EW parameter input, the G_μ scheme has been used,

$$\alpha = \frac{\sqrt{2}}{\pi} G_F m_W^2 \sin^2\theta_W \,, \quad \text{and} \quad \sin^2\theta_W = 1 - \frac{m_W^2}{m_Z^2} \,, \tag{6.26}$$

with

$$\begin{aligned} G_F &= 1.1663787 \times 10^{-5}\ \text{GeV}^{-2} \,, & m_t &= 173.2\ \text{GeV} \,, \\ m_W &= 80.35797\ \text{GeV} \,, & m_b &= 4.92\ \text{GeV} \,, \\ m_Z &= 91.15348\ \text{GeV} \,, & \Gamma_t &= 1.369\ \text{GeV} \,, \end{aligned} \tag{6.27}$$

resulting in

$$1/\alpha \approx 132.36 \quad \text{and} \quad \sin^2\theta_W \approx 0.222838 \,. \tag{6.28}$$

The PDF set `PDF4LHC15_nlo_mc` [183], with default α_s, provided by LHAPDF [66] has been used. The factorisation and renormalisation scales have been set to

$$\mu = \mu_R = \mu_F = \frac{M_{t\bar{t}}}{2} \,. \tag{6.29}$$

The hadronic pp collision energy is $\sqrt{s} = 13$ TeV, corresponding to current LHC energy. Finite top and bottom quark mass effects for quark loops have been taken into account.

6.5.1 Higgs Decay Widths

The SM Higgs decay widths have been calculated using `HDECAY` [69, 70] and Prophecy4f [71–73]. For a SM Higgs with $m_H = 125$ GeV, the decay width is $\Gamma_H = 4.087 \times 10^{-3}$ GeV. The decay widths of the light and heavy Higgs bosons in

[3] Originally called the LHC Higgs Cross Section Working Group (LHCHXSWG).

the 1HSM have been calculated using

$$\Gamma_{h_1} = \Gamma_H\left(M_{h_1}\right)\cos^2\theta\,, \tag{6.30}$$

$$\Gamma_{h_2} = \Gamma_H\left(M_{h_2}\right)\sin^2\theta + \Gamma\left(h_2 \to n \times h_1\right)\,, \tag{6.31}$$

where $\Gamma_H(M)$ refers to the decay width of a SM Higgs with mass M. Due to numerical issues in `HDECAY` from tiny values of m_b for decay modes with b quarks, it is not possible to calculate the full contribution to $\Gamma_H(M = 3\text{ TeV})$. Therefore, for $M = 3$ TeV, the approximation of only taking heavy gauge boson decay modes into account, $\Gamma_H \approx \Gamma(H \to WW) + \Gamma(H \to ZZ)$, has been used. The partial decay widths for $\Gamma\left(h_2 \to n \times h_1\right)$ has been taken into account for $2 \leq n \leq 4$. A custom implementation of the 1HSM in FeynRules [115, 184] was used to produce a UFO [185] implementation that was subsequently used in MadGraph5_aMC@NLO [47] to calculate the partial decay widths $\Gamma\left(h_2 \to n \times h_1\right)$, the results of which are shown in Table 6.2. It is clear that partial decay widths for decays to higher multiplicities, $n > 4$, of h_1 are suppressed.

	$\theta = \theta_1$		
M_{h_2} [GeV]	$\Gamma\left(h_2 \to 2 \times h_1\right)$ [GeV]	$\Gamma\left(h_2 \to 3 \times h_1\right)$ [GeV]	$\Gamma\left(h_2 \to 4 \times h_1\right)$ [GeV]
700	2.1556(1)	0.00468(2)	$6.24(4) \times 10^{-7}$
1000	6.0953(1)	0.1692(7)	0.001718(9)
1500	9.8911(1)	0.218(2)	0.001632(8)
3000	20.658(1)	0.306(2)	0.001060(7)

	$\theta = \theta_2$		
M_{h_2} [GeV]	$\Gamma\left(h_2 \to 2 \times h_1\right)$ [GeV]	$\Gamma\left(h_2 \to 3 \times h_1\right)$ [GeV]	$\Gamma\left(h_2 \to 4 \times h_1\right)$ [GeV]
700	4.1798(1)	0.507(2)	0.01451(8)
1000	11.604(1)	7.34(4)	2.46(2)
1500	27.26(1)	12.9(2)	3.91(2)
3000	66.8(1)	21.4(2)	4.17(2)

Table 6.2. Partial decay widths for $h_2 \to n \times h_1$ for $n = 2, 3$, and 4 in the 1HSM for the eight different benchmark points.

The final decay widths Γ_{h_1} and Γ_{h_1} along with their respective Γ/M ratios in the 1HSM for all benchmark points are shown in Table 6.3.

	M_{h_2} [GeV]	700	1000	1500	3000
θ_1	Γ_{h_1} [GeV]	$3.910(5) \times 10^{-3}$	$3.910(5) \times 10^{-3}$	$4.004(5) \times 10^{-3}$	$4.067(5) \times 10^{-3}$
	Γ_{h_1}/M_{h_1}	$3.1283(4) \times 10^{-5}$	$3.1283(4) \times 10^{-5}$	$3.2034(4) \times 10^{-5}$	$3.2537(4) \times 10^{-5}$
	Γ_{h_2} [GeV]	10.780(3)	34.295(3)	79.52(2)	86.70(3)
	Γ_{h_2}/M_{h_2}	0.015400(4)	0.034295(3)	0.053013(7)	0.028902(9)
θ_2	Γ_{h_1} [GeV]	$3.488(5) \times 10^{-3}$	$3.488(5) \times 10^{-3}$	$3.813(5) \times 10^{-3}$	$4.017(5) \times 10^{-3}$
	Γ_{h_1}/M_{h_1}	$2.7908(4) \times 10^{-5}$	$2.7908(4) \times 10^{-5}$	$3.0506(4) \times 10^{-5}$	$3.2139(4) \times 10^{-5}$
	Γ_{h_2} [GeV]	33.903(8)	116.37(4)	273.6(2)	322.5(2)
	Γ_{h_2}/M_{h_2}	0.04843(2)	0.11637(4)	0.18240(8)	0.10751(5)

Table 6.3. Decay widths and Γ/M ratios for the light and heavy Higgs bosons, h_1 and h_2, in the 1HSM extension for the considered benchmark points. The error is due to rounding and the numerical integration.

The partial decay widths for $n > 2$ is due to cascaded emissions of $h_2 \to h_2 h_1$ and decays $h_2 \to h_1 h_1$, as shown in Figure 6.13.

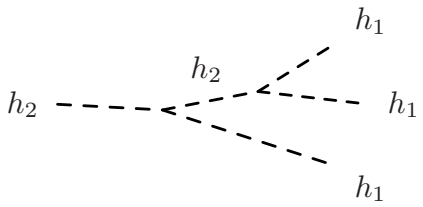

Figure 6.13. The cascaded partial decay of $h_2 \to 3 \times h_1$.

This implies a circular dependence of the decay width Γ_{h_2} when using the Breit–Wigner approximation to the propagator, as can be seen in Eq. (3.19). This is not problematic if $\Gamma_{h_2}/M_{h_2} \ll 1$, but as can be seen in Table 6.3 one of the benchmark points reaches $\Gamma_{h_2}/M_{h_2} \sim 0.18$. A simple solution would be to recursively calculate the decay width. However, in the case of $\Gamma/M \sim 1$ the Breit–Wigner approximation does not hold, and one should use a better estimate of the self energy $\Sigma(p^2)$ in the exact propagator expression of Eq. (2.30). It is important, however, to do this in a gauge-invariant way. This would likely produce a tiny correction in this case, and has therefore not been done in this study. But it may be necessary for certain new physics models that introduces resonances with large decay widths.

6.5.2 Numerical Stability

For numerical stability, a small cut on the transverse momentum of the real radiated jet is applied, $p_{T,j} > 0.1$ GeV. This is in particularly necessary for the evaluation of

the loop-induced real emission amplitudes for the gg-channel, $gg \to Hg$, which can suffer from numerical instability in the box diagrams. This p_T cutoff is expected to remove less than 0.1% of the total cross-section. Additional stability treatment is included in `gghtt`, which discards events based on the relative accuracy estimate provided by OpenLoops, which will be above some threshold for events causing numerical instability in the loop calculations. A cut on the relative ratio of the invariant mass of the emitter, $s_{ij}/s_{ijk} < 10^{-6}$, has been applied. Furthermore, events that are in the soft and collinear region, i.e. low p_T or low s_{ij}/s_{ijk} have been flagged for a further stability check of the relative error of the real-subtracted cross-section.

6.6 Validation

The dipole subtraction implemented in `gghtt` has been validated by considering the ratio between the real emission $\mathrm{d}\sigma_R$, and the sum over the dipole terms $\mathrm{d}\sigma_A$, as a function of jet p_T for each process and contribution. An example for the SM QCD process $pp \to t\bar{t} + \text{jet}$ is shown in Figure 6.14. The dipoles were plotted with the same $m+1$-kinematics as for the real emission, instead of their actual m-kinematics. As seen on Figure 6.14, the ratio goes to one for p_T going to zero, indicating complete subtraction of the divergent parts of the real emission at $p_T \to 0$.

The cancellation of the single and double poles, $1/\varepsilon$ and $1/\varepsilon^2$, from the virtual one-loop corrections against those from the integrated counterterms, has been checked for a selection of phase space points in the case of the continuum QCD background. Internal machinery in `gghtt` facilitates such checks. However, the $gg \to H$ form factors does not provide the IR divergent parts, but only the finite result, and hence these need to be checked at the level of the total cross-section.

The implementation of the one- and two-loop form factors for gluon-fusion Higgs production in OpenLoops has been validated by considering the process $pp \to H + X$ at NLO in `gghtt` and comparing the total cross-section to the result from SusHi [105, 106]. The total cross-section results for $pp \to H + X$ in the SM, from `gghtt` with parameter input as in section 6.5 but $\mu_R = \mu_F = m_H/2$, are

$$\begin{aligned} \sigma_{\mathrm{LO}}(pp \to H + X) &= 14.541(7)\ \mathrm{pb}\,, \\ \sigma_{\mathrm{NLO}}(pp \to H + X) &= 35.11(2)\ \mathrm{pb}\,, \end{aligned} \tag{6.32}$$

of which the finite real contribution only accounts for 0.077(2) pb. Note here that σ_{NLO} refers to the sum of the LO cross-section and corresponding NLO correction.

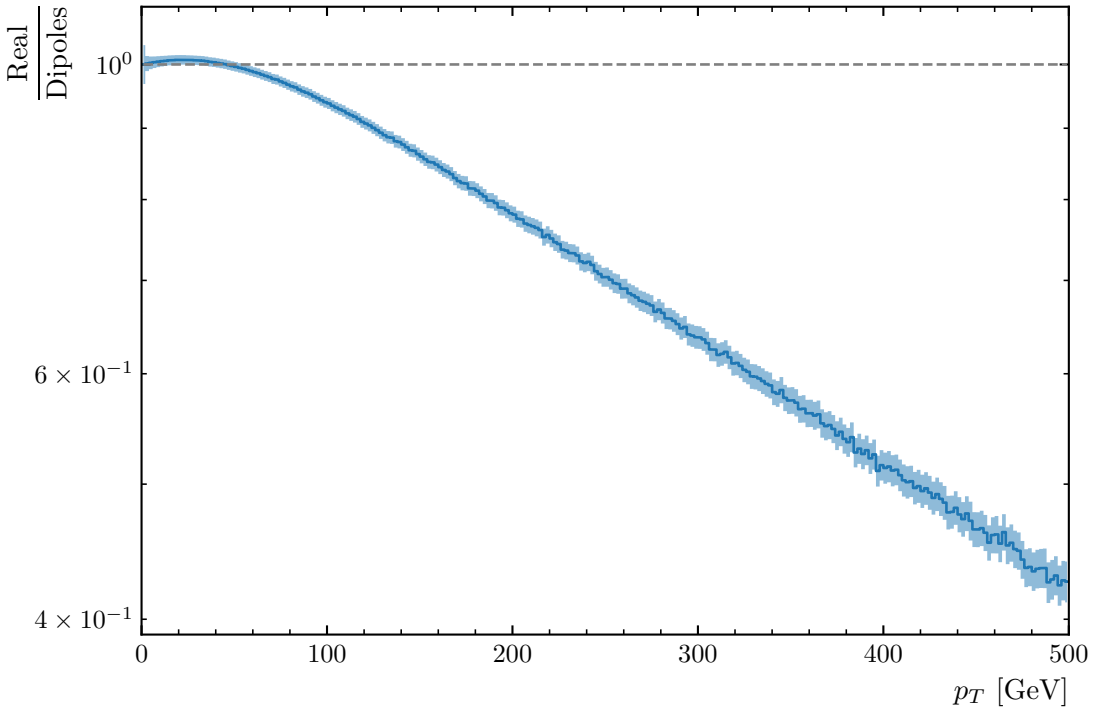

Figure 6.14. The ratio between the real emission and the sum over the dipole terms, Real/Dipoles $\sim \mathrm{d}\sigma^R / \mathrm{d}\sigma^A$, as a function of jet p_T for the SM QCD process $pp \to t\bar{t} + \text{jet}$. The dipoles have been plotted with the same $m+1$-kinematics as for the real emission, instead of their actual m-kinematics. The bands show the MC integration error.

As explained in section 3.5, the NLO coefficient is larger than the LO cross-section, and the real emission contribution is nearly negligible. The $pp \to H + X$ NLO cross-section has been validated against SusHi for varying Higgs mass m_H and scales, μ_R and μ_F, to ensure correct behaviour of the form factors. All cross-sections were found to be in agreement with SusHi within their respective Monte Carlo error estimates. The p_T distribution for $pp \to H + X$ from `gghtt` has been validated against H1jet.

The LO and one-loop amplitudes implemented in OpenLoops have been compared at the amplitude level for several phase space points to the implementation used in ref. [121], and was found to be in agreement. The implementation of the continuum QCD background for $pp \to t\bar{t} + X$ at NLO in `gghtt` has been validated against the result from MCFM [76–79], and was found to be in agreement. The implementation of the **I** operator from Helac-Dipoles was validated against the implementation in OpenLoops for the continuum QCD background.

6.7 Results and Discussion

This section presents the results for the integrated cross-sections and differential distributions for the 1HSM from `gghtt`. Distributions for the SM are available in Appendix B. Note that σ_{NLO} refers to the sum of the LO cross-section and corresponding NLO correction.

All errors listed here represent Monte Carlo statistics only. Besides statistical uncertainties, there are theoretical uncertainties due to the sensitivity to the renormalisation and factorisation scale choice coming from higher-order corrections, and PDF uncertainties. However, these are not included in the main results, but the size of them are estimated in subsection 6.7.4. The MC error is shown using the shorthand bracket notation, where the number in the parentheses is the uncertainty on the last digit of the quoted result.

6.7.1 Integrated Cross-Sections

The integrated NLO cross-sections and associated K-factors for each contribution in the SM are shown for the process $pp\,(\to \{h_1, h_2\}) \to t\bar{t} + X$ in Table 6.4. The contributions are the SM Higgs signal, $|\mathcal{M}_H|^2$, the continuum QCD background, $|\mathcal{M}_{\text{QCD}}|^2$, and their interference, $2\,\text{Re}(\mathcal{M}_H^* \mathcal{M}_{\text{QCD}})$.

The K-factor is defined as

$$K = \frac{\sigma_{\text{NLO}}}{\sigma_{\text{LO}}}\,, \tag{6.33}$$

where σ_{NLO} includes the sum of the LO cross-section and the NLO correction. Since there is some ambiguity in the definition of the K-factor [186], it is worth mentioning that both the LO and NLO cross-sections are evaluated with NLO PDF sets and three-loop α_s running.

$pp\,(\to \{h_1, h_2\}) \to t\bar{t} + X$ in the SM, pp, $\sqrt{s} = 13$ TeV					
Higgs signal		QCD background		Interference	
σ_{NLO} [pb]	K	σ_{NLO} [pb]	K	σ_{NLO} [pb]	K
0.030971(3)	1.6512(2)	675.23(4)	1.5965(1)	−1.5865(2)	2.1807(2)

Table 6.4. Integrated NLO cross-sections and corresponding K-factors for the process $pp\,(\to \{h_1, h_2\}) \to t\bar{t} + X$ in the SM. The MC integration error is shown in brackets.

$pp\,(\to \{h_1, h_2\}) \to t\bar{t} + X$ in the SM, pp, $\sqrt{s} = 13$ TeV					
Higgs signal		QCD background		Interference	
σ_{R} [pb]	$\sigma_{\mathrm{R}}/\sigma_{\mathrm{NLO}}$	σ_{R} [pb]	$\sigma_{\mathrm{R}}/\sigma_{\mathrm{NLO}}$	σ_{R} [pb]	$\sigma_{\mathrm{R}}/\sigma_{\mathrm{NLO}}$
−0.002428(1)	−0.07839(4)	−24.14(2)	−0.03575(2)	0.07117(8)	−0.04486(5)

Table 6.5. Integrated cross-sections for the finite real contribution with the corresponding relative differences to the total NLO cross-section for the process $pp\,(\to \{h_1, h_2\}) \to t\bar{t} + X$ in the SM. The MC integration error is shown in brackets.

The integrated NLO cross-sections and associated K-factors for the Higgs signal and for the Higgs–QCD interference in the 1HSM for each benchmark point are shown in Table 6.6. The integrated cross-sections for the isolated h_2 and h_2–QCD interference are shown in Table 6.7.

Since there can be some ambiguity in the term "signal", as discussed in section 3.4, the terms used for the different contributions will be explained here. Schematically, at LO for the 1HSM,

$$\begin{aligned}
\text{QCD background:} \quad & |\mathcal{M}_{\mathrm{QCD}}|^2 \\
\text{Higgs signal:} \quad & |\mathcal{M}_{h_1}|^2 + |\mathcal{M}_{h_2}|^2 + 2\,\mathrm{Re}\left(\mathcal{M}_{h_1}^* \mathcal{M}_{h_2}\right) , \\
\text{Higgs–QCD interference:} \quad & 2\,\mathrm{Re}\left(\left(\mathcal{M}_{h_1}^* + \mathcal{M}_{h_2}^*\right) \mathcal{M}_{\mathrm{QCD}}\right) , \\
h_2 \text{ signal:} \quad & |\mathcal{M}_{h_2}|^2 , \\
h_2\text{–QCD interference:} \quad & 2\,\mathrm{Re}\left(\mathcal{M}_{h_2}^* \mathcal{M}_{\mathrm{QCD}}\right) ,
\end{aligned} \tag{6.34}$$

i.e. "Higgs signal" refers to the 1HSM contribution from h_1 and h_2 without their interference to the continuum QCD background. Furthermore, the heavy Higgs h_2 contribution and its interference to the continuum QCD background has been isolated in order to study them in detail.

The integrated cross-sections for the Higgs signal in the 1HSM exhibit a relatively small deviation from their SM counterpart. For the benchmark points with $\theta_1 \lesssim 0.2$, the Higgs signal deviation range from 11% to 0.12% for the different heavy Higgs masses, with the largest deviation for $M_{h_1} = 1$ GeV. The deviation of the Higgs–QCD interference range from 6% to 0.9%. For the benchmark points with $\theta_2 \lesssim 0.4$, the deviations of the Higgs signal range from 35% to 4%, while the Higgs–QCD interference range from 18% to 1%.

$pp\,(\to\{h_1,h_2\})\to t\bar{t}+X$ in the 1HSM, pp, $\sqrt{s}=13$ TeV					
		Higgs signal		Higgs–QCD interference	
	M_{h_2} [GeV]	σ_{NLO} [pb]	K	σ_{NLO} [pb]	K
θ_1	700	0.029108(2)	1.6234(2)	−1.5169(2)	2.1743(3)
	1000	0.027334(2)	1.6459(2)	−1.49132(9)	2.1579(2)
	1500	0.029932(3)	1.6745(2)	−1.5601(2)	2.1926(2)
	3000	0.030933(3)	1.6661(2)	−1.5724(1)	2.1719(2)
θ_2	700	0.027231(2)	1.5689(2)	−1.3487(2)	2.1383(3)
	1000	0.020114(2)	1.6442(2)	−1.30744(8)	2.1458(2)
	1500	0.026519(2)	1.6617(2)	−1.4796(2)	2.1903(2)
	3000	0.029772(2)	1.6452(2)	−1.5673(2)	2.1924(2)

Table 6.6. Integrated NLO cross-sections and corresponding K-factors for the process $pp\,(\to\{h_1,h_2\})\to t\bar{t}+X$ in the 1HSM for each benchmark point. "Higgs" refers here to the h_1 and h_2 contributions. The MC integration error is shown in brackets.

$pp\,(\to\{h_1,h_2\})\to t\bar{t}+X$ in the 1HSM, pp, $\sqrt{s}=13$ TeV					
		h_2 signal		h_2–QCD interference	
	M_{h_2} [GeV]	σ_{NLO} [pb]	K	σ_{NLO} [pb]	K
θ_1	700	0.0030825(4)	1.4921(2)	0.00920(7)	−6.08(6)
	1000	0.00022433(2)	1.3670(2)	0.013389(7)	2.645(2)
	1500	$2.7419(2)\times10^{-6}$	1.2663(1)	0.0032540(5)	2.3522(5)
	3000	$2.2091(2)\times10^{-9}$	1.2414(2)	0.00019889(2)	2.2532(2)
θ_2	700	0.0109802(9)	1.4961(2)	0.01604(9)	−1.64(1)
	1000	0.00078146(5)	1.3881(1)	0.03550(2)	3.022(2)
	1500	$1.14923(7)\times10^{-5}$	1.32998(9)	0.008283(2)	2.5617(7)
	3000	$1.9755(2)\times10^{-8}$	1.3556(1)	0.00063208(7)	2.3300(3)

Table 6.7. Integrated NLO cross-sections and corresponding K-factors for the process $pp\,(\to\{h_1,h_2\})\to t\bar{t}+X$ in the 1HSM for each benchmark point. Only h_2 contributions are considered here. The MC integration error is shown in brackets.

$pp\,(\to\{h_1,h_2\})\to t\bar{t}+X$ in the 1HSM, pp, $\sqrt{s}=13$ TeV					
		Higgs signal		Higgs–QCD interference	
	M_{h_2} [GeV]	σ_{R} [pb]	$\sigma_{\mathrm{R}}/\sigma_{\mathrm{NLO}}$	σ_{R} [pb]	$\sigma_{\mathrm{R}}/\sigma_{\mathrm{NLO}}$
θ_1	700	−0.0024074(6)	−0.08271(2)	0.0594(2)	−0.03918(8)
	1000	−0.0022439(5)	−0.08209(2)	0.08056(4)	−0.05402(3)
	1500	−0.001906(2)	−0.06368(6)	0.06097(9)	−0.03908(6)
	3000	−0.002124(2)	−0.06867(5)	0.07714(6)	−0.04906(4)
θ_2	700	−0.0022818(7)	−0.08380(3)	0.0438(2)	−0.03248(9)
	1000	−0.0016467(4)	−0.08187(2)	0.06983(3)	−0.05341(3)
	1500	−0.001932(2)	−0.07286(5)	0.05835(9)	−0.03944(6)
	3000	−0.0024503(5)	−0.08230(2)	0.06150(9)	−0.03924(6)

Table 6.8. Integrated cross-sections for the finite real contribution with the corresponding relative differences to the total NLO cross-section for the process $pp\,(\to\{h_1,h_2\})\to t\bar{t}+X$ in the 1HSM for each benchmark point. The MC integration error is shown in brackets.

The ratio of the Higgs–QCD interference to the Higgs signal range from a factor 51 to 55 for the benchmark points with θ_1, while for the θ_2 benchmark points the range is wider, 49 to 65. The Higgs–QCD interference has the opposite sign to the Higgs signal and accounts for the majority of the total cross-section contribution from the heavy Higgs. In ref. [121], it was noted that the IR divergent bare one-loop interference switched sign compared to the tree-level interference. This is evidently not the case when taking the full NLO contribution into account.

The K-factors for the Higgs signal are around 1.6 for the SM and 1HSM Higgs signals alike, while the K-factors for the Higgs–QCD interference are around 2.2 for the SM and 1HSM. Hence, NLO corrections are in particular important for the interference term, which constitutes the majority of the overall BSM signal. There is little difference in the K-factors when taking into account the heavy Higgs compared to the SM.

In Table 6.7, it can be seen that the h_2 resonance signal decreases rapidly with increasing M_{h_2} as expected, and that the θ_2 results are roughly a factor 4 to 9 times larger than the θ_1 results. The overall BSM signal is much larger when taking the h_2–QCD interference into account, especially for large M_{h_2}. For the θ_1 benchmark points, the ratio of the interference to signal range from 3 to 9×10^4, while for the

θ_2 benchmark points, the range is from 1.5 to 3.2×10^4.

The contribution of the light and heavy Higgs to the overall BSM signal does not exceed 0.15% and can be reasonably neglected especially for larger M_{h_2}. For reference, the integrated cross-section results for the h_1–h_2 interference is available in Appendix C.

Table 6.5 and 6.8 shows the integrated cross-sections for the finite real contribution with the corresponding relative differences to the total NLO cross-section for the SM and 1HSM respectively. These cross-sections will be dependent on the dipole subtraction scheme used, which in this case is Catani–Seymour subtraction. However, they indicate that the result is very inclusive since the real emission and dipole sum contributions are relatively small compared to the virtual contribution and the integrated counterterms. Since these contributions are generally some of the slowest to compute, they can be neglected for this particular process in a study concerned with quick estimates or fast model parameter scans. For more serious precision studies, they should of course be included.

Additional integrated NLO cross-sections for the h_1 resonance signal, the h_1–QCD interference, and the h_1–h_2 interference are given in Appendix C.

6.7.2 Differential Distributions

Additional insight can be gained from considering differential distributions.

The differential distributions in the invariant mass of the $t\bar{t}$ system, $M_{t\bar{t}}$, for each contribution listed in Equation 6.34 and for each 1HSM benchmark point, are shown in Figure 6.15 – 6.22. For reference, the SM distribution in $M_{t\bar{t}}$ is shown in Figure B.1 of Appendix B.

The distributions of the relative deviation of the 1HSM distribution to the SM distribution, 1HSM/SM-1, for the Higgs–QCD interference, are shown in Figure 6.23 and 6.24 for each benchmark point.

Figure 6.25 – 6.32 shows the distributions in $M_{t\bar{t}}$ for the SM background, the 1HSM signal, and the 1HSM total. The SM background is defined as the contributions from the continuum QCD background and the light Higgs h_1 including their interference. The 1HSM signal is defined as the contribution from the heavy Higgs h_2 including its interference to the QCD background and the light Higgs h_1. The 1HSM total is the sum of the SM background and the 1HSM signal. The lower ratio plots in Figure 6.25 – 6.32 shows the relative ratio of the 1HSM total and SM background.

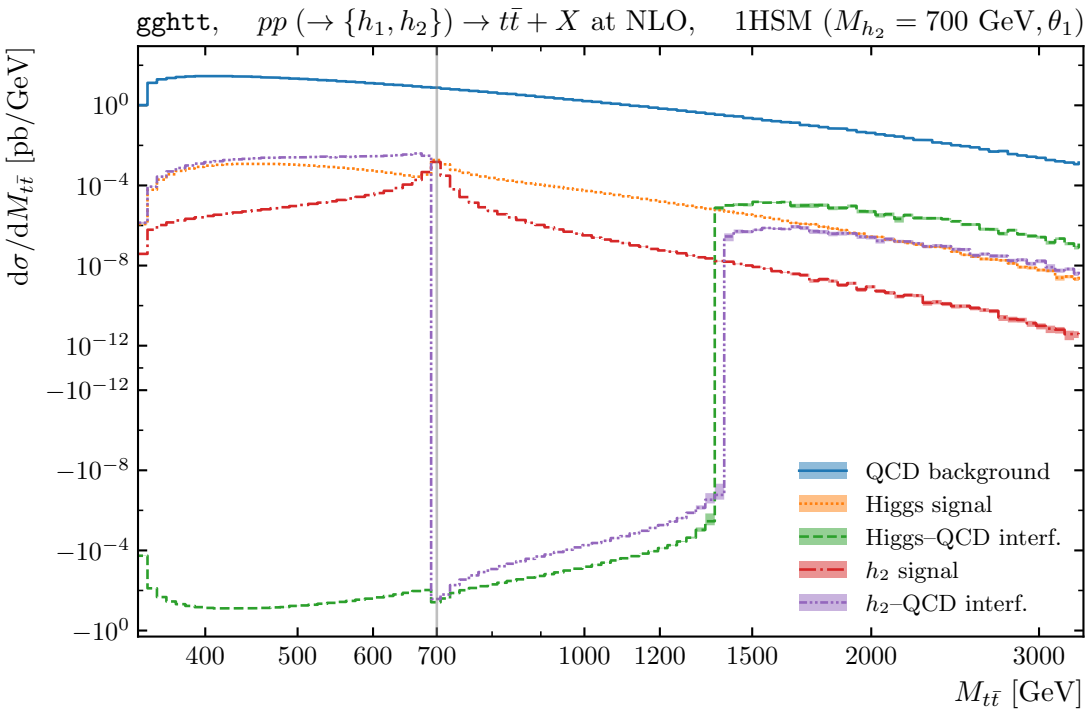

Figure 6.15. Differential distributions in $M_{t\bar{t}}$ for the process $pp\,(\to\{h_1,h_2\})\to t\bar{t}+X$ at NLO in the 1HSM extension for $M_{h_2}=700$ GeV, $\theta=\theta_1=\pi/15$.

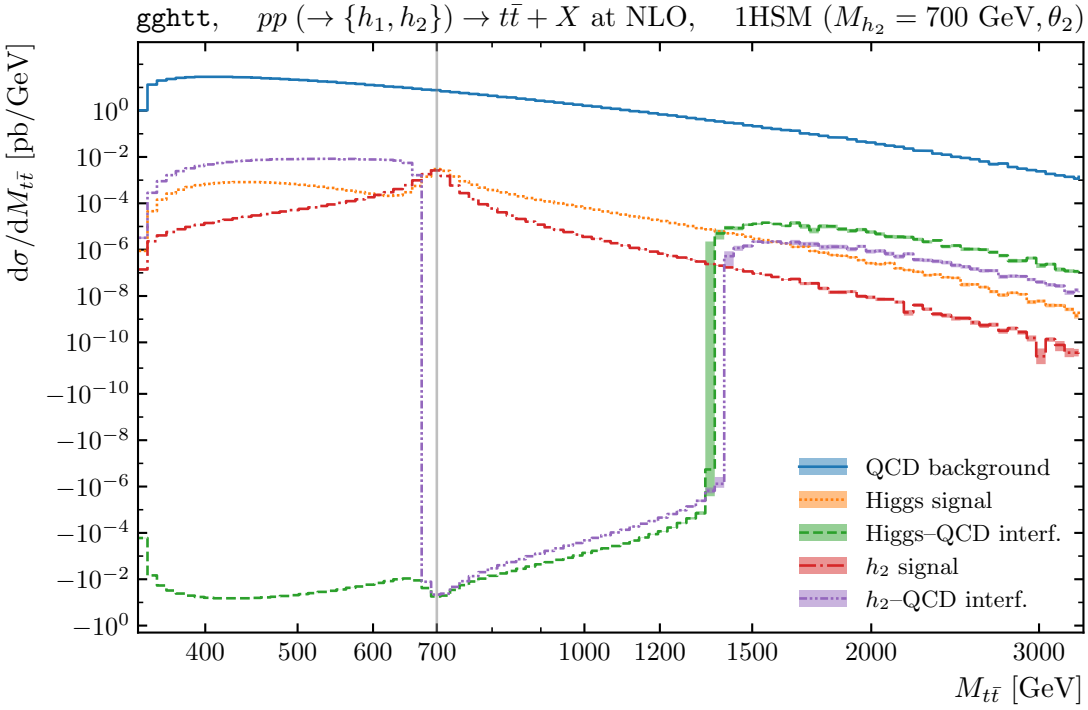

Figure 6.16. Differential distributions in $M_{t\bar{t}}$ for the process $pp\,(\to\{h_1,h_2\})\to t\bar{t}+X$ at NLO in the 1HSM extension for $M_{h_2}=700$ GeV, $\theta=\theta_2=\pi/8$.

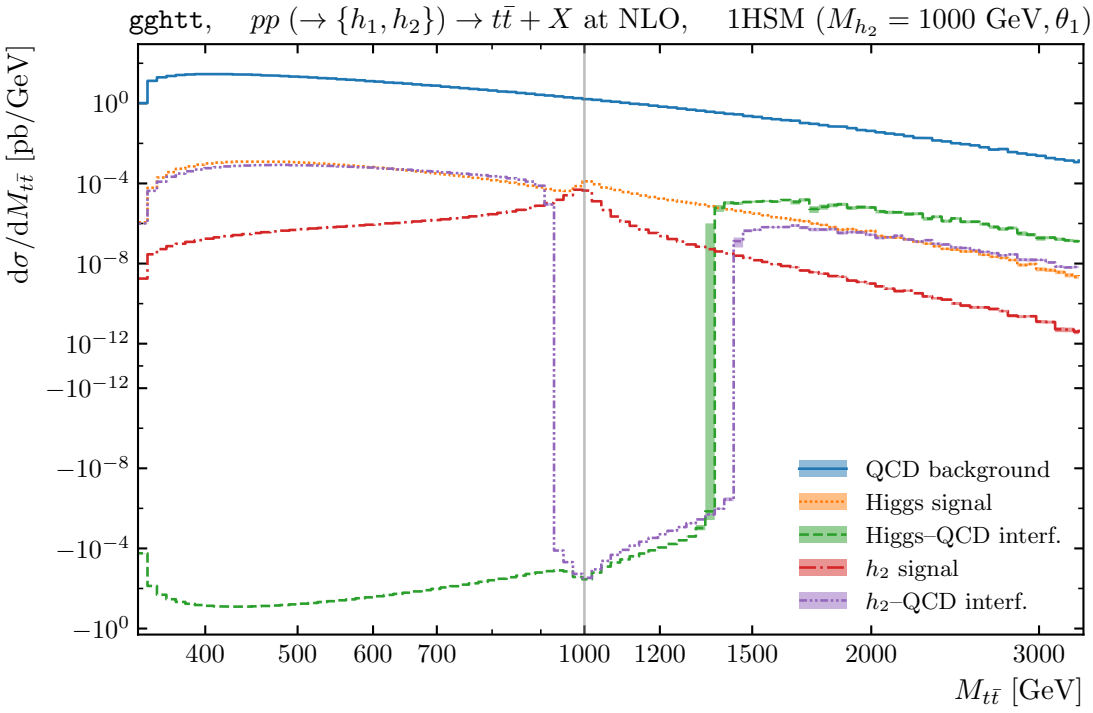

Figure 6.17. Differential distributions in $M_{t\bar{t}}$ for the process $pp\,(\to\{h_1,h_2\})\to t\bar{t}+X$ at NLO in the 1HSM extension for $M_{h_2}=1$ TeV, $\theta=\theta_1=\pi/15$.

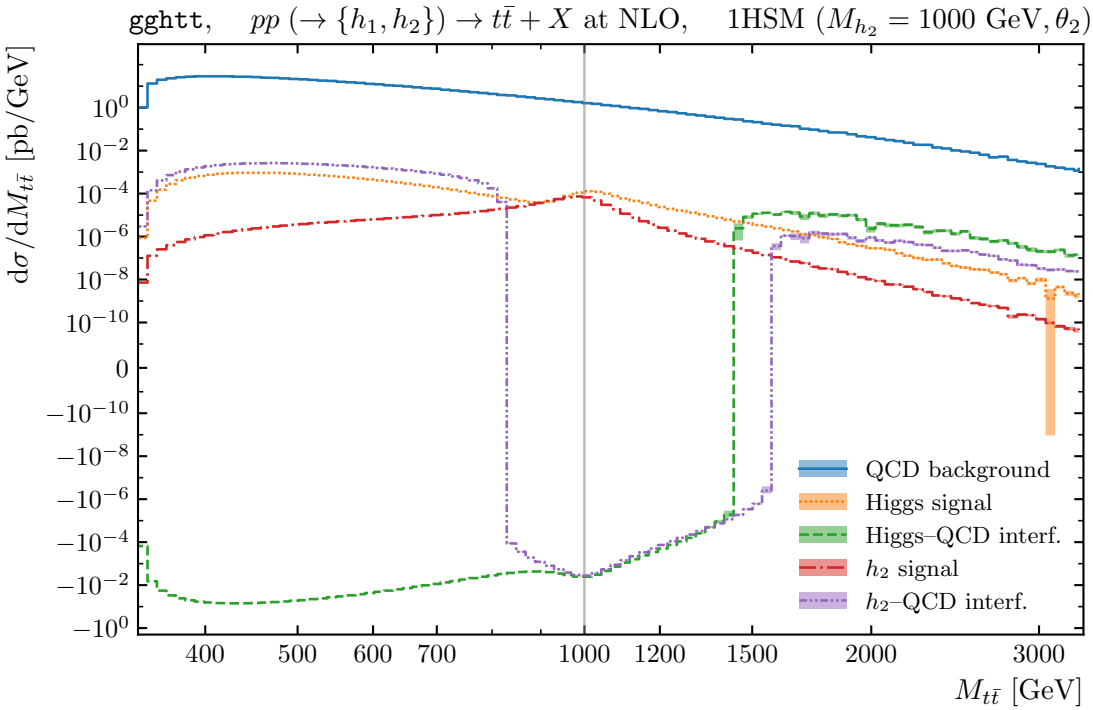

Figure 6.18. Differential distributions in $M_{t\bar{t}}$ for the process $pp\,(\to\{h_1,h_2\})\to t\bar{t}+X$ at NLO in the 1HSM extension for $M_{h_2}=1$ TeV, $\theta=\theta_2=\pi/8$.

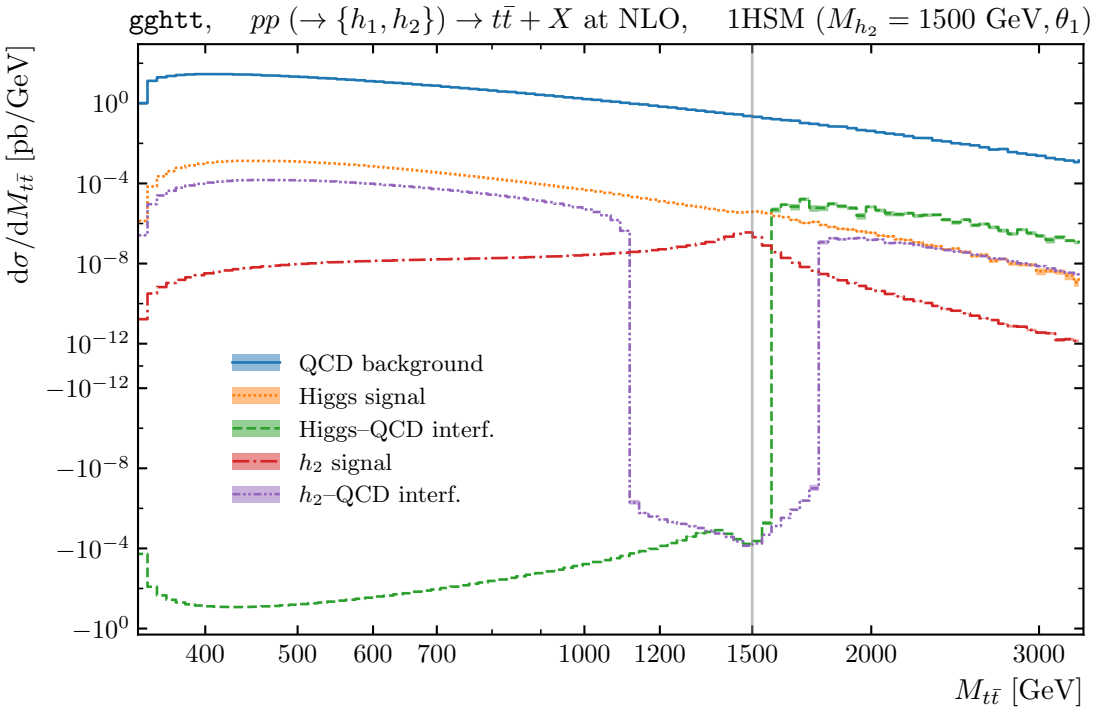

Figure 6.19. Differential distributions in $M_{t\bar{t}}$ for the process $pp\,(\to\{h_1,h_2\})\to t\bar{t}+X$ at NLO in the 1HSM extension for $M_{h_2}=1.5$ GeV, $\theta=\theta_1=\pi/22$.

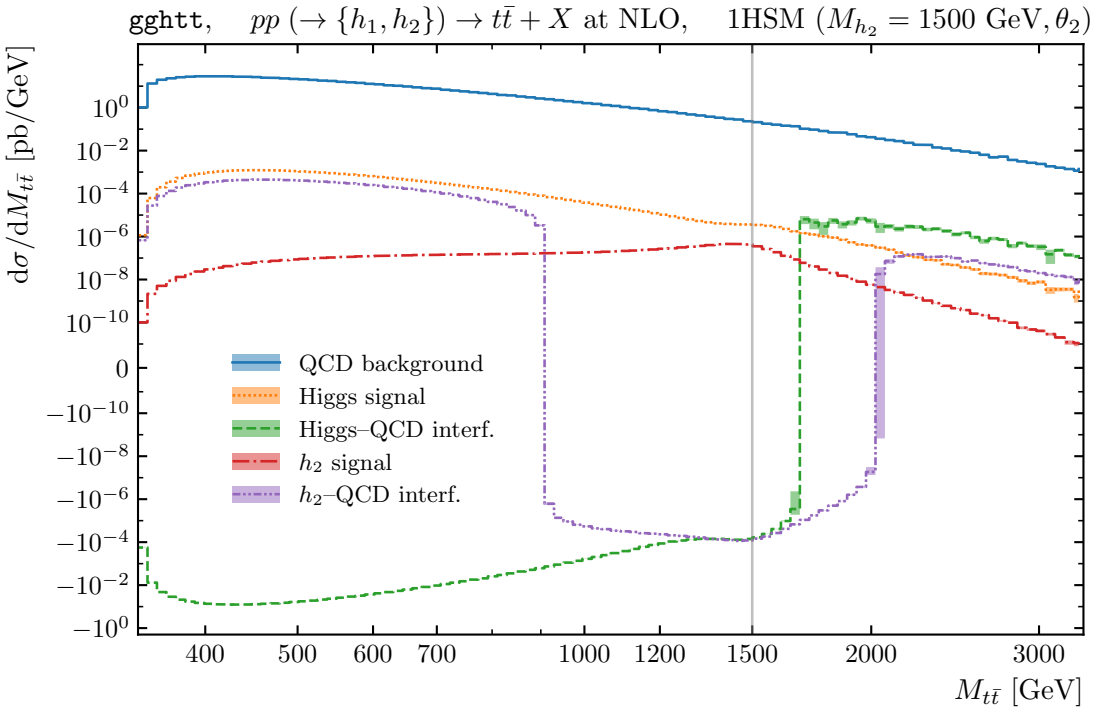

Figure 6.20. Differential distributions in $M_{t\bar{t}}$ for the process $pp\,(\to\{h_1,h_2\})\to t\bar{t}+X$ at NLO in the 1HSM extension for $M_{h_2}=1.5$ TeV, $\theta=\theta_2=\pi/12$.

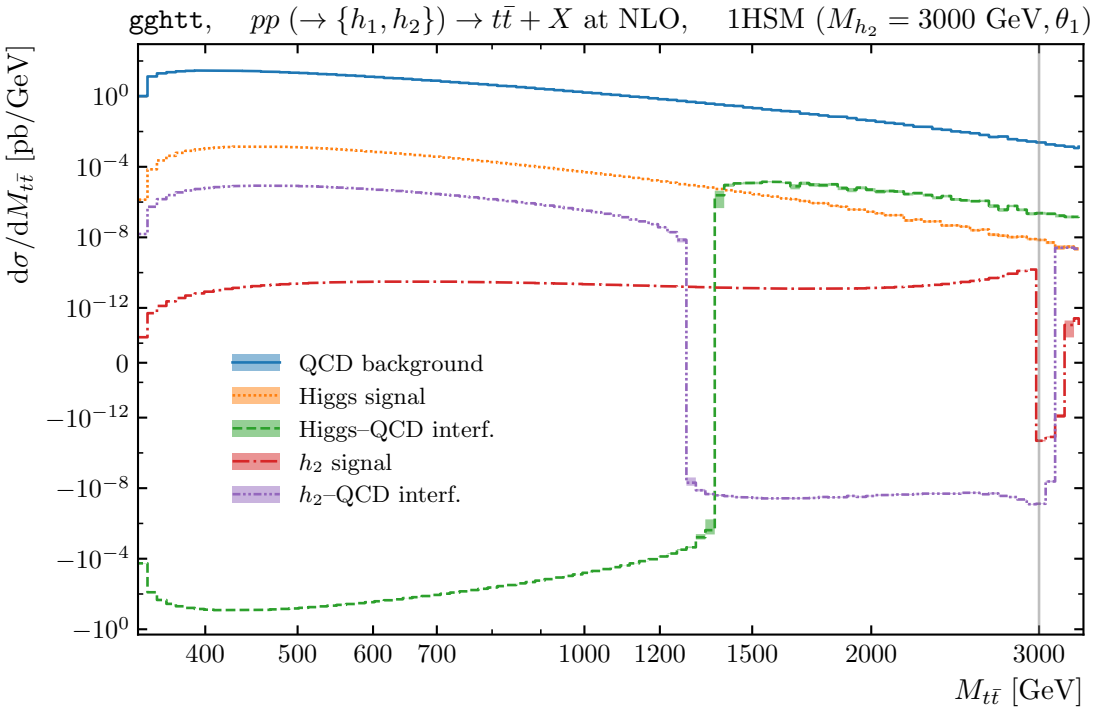

Figure 6.21. Differential distributions in $M_{t\bar{t}}$ for the process $pp\,(\to\{h_1,h_2\})\to t\bar{t}+X$ at NLO in the 1HSM extension for $M_{h_2}=3$ TeV, $\theta=\theta_1=\pi/45$.

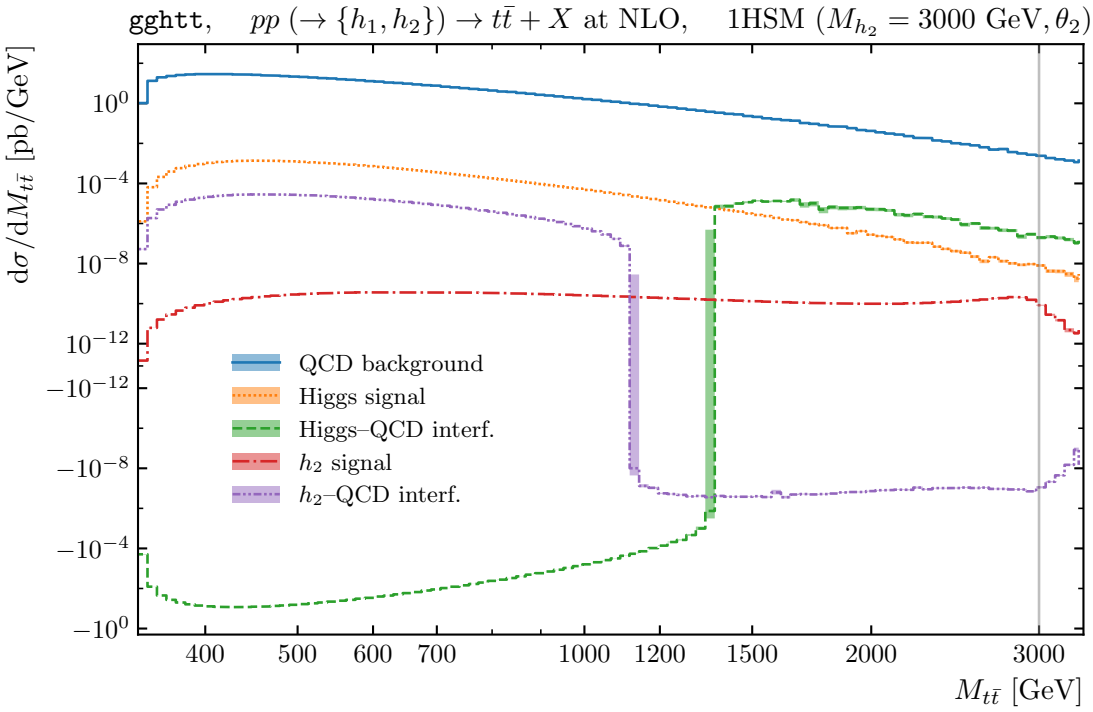

Figure 6.22. Differential distributions in $M_{t\bar{t}}$ for the process $pp\,(\to\{h_1,h_2\})\to t\bar{t}+X$ at NLO in the 1HSM extension for $M_{h_2}=3$ TeV, $\theta=\theta_2=\pi/24$.

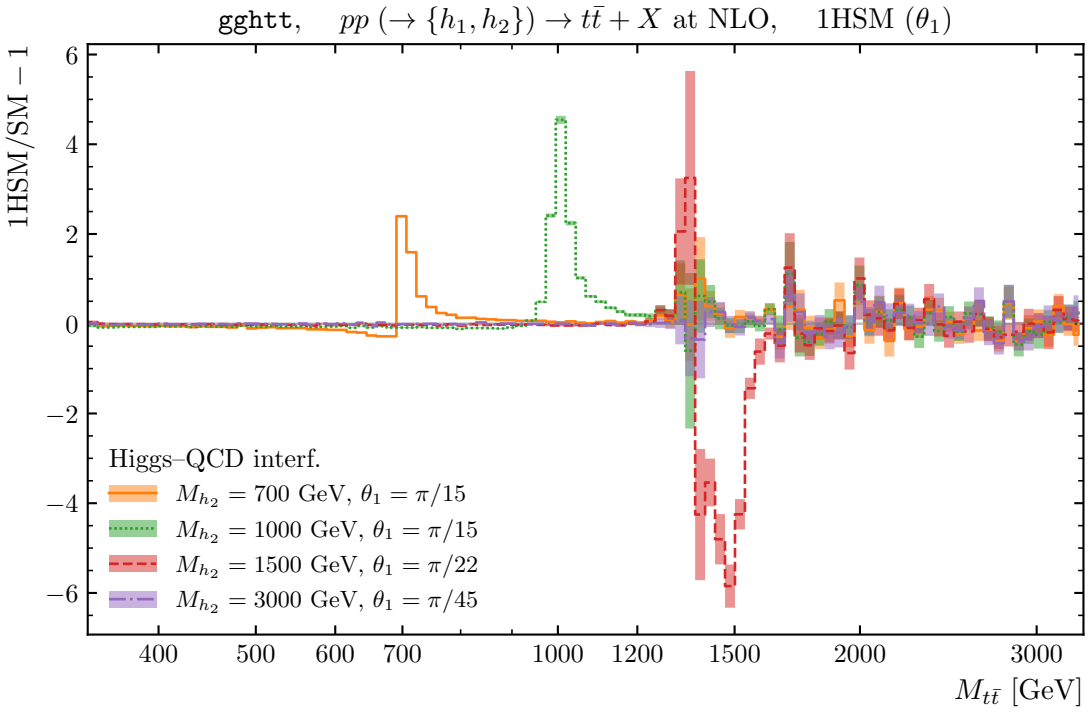

Figure 6.23. Distributions in the invariant mass, $M_{t\bar{t}}$, for the relative difference 1HSM/SM−1 of the Higgs–QCD interference for the process $pp\,(\to\{h_1,h_2\})\to t\bar{t}+X$ for benchmark points with $\theta=\theta_1$.

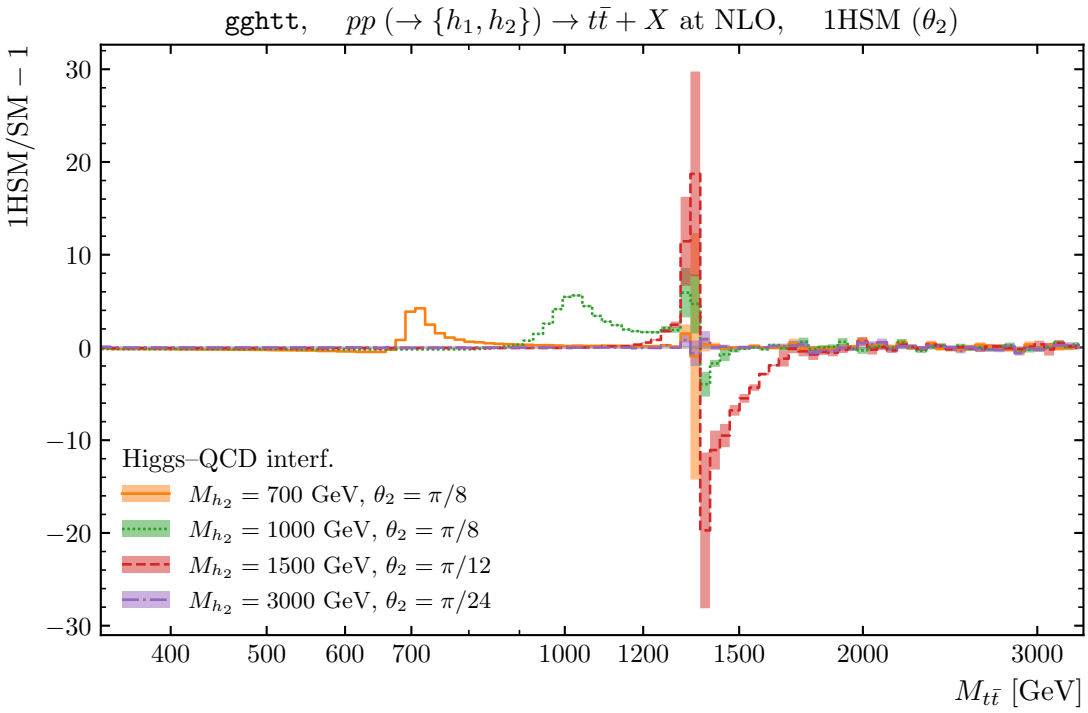

Figure 6.24. Distributions in the invariant mass, $M_{t\bar{t}}$, for the relative difference 1HSM/SM−1 of the Higgs–QCD interference for the process $pp\,(\to\{h_1,h_2\})\to t\bar{t}+X$ for benchmark points with $\theta=\theta_2$.

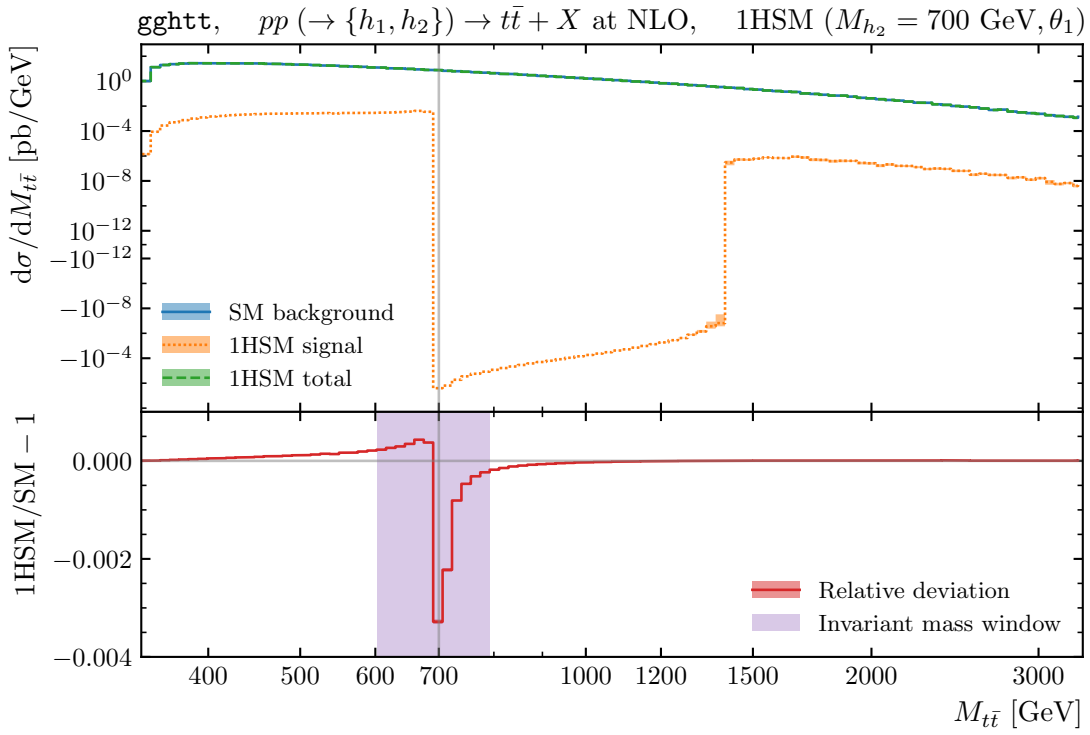

Figure 6.25. Differential distributions in $M_{t\bar{t}}$ for the process 1HSM signal with $M_{h_2} = 700$ GeV, $\theta = \theta_1 = \pi/15$, against the SM background.

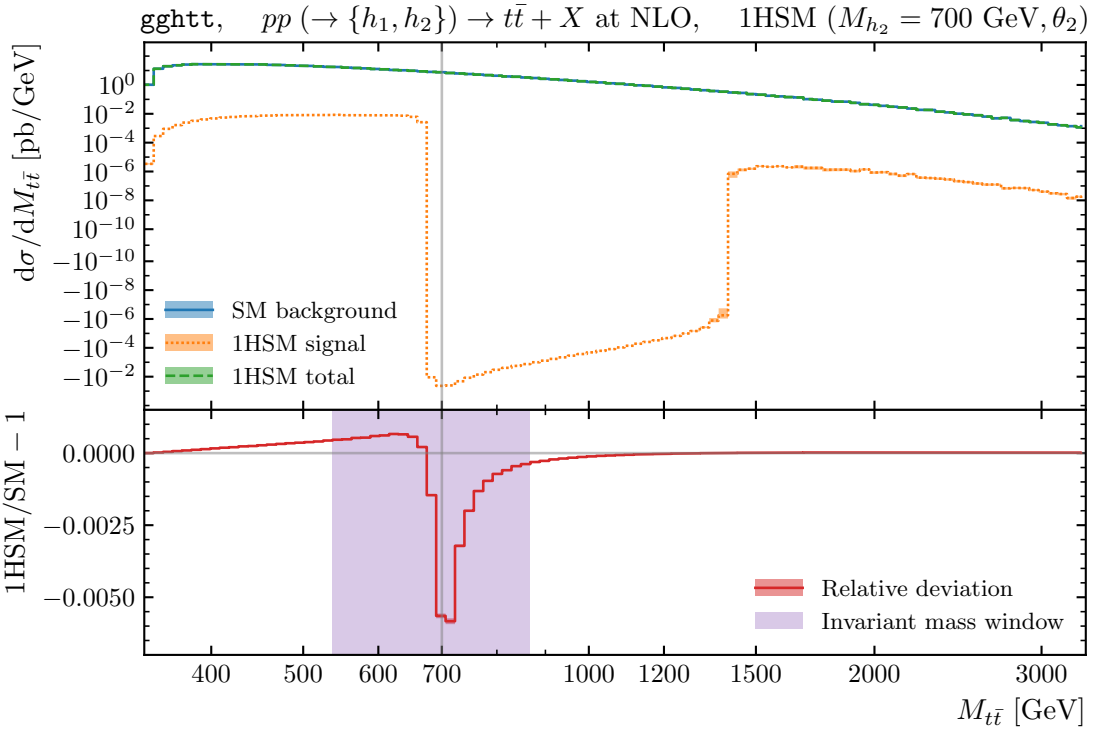

Figure 6.26. Differential distributions in $M_{t\bar{t}}$ for the process 1HSM signal with $M_{h_2} = 700$ GeV, $\theta = \theta_2 = \pi/8$, against the SM background.

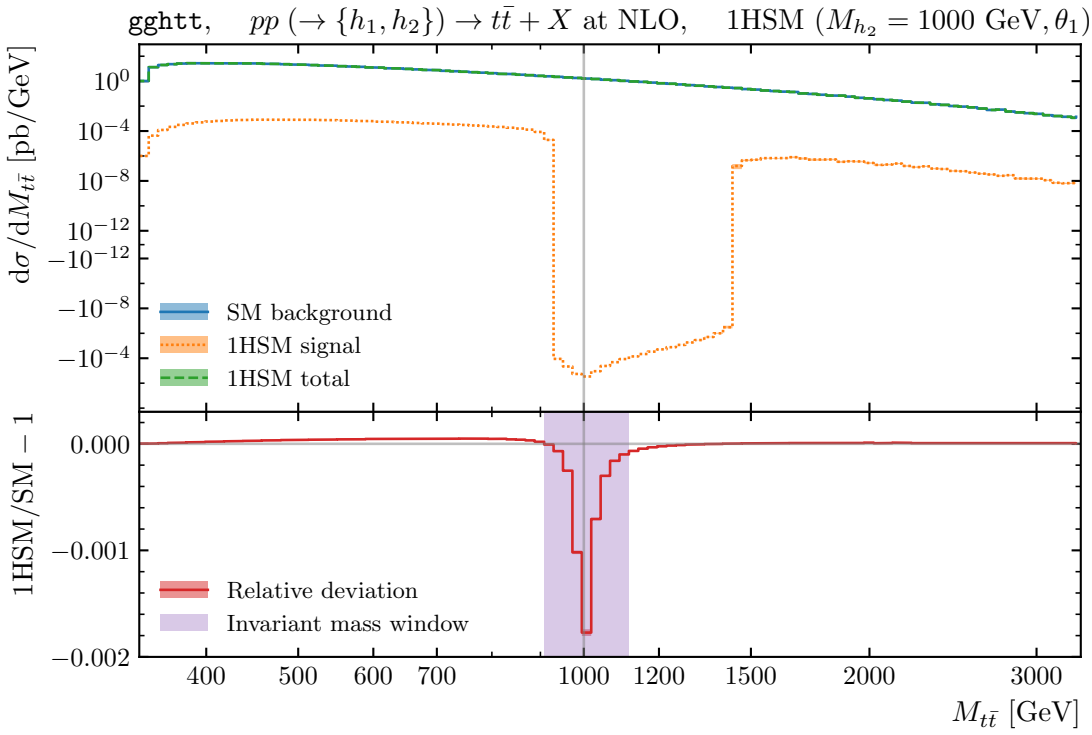

Figure 6.27. Differential distributions in $M_{t\bar{t}}$ for the process 1HSM signal with $M_{h_2} = 1$ TeV, $\theta = \theta_1 = \pi/15$, against the SM background.

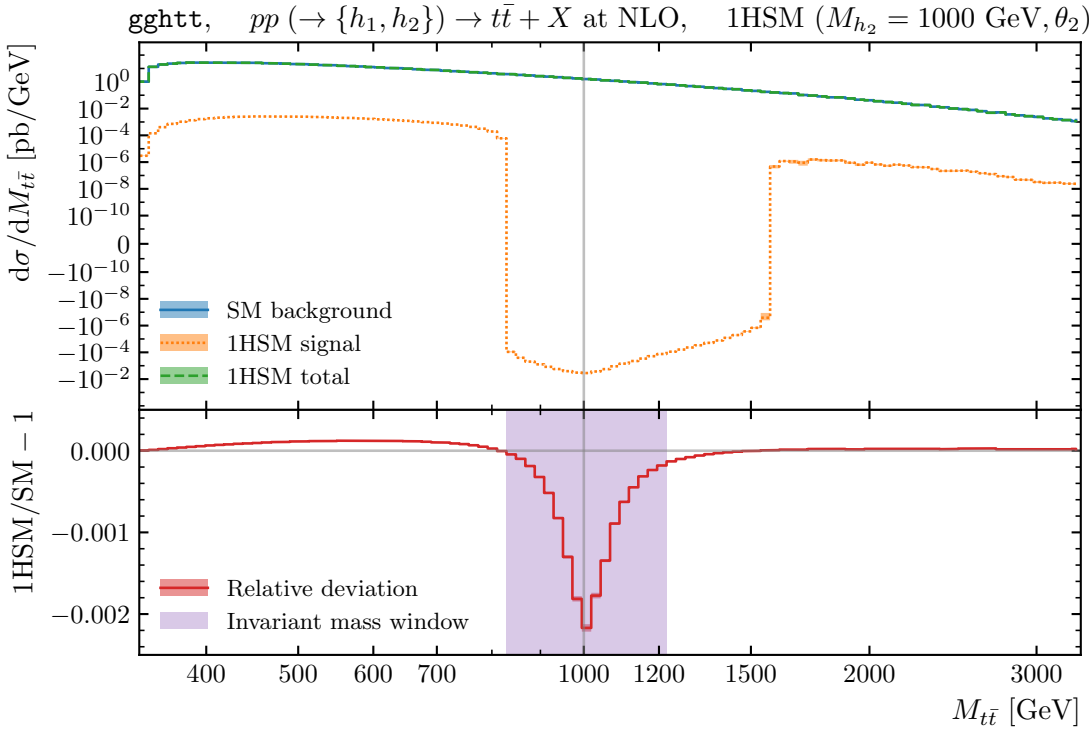

Figure 6.28. Differential distributions in $M_{t\bar{t}}$ for the process 1HSM signal with $M_{h_2} = 1$ TeV, $\theta = \theta_2 = \pi/8$, against the SM background.

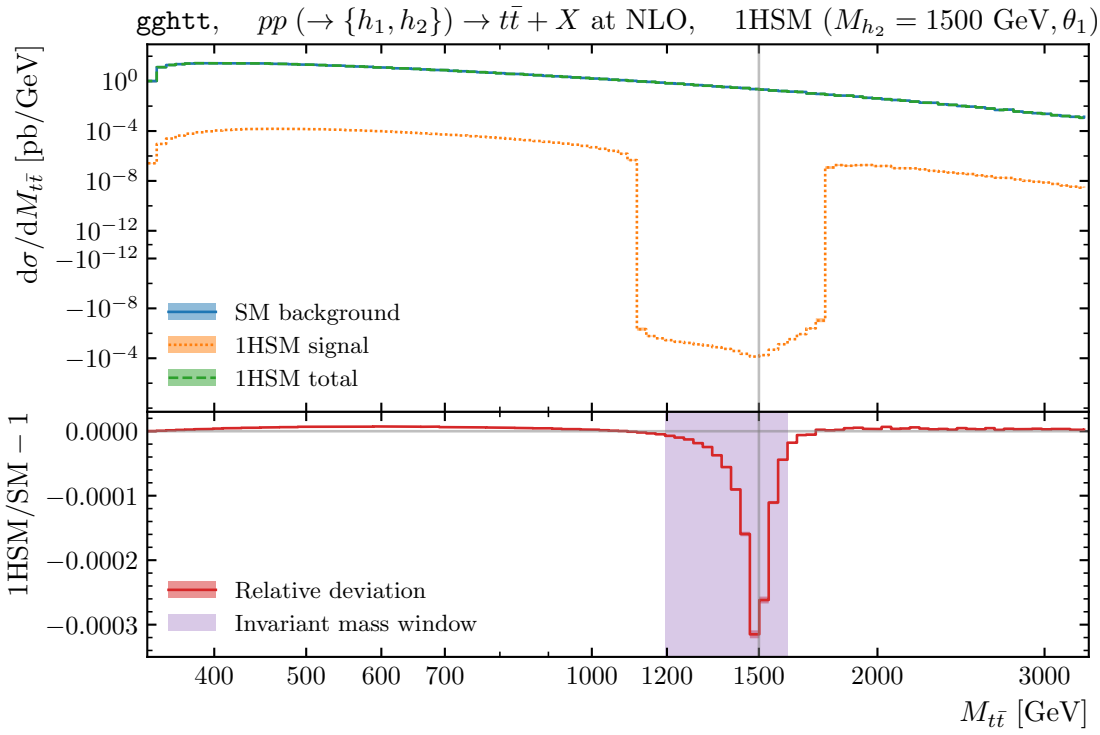

Figure 6.29. Differential distributions in $M_{t\bar{t}}$ for the process 1HSM signal with $M_{h_2} = 1.5$ TeV, $\theta = \theta_1 = \pi/22$, against the SM background.

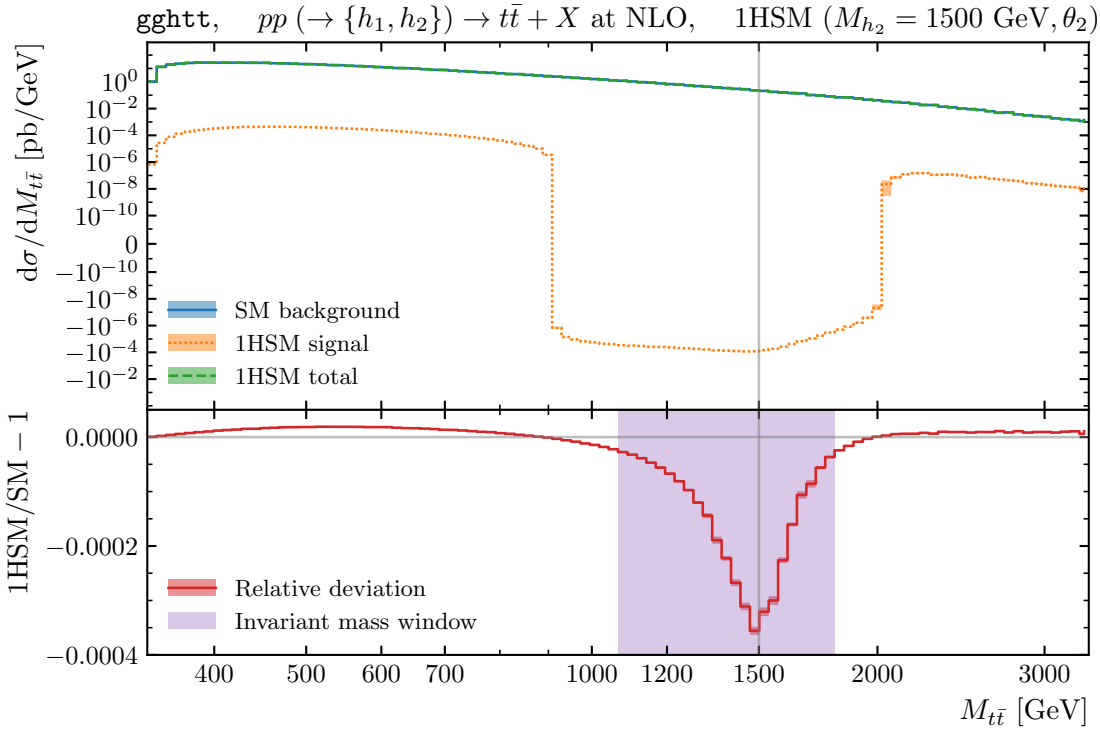

Figure 6.30. Differential distributions in $M_{t\bar{t}}$ for the process 1HSM signal with $M_{h_2} = 1.5$ TeV, $\theta = \theta_2 = \pi/12$, against the SM background.

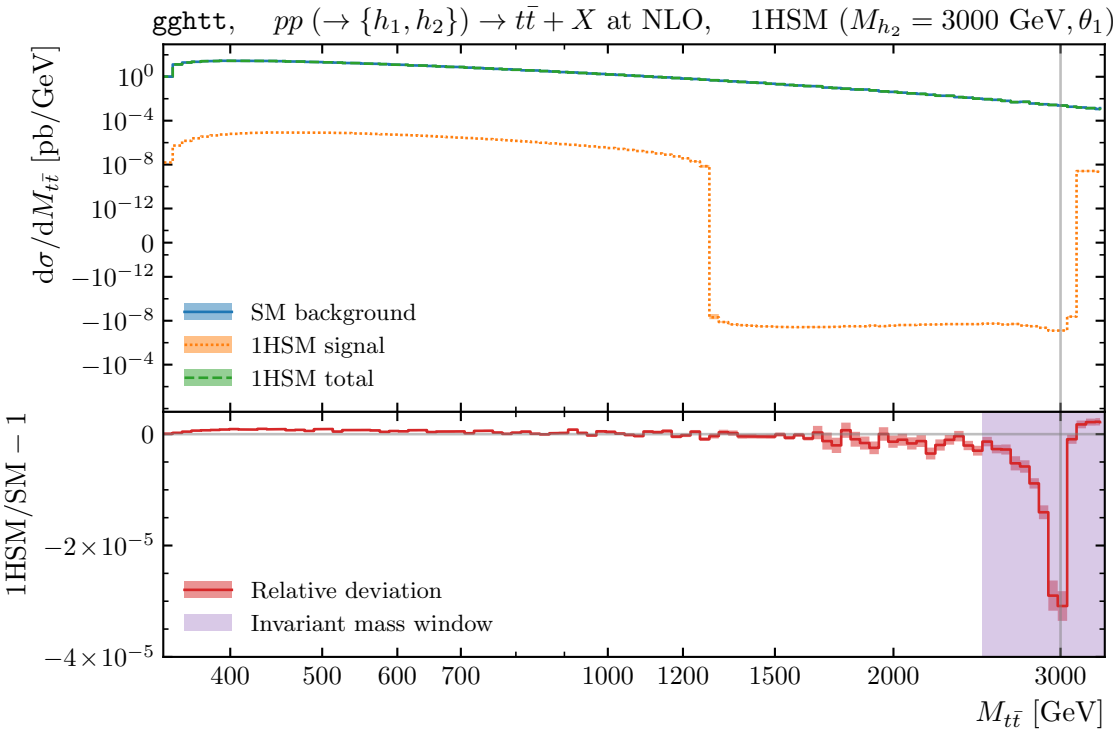

Figure 6.31. Differential distributions in $M_{t\bar{t}}$ for the process 1HSM signal with $M_{h_2} = 3$ TeV, $\theta = \theta_1 = \pi/45$, against the SM background.

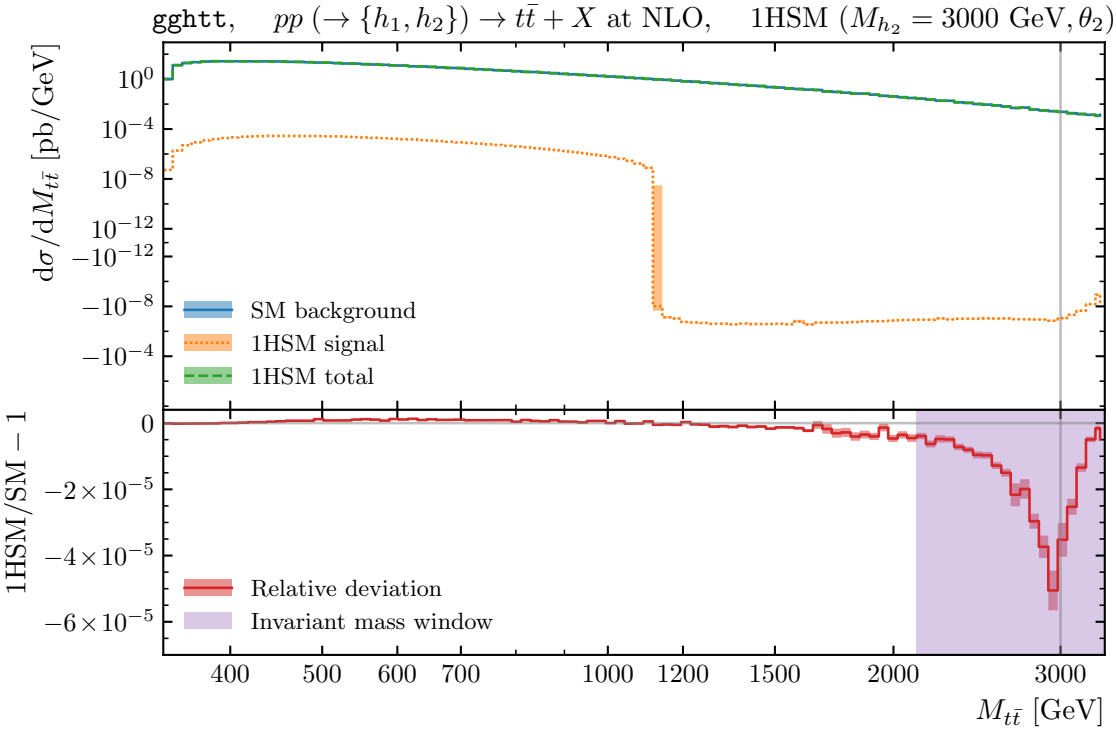

Figure 6.32. Differential distributions in $M_{t\bar{t}}$ for the process 1HSM signal with $M_{h_2} = 3$ TeV, $\theta = \theta_2 = \pi/24$, against the SM background.

As expected, the invariant mass distributions of the light Higgs resonance h_1 signal resembles that of the Standard Model Higgs H. The invariant mass distributions of the heavy Higgs resonance exhibits a Breit–Wigner line shape around the respective resonance mass, with a shoulder extending down to $2m_t$. This shoulder is due to an enhancement from the gluon PDFs as explained in section 6.1.

Across the invariant mass spectrum, for each benchmark point, the absolute value of the h_2–QCD interference is larger than that of the h_2 signal. Notably the Higgs–QCD interference acquires a dip structure around the resonance mass as compared to the SM distribution. This is clearly shown in Figure 6.23 and 6.24, where the dip structures causes deviations of around 240%, 450%, and 590% for $M_{h_2} = 700$ GeV, 1 TeV, and 1.5 TeV respectively for the benchmark points with θ_1. The benchmark points with θ_2 shows larger deviations of around 420%, 590%, and 1970% for $M_{h_2} = 700$ GeV, 1 TeV, and 1.5 TeV respectively, and with more spread out dip structures over a larger invariant mass range. This is due to the heavy Higgs decay widths depending on the mixing angle – a large decay width will result in a wider Breit–Wigner line shape, which will affect the dip structure observed in the interference. Notably, any deviations of the Higgs–QCD interference from the SM distribution are not observed for the benchmark points with $M_{h_2} = 3$ TeV.

Figure 6.25 – 6.32 highlights the size of the overall 1HSM deviations relative to the SM background. The deviations are around 0.33%, 0.18%, 0.032%, and 0.0031% for $M_{h_2} = 0.7$, 1, 1.5, and 3 TeV respectively, for the benchmark points with θ_1, while the deviations are around 0.58%, 0.22%, 0.036%, and 0.0051% for $M_{h_2} = 0.7$, 1, 1.5, and 3 TeV respectively, for the benchmark points with θ_2. The deviation in the overall 1HSM signal for the benchmark points with $M_{h_2} = 3$ TeV is due to the h_2 resonance signal only.

Additional distributions over the average p_T of the $t\bar{t}$ pair, $p_{T,\text{average}} = (p_{T,t} + p_{T,\bar{t}})/2$, and the transverse mass of the $t\bar{t}$ system, $M_{T,t\bar{t}}$, are available in Appendix C. These observables have been considered as they are not sensitive to the radiated jet from the real emissions. The $p_{T,\text{average}}$ distributions shows a similar dip in the interference as the invariant mass distributions, albeit slightly smaller. The $M_{T,t\bar{t}}$ distributions are likewise highly similar to the invariant mass distributions, as the process considered is very inclusive.

6.7.3 Significance Estimations

In order to estimate the significance from Poisson statistics, $S/\sqrt{B}$, [187] of the 1HSM signal, it will be necessary to estimate the expected number of events. The number of events is related to the cross-section through the *integrated luminosity* $\mathcal{L}$,

$$N = \sigma\mathcal{L}\,, \tag{6.35}$$

hence the significance becomes

$$\frac{S}{\sqrt{B}} = \sqrt{\mathcal{L}}\frac{\sigma_S}{\sqrt{\sigma_B}}\,. \tag{6.36}$$

The full LHC Run 2 data sample for pp collisions corresponds to an integrated luminosity of $\mathcal{L} = 1.39 \times 10^5$ pb^{-1} [188]. The projected integrated luminosity for LHC Run 3 is $\mathcal{L} \approx 3 \times 10^5$ pb^{-1}, and $\mathcal{L} \approx 3 \times 10^6$ pb^{-1} for the future high luminosity (HL-LHC) upgrade [189].

The signal S is taken to be the Higgs–QCD interference, while the background B is taken to be the continuum QCD background. Technically, the heavy Higgs resonance and its interference to the light Higgs contributes to the signal, but can be reasonably neglected as indicated from the integrated cross-section results presented in subsection 6.7.1 and Appendix C. The light Higgs resonance will likewise contribute to the SM background but is negligible as well.

As shown in Figure 6.23 and 6.24, as well as in the ratio plots of Figure 6.25 – 6.32, the contribution of the heavy Higgs to the interference is the dip structure located at the resonance mass. The significances have been calculated in invariant mass windows that have been chosen around the dip structures for each benchmark point, and based on the deviations of the total 1HSM signal to the SM background. The invariant mass windows are illustrated for each benchmark points in the ratio plots of Figure 6.25 – 6.32. The benchmark points with a significance of $S/\sqrt{B} > 2\sigma$, i.e. excludable at $\sim 95\%$ confidence level, are shown in Table 6.9 for the LHC Run 2 and projected Run 3 and HL-LHC data samples, along with the respective invariant mass windows. Approximate values, rounded to the nearest ten, for the end points of the mass windows are given, as they are selected from bin end points corresponding to distributions in $\ln M_{t\bar{t}}$. The benchmark points with $M_{h_2} = 700$ GeV can all be excluded with the data sample from Run 2. However, benchmark points with $M_{h_2} = 1.5$ TeV or above cannot be excluded even for the HL-LHC. These results

may change if taking into account top decays with a proper simulation of detector cuts.

	M_{h_2} [GeV]	Invariant mass window	Excludable Run 2	Run 3	HL-LHC
θ_1	700	600–790 GeV	✓	✓	✓
	1000	900–1115 GeV	–	–	✓
	1500	1200–1600 GeV	–	–	–
	3000	2500–3340 GeV	–	–	–
θ_2	700	530–870 GeV	✓	✓	✓
	1000	830–1200 GeV	–	✓	✓
	1500	1050–1800 GeV	–	–	–
	3000	2100–3340 GeV	–	–	–

Table 6.9. The 1HSM benchmark points that can be excluded at a 95% confidence level in the corresponding data samples for the LHC Run 2 and the future Run 3 and HL-LHC.

6.7.4 Theoretical Uncertainties from Scale Variations

In order to estimate the theoretical uncertainties, the LO and NLO cross-sections have been evaluated for one of the benchmark points ($M_{h_2} = 1.5$ TeV, θ_1) while varying the renormalisation and factorisation scale. A symmetrical three-point scale variation has been used with $\mu_R = \mu_F = \{\mu/2, \mu, 2\mu\}$, for $\mu = M_{t\bar{t}}/2$.

The LO and NLO integrated cross-sections with theoretical uncertainties for each contribution are shown in Table 6.10. For the QCD background the NLO theoretical uncertainty is around 12%, while for the Higgs–QCD interference the theoretical uncertainty is at 19–31%. The h_2–QCD interference is in particular sensitive to the scale variations with a theoretical uncertainty of 27–42%.

Distributions in the invariant mass, $M_{t\bar{t}}$, for the theoretical and statistical uncertainties are shown for NLO in Figure 6.33 and for LO in Figure 6.34. The theoretical uncertainties are indicated by the light shaded bands, while the statistical uncertainties are indicated by the dark shaded bands. Naturally, the statistical errors can be decreased by simply generating more events. However, since the theoretical uncertainty estimates themselves carry statistical errors, it is informative to indicate the relative size of the statistical errors, especially for high $M_{t\bar{t}}$. The large peaks in

Contribution	σ_{NLO} [pb]	σ_{LO} [pb]
QCD background	$6.8^{+0.9}_{-0.8} \times 10^2$	$4.2^{+1.2}_{-0.9} \times 10^2$
Higgs signal	$3.0^{+0.6}_{-0.5} \times 10^{-2}$	$1.8^{+0.5}_{-0.4} \times 10^{-2}$
Higgs–QCD interference	$-1.6^{+0.3}_{-0.5}$	$-0.7^{+0.2}_{-0.2}$
h_1 signal	$3.0^{+0.6}_{-0.5} \times 10^{-2}$	$1.8^{+0.5}_{-0.4} \times 10^{-2}$
h_2 signal	$2.7^{+0.6}_{-0.5} \times 10^{-6}$	$2.2^{+0.8}_{-0.5} \times 10^{-6}$
h_2–QCD interference	$3.3^{+1.4}_{-0.9} \times 10^{-3}$	$1.4^{+0.4}_{-0.3} \times 10^{-3}$

Table 6.10. The integrated LO and NLO cross-sections with theoretical uncertainties due to scale variations for the various contributions for the 1HSM benchmark point with $M_{h_2} = 1.5$ TeV, $\theta = \theta_1 = \pi/22$.

the Higgs–QCD and h_2–interference distributions for the theoretical uncertainty may be due to final-state gluon emissions not being included in the definition of $M_{t\bar{t}}$. This may also be the reason for the increasing error on the h_2 signal for $M_{t\bar{t}} \to 2m_t$. The theoretical uncertainty distributions for the LO results show little deviation across the $M_{t\bar{t}}$ range.

6.8 Conclusion and Outlook

This chapter has presented an investigation into the NLO corrections to Higgs interference effects in top-quark pair production in the 1HSM. The interference between the heavy Higgs and the QCD background has been found to heavily dominate, with NLO QCD corrections being important. The deviation in the interference effect from the SM behaviour has been found to be excludable at 95% confidence level for the projected Run 3 and the HL-LHC for heavy Higgs masses up to at least 700 GeV, and in some benchmark points up to 1 TeV.

The structure of the corresponding interference process is unusual as the leading-order is induced by a tree-loop interference. Correspondingly the NLO computation consists at the virtual level of two-loop contributions in interference with tree amplitudes together with loop-loop interferences, while the real radiation contributions are induced by tree-loop interferences. As currently available NLO tools are unable to handle such a structure, a novel NLO Monte Carlo framework has been developed. In this framework the phase space integration has been performed using Kaleu, and the dipole subtraction has been derived from the implementation in Helac-

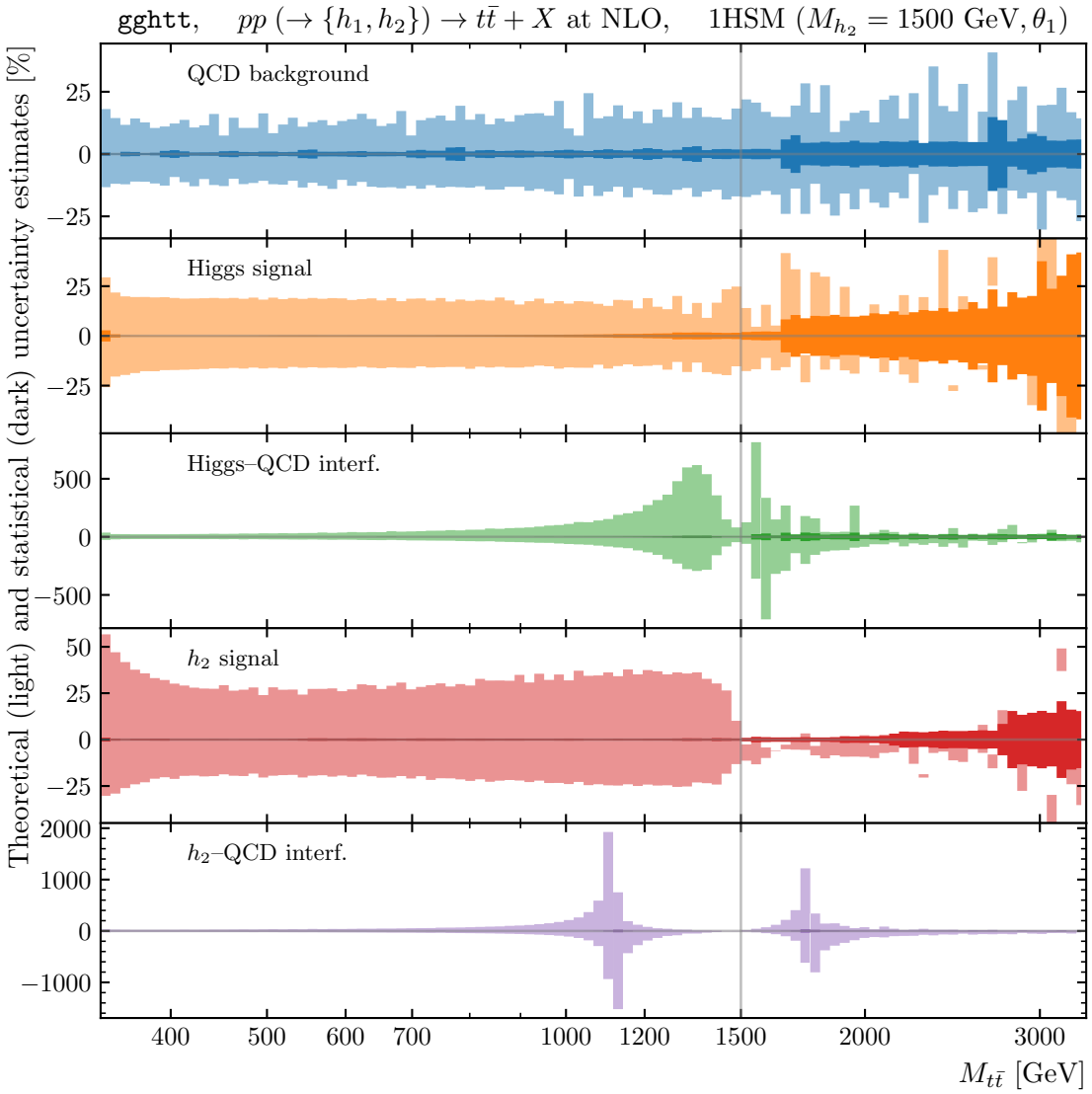

Figure 6.33. NLO distributions in the invariant mass, $M_{t\bar{t}}$, for the theoretical (light shaded) and statistical (dark shaded) uncertainties.

Dipoles. All tree and loop matrix elements have been obtained with a modified version of OpenLoops, where a dedicated interface to extract colour-correlated helicity amplitudes has been implemented. Finally, the two-loop virtual amplitudes has been incorporated via tree-level OpenLoops amplitudes within a novel form-factor based approach using CHAPLIN for the required harmonic polylogarithms. The framework is highly flexible and will allow for efficient computation of further loop-tree and/or loop-squared induced processes at NLO. This covers a gap in the event generator landscape and will e.g. facilitate studies of loop-induced processes affected by EFTs, an area which still remains largely unexplored.

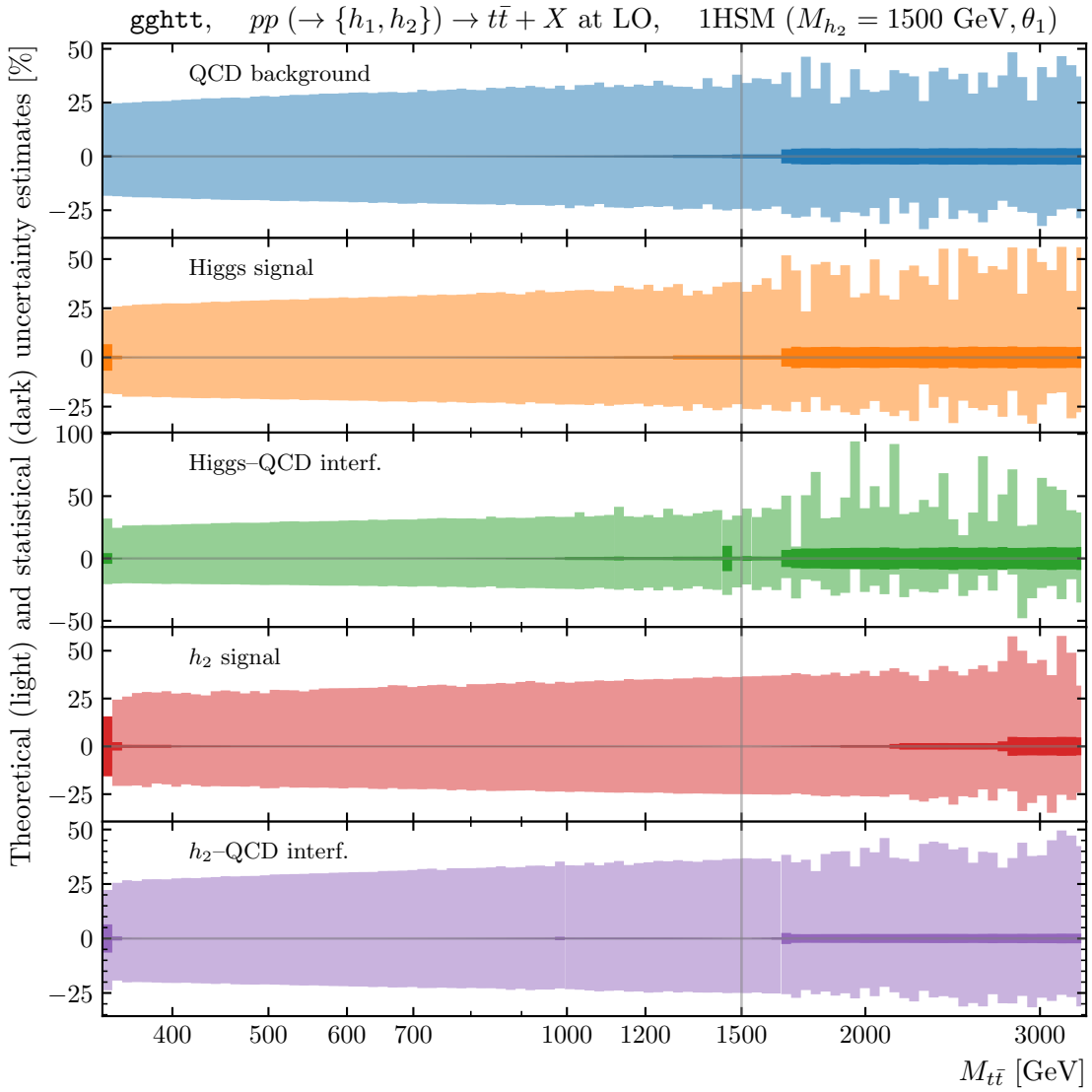

Figure 6.34. LO distributions in the invariant mass, $M_{t\bar{t}}$, for the theoretical (light shaded) and statistical (dark shaded) uncertainties.

The following sections will present some of the ways the Higgs interference study presented in this chapter can be extended in future work.

6.8.1 Decays of the Top and Anti-Top Quarks

The top quark is not stable and will decay before undergoing hadronisation. Hence, a further study should include decays of the on-shell $t\bar{t}$ pair. The decay channel

could be the leptonic channel,

$$\begin{aligned} t &\to W^+ b \to \bar{\ell}\nu b \\ \bar{t} &\to W^- \bar{b} \to \ell' \bar{\nu}' \bar{b}\,, \end{aligned} \tag{6.37}$$

as shown in Figure 6.35. This will have a clean experimental signature compared to the hadronic decay channel, due to the dominating QCD background at hadron colliders.

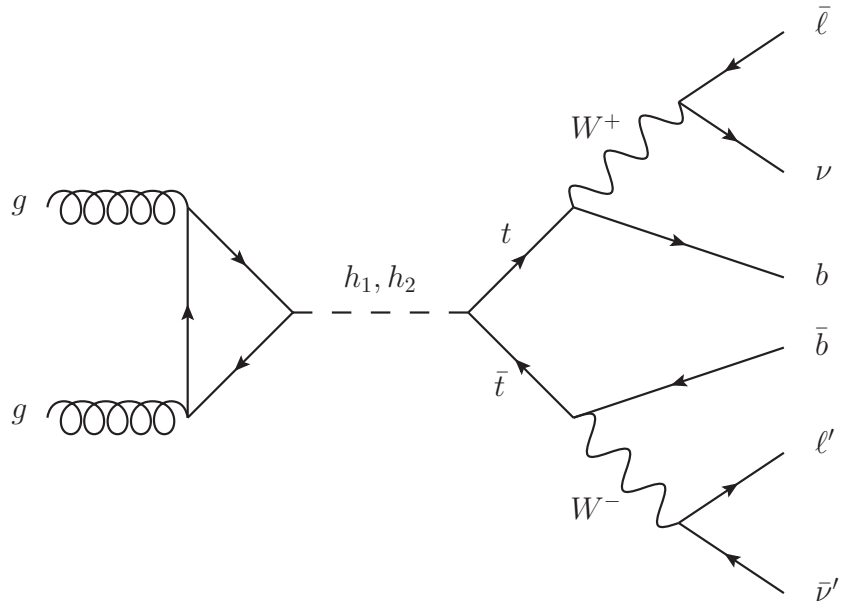

Figure 6.35. Feynman diagram for the LO signal with the decays of the on-shell $t\bar{t}$.

When taking into account top decays, the fiducial volume of the ATLAS and CMS experiments at the LHC can be simulated by taking into account a simplified version of the experimental detector cuts on the final-state leptons and jets from refs. [190, 191].

Since it is not possible to specify on-shell intermediate particles in KALEU, KALEU can provide the phase space for the on-shell $t\bar{t}$ production, while the subsequent decay phase space can be handled by a custom code. This code is already available in `gghtt` and has been adapted from MCFM [76–79].

6.8.2 Dipole Subtraction for Intermediate Emitters

Soft singularities can arise from radiative emissions from intermediate resonant propagators. Hence, the on-shell top quarks should be treated as emitters, even

when considering their decay. This is in contrast to the full calculation with off-shell top quarks, where the intermediate propagators are not IR divergent. These "intermediate" dipoles must be treated in a modified version of the Catani–Seymour subtraction scheme, as described in ref. [192]. The dipole subtraction at NLO is applied for the $pp \to t\bar{t}$ production, which is then convoluted with the LO top and anti-top decay matrix elements. Radiation from the top decays is not considered here. The Catani–Seymour mapping, $p \to \widetilde{p}$, of the emitter and spectator four-momenta is applied to the four-momenta of the $t\bar{t}$ pair which is reconstructed from the four-momenta of their decay products. The mapping then has to be carried over to the decay products of the top quarks. The four-momenta of the decay products of the top quarks are subject to mass-shell constraints,

$$\widetilde{p}_t^2 = p_t^2 = m_t^2, \quad \widetilde{p}_W^2 = p_W^2, \quad \widetilde{p}_b^2 = p_b^2 = m_b^2, \quad \widetilde{p}_\ell^2 = p_\ell^2 = \widetilde{p}_\nu^2 = p_\nu^2 = 0\,, \tag{6.38}$$

hence the mapping of the decay products can be achieved with a Lorentz transformation, constructed as the product of two boosts. The four-momenta of the intermediate top quarks will be the same in their centre-of-mass (CoM) frames,

$$p_t^{\mathrm{CoM}} = \Lambda p_t = \widetilde{p}_t^{\mathrm{CoM}} = \widetilde{\Lambda}\widetilde{p}_t = \left(m_t, \vec{0}\right)\,, \tag{6.39}$$

where Λ and $\widetilde{\Lambda}$ are the boosts bringing their respective four-momenta into their CoM frames. Based on this observation, the resulting Lorentz transformation becomes

$$\widetilde{p}_t = \left(\widetilde{\Lambda}^{-1}\Lambda\right) p_t\,, \tag{6.40}$$

which is applied to the top decay products in order to construct the final mapped four-momenta [192]. The full mapping procedure is illustrated in Figure 6.36.

The code for this mapping procedure has been implemented in `gghtt`.

The top decays can be treated at NLO by extending the Catani–Seymour subtraction scheme as in refs. [193] and [194]. Indeed, virtual corrections and real emissions in the top decays can have an important effect on many relevant observables.

6.8.3 Spin Correlations in the Top Decays

Since the lifetime of the top quark ($\hbar/\Gamma_t \sim 10^{-25}$ s) is shorter than the time scale for QCD hadronisation effects ($1/\Lambda_{\mathrm{QCD}} \sim 10^{-23}$ s), and much shorter than the time scale for spin decorrelation ($m_t/\Lambda_{\mathrm{QCD}}^2 \sim 10^{-21}$ s) [195], the spin information of the

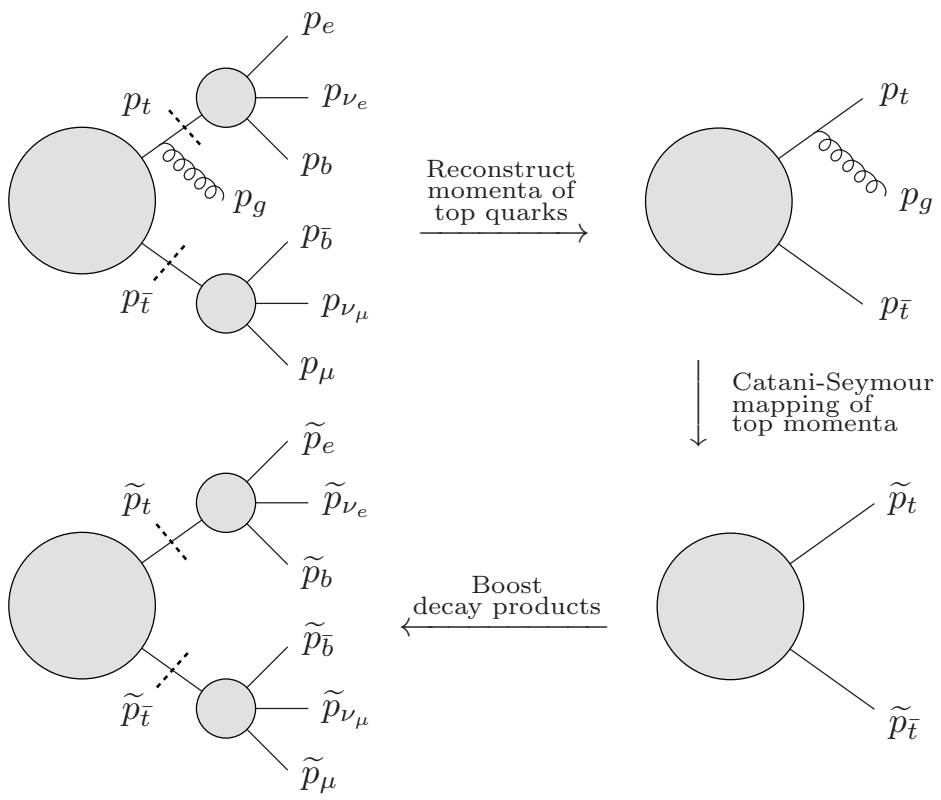

Figure 6.36. The phase space mapping procedure applied to an intermediate emitter. Shown here for a final-final dipole with a top quark as the emitter, and the anti-top as the spectator.

top quark will be directly transferred to its decay products. Spin correlations of the top and the anti-top pair in $t\bar{t}$ production are predicted in the SM and have been experimentally observed at the LHC [196, 197] and the Tevatron [198, 199]. The charged leptons from the leptonically decaying W bosons will carry most of the spin information from the decayed top quark [200–203], hence angular observables, such as the azimuthal opening angle $\Delta\phi_{\ell\ell'}$ between the two leptons, is in particular sensitive to the $t\bar{t}$ spin correlations [204]. It will therefore be necessary to include spin correlations in a further study that includes decays of the top quarks.

6.8.4 Generalising and Extending `gghtt`

The `gghtt` event generator has been written in a way so that it can easily be generalised to compute other loop-induced processes, including interference effects, at NLO, such as double Higgs production, $gg \to HH$, provided that the form factors

are implemented in the new OpenLoops interface. Other processes of interest could include W^+W^- and ZZ production. A generalised version of `gghtt` could facilitate studies of several BSM models, e.g. the inclusion of dimension-6 or dimension-8 operators.

Technical features of `gghtt` can easily be added. A generalised version could allow saving events in a HepMC [90, 91] format instead of writing out the specified histograms as is currently the case. Instead of taking a few, simple command line options, `gghtt` can be extended to accept an input file with function parsing, that allows setting cuts and specifying histograms at runtime, instead of having to hack the code and recompile. In addition, `gghtt` is written in a modular way, such that each part can be switched out with an alternative, if desired. For example, the phase space generation can easily be provided by a custom code instead of Kaleu.

While the Monte Carlo method as described in subsection 4.4.1 is a powerful and versatile integration method, especially useful for complicated and multi-dimensional integrals, it can also be rather slow as already explained for the case of H1jet. Hence, parallelisation of a generalised version of `gghtt` may be beneficial. This could be achieved using multi-threading with OpenMP. However, this would require ensuring thread-safety of Kaleu and OpenLoops. Currently, `gghtt` allows setting a seed for the random number generator at runtime, and outputting the histograms with the sum of weights and sum of squared weights, rather than the calculated $\mathrm{d}\sigma$ and associated error. This allows for simple parallelisation when running on a high performance cluster (HPC). This feature was used when generating the results for this thesis.

7

Concluding Remarks

This thesis has presented two phenomenological research projects focusing on the physics of Higgs bosons in QCD processes at the LHC. A major output of this thesis has been the development of two new flexible and easy-to-use tools for precision studies of BSM models as mapped onto EFTs.

The first tool, H1JET, returns a transverse momentum spectrum of a given colour singlet in about a second. H1JET implements various processes, including Higgs production both in gluon fusion and bottom–anti-bottom annihilation, as well as Z production. Loop-induced Higgs production is implemented in the SM, as well as several attractive BSM scenarios, such as a simplified SUSY model and composite Higgs models. Furthermore, H1JET allows for automatic implementation of new processes and models through a provided user interface. In addition, input files can be used to obtain results for any given number of fermions and scalars in the loops for Higgs production, with appropriate couplings. This can be used to implement e.g. the MSSM instead of the provided simplified SUSY model. H1JET is well suited for quick parameter scans of BSM models, and for precision phenomenology in studies of the p_T spectrum of a colour singlet, especially when involving the matching of resummed calculations with exact fixed order. Finally, H1JET can be extended to include higher orders, provided one integrates over all coloured particles.

The second tool, `gghtt`, covers a gap in the event generator landscape by facilitating studies of loop-induced processes affected by EFTs, an area which is not otherwise easily accessible. The generalised `gghtt` code can be used to study various processes, such as double Higgs production, $gg \to HH$, or e.g. ZZ and W^+W^-

production, while considering dimension-6 and dimension-8 operators.

In chapter 6, `gghtt` was used to study Higgs interference effects at NLO in the process $pp\ (\to \{h_1, h_2\}) \to t\bar{t} + X$ in the 1-Higgs-singlet model, introducing an additional heavy Higgs resonance, h_2, which mixes with the light Higgs boson, h_1, assumed to be the observed scalar with a mass of 125 GeV. The interference effects was studied for benchmark points with a heavy Higgs mass that significantly exceeds $2m_t$. More specifically, the M_{h_2} range 700–3000 GeV was studied with mixing angles compatible with current limits as well as a second set of mixing angles, roughly twice as large, to illustrate the dependence on the mixing angle. The interference between the heavy Higgs boson and the continuum QCD background was found to dominate over the absolute-squared heavy Higgs resonance signal. The h_2–QCD interference introduces a dip structure around the heavy resonance mass in the invariant mass distributions. The significance and excludability of this dip structure was explored for the LHC Run 2 and projected Run 3 and HL-LHC. It is clear from the results that full NLO corrections are essential for interference-guided searches of heavy resonances. Future work could consider spin-correlated decays of the top quarks with a proper simulation of the fiducial detector acceptance. Additional decay channels of the Higgs boson, such as W^+W^- or ZZ, could be studied as well.

It is the hope of the author that these new tools will open new possibilities to employ LHC data to constrain the electroweak symmetry breaking sector of the SM and for broader searches of new physics.

A

Manual for gghtt

This appendix provides a brief manual for the specialised code `gghtt`, a parton-level Monte Carlo event generator developed for the purposes of this thesis to generate events for the process

$$pp\ (\to \{h_1, h_2\}) \to t\bar{t} + X\,, \tag{A.1}$$

at NLO QCD. The process can be calculated in both the Standard Model and the 1-Higgs-singlet model (1HSM) extension.

A.1 Dependencies

The following external packages are required by `gghtt`,

- OpenLoops 2 [45], for tree and loop amplitudes,
- HOPPET [67], for the running of α_s,
- LHAPDF [66], for PDF sets,
- Chaplin [114], for complex harmonic polylogarithms.

In addition, `gghtt` uses Kaleu [175] for the phase space generation. The source code of Kaleu is already included and will be automatically compiled and linked.

By default the `PDF4LHC15_nlo_mc` PDF set [183] will be used. This can be changed in the `pdfs.f90` file. Make sure the local installation of LHAPDF contains the specified PDF set.

gghtt requires a modified version of OpenLoops 2, which is currently under preparation for publication. The new form factor interface in OpenLoops requires Chaplin for the evaluation of the harmonic polylogarithms. Hence, it is necessary to set up a CHAPLIN environment variable with:

```
export CHAPLIN=/path/to/chaplin
```

in order for OpenLoops to compile the form factor interface.

A.2 Installation

The source code for gghtt is available at ref. [122].
The latest version can be checked out with:

```
git clone https://github.com/alexander-lind/gghtt.git
```

The gghtt code can then be compiled with:

```
make OPENLOOPS=/path/to/openloops
```

It is necessary to specify the full path to the OpenLoops installation.

A.3 Usage

After compilation, gghtt can be run from the main directory with:

```
./gghtt
```

The help message will list all available options:

`-h, --help` Display the help message and quit.

The physics process can be selected with:

`-i <arg>` Specify the process. Arguments:

- `ggh` $pp \to H + X$.
- `ttbar` $pp\ (\to \{h_1, h_2\}) \to t\bar{t} + X$ (default).

The ggh option is only available for the SM.
The physics contribution and model can likewise be set:

`-c <value>` Set the contribution. Arguments:

- `signal` Higgs signal only ($h_1 + h_2$ for 1HSM).

	`background`	Continuum QCD background (default).
	`interf`	Higgs-QCD interference.
	`h1`	1HSM light Higgs signal.
	`h2`	1HSM heavy Higgs signal.
	`h1int`	1HSM light Higgs-QCD interference.
	`h2int`	1HSM heavy Higgs-QCD interference.

`-m <value>` Model benchmark point (SM = 0, 1HSM = 1–8), default: 0.

The contribution and model can only set for the `ttbar` process.
`gghtt` allows generating isolated parts of the full NLO calculation. The desired part can be specified with:

`-p <value>` Part of the cross-section to calculate. Arguments:

`lo`	The leading-order result.
`nlo`	The total next-to-leading-order result (default).
`nlocoeff`	The next-to-leading-order coefficient.
`real`	The finite real emission result with dipoles subtracted.
`virt`	The bare virtual result.
`i`	The result from the integrated counterterm I.
`kp`	The result from the integrated counterterms K and P.
`vikp`	The finite virtual result.

By default, `gghtt` will generate a fixed number of events, which can be set with:

`-n <value>` Number of events to be generated, default: 1000000.

If desired, an integration accuracy target can be used instead. Do note that `gghtt` will not be able to estimate the remaining time, and may run for a long time before reaching the target. The accuracy target can be set (in percentage) with:

`-a <value>` Integration accuracy target, alternative to `-n`, default: 0.1%.

The name of the output file with the resulting histograms can be set with:

`-o <string>` Name of output file with histograms, default: `histograms.dat`.

The seed for the random number generator can be set with:

`-s <value>` Set the seed for the RNG (use 0 for "random" seed), default: 314159265.

This will allow for naive parallelisation. If the `-s` option is set to 0, `gghtt` will use the CPU clock cycles as the seed. This is better than using the time, as it will avoid similar seeds if several instances are run simultaneously.
Finally, some additional flags can be set:

`--onlygg` Toggle for including only the gg channel. All channels are included by default.

`--opt` Toggle for running an initial phase space optimisation step. Off by default.

The optimisation step will run for a fixed 100k events, during which the phase space channels in KALEU will be optimised. After the optimisation step, all estimates will be thrown away while keeping the optimised phase space channels. The normal integration step will then be performed with the specified number of events.

B

Standard Model Distributions for $t\bar{t}$ Production

This appendix presents differential distributions for the process $pp\,(\to H) \to t\bar{t} + X$ in the SM. Details are given in chapter 6.

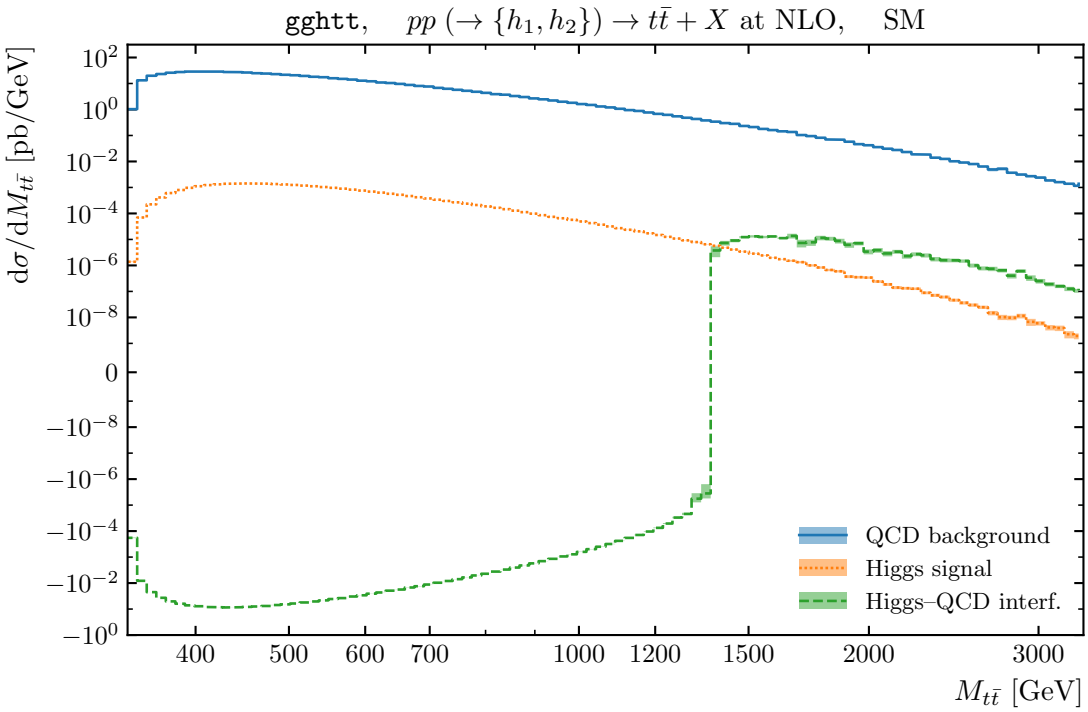

Figure B.1. The differential distributions in $\ln M_{t\bar{t}}$ for the process $pp\,(\to H) \to t\bar{t} + X$ at NLO in the SM.

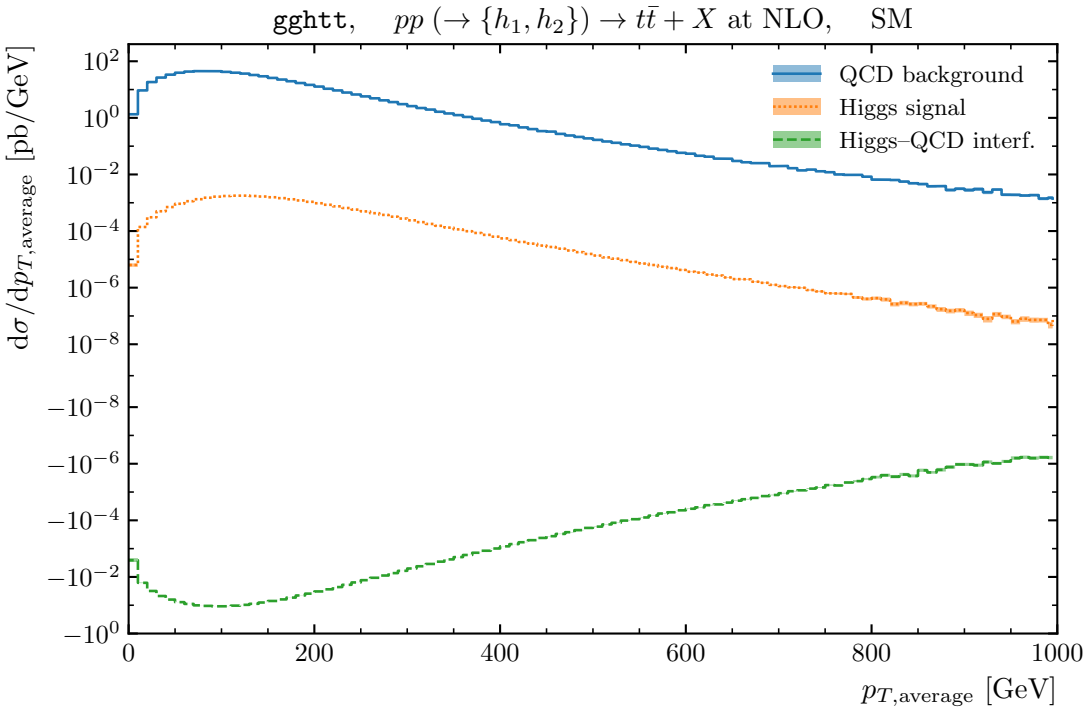

Figure B.2. The differential distributions in $p_{T,\mathrm{average}}$ for the process $pp\,(\to\{h_1,h_2\})\to t\bar{t}+X$ at NLO in the SM.

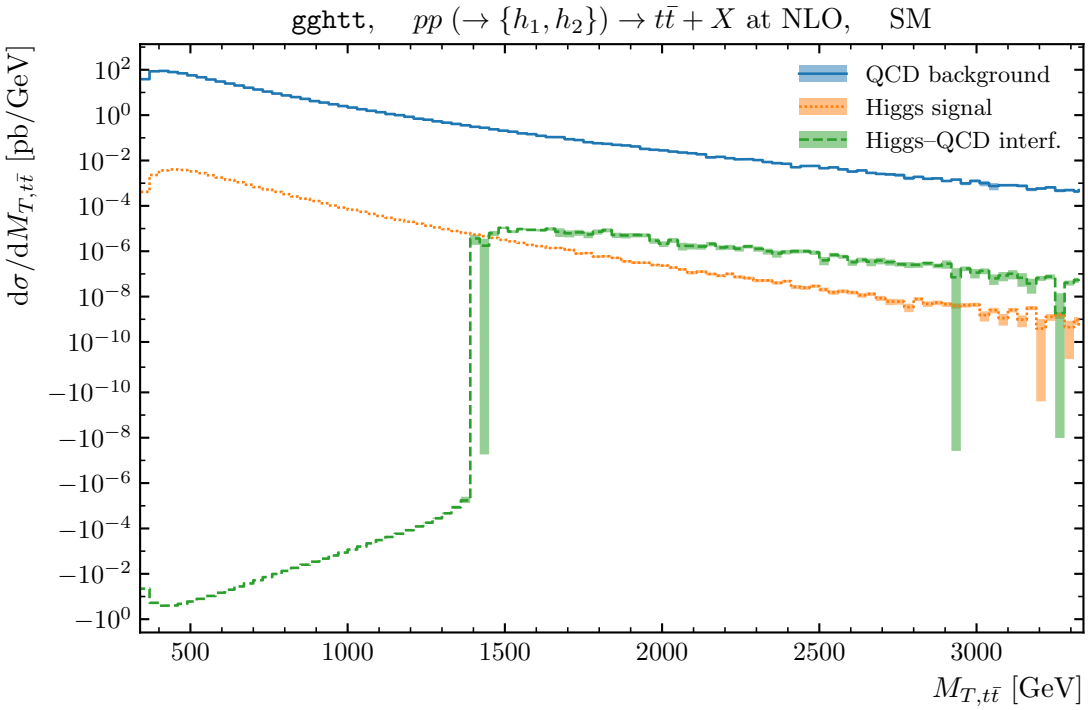

Figure B.3. The differential distributions in $M_{T,t\bar{t}}$ for the process $pp\,(\to\{h_1,h_2\})\to t\bar{t}+X$ at NLO in the SM.

C

Additional Results for the 1HSM

This appendix includes additional results for the integrated cross-sections and differential distributions for the process $pp\,(\to\{h_1,h_2\})\to t\bar{t}+X$ in the 1HSM. Details are given in chapter 6.

The integrated NLO cross-sections for the h_1 resonance signal, the h_1–QCD interference, and the h_1–h_2 interference are given in Table C.1.

$pp\,(\to\{h_1,h_2\})\to t\bar{t}+X$ in the 1HSM, pp, $\sqrt{s}=13$ TeV				
	M_{h_2} [GeV]	h_1 signal σ_{NLO} [pb]	h_1–QCD interference σ_{NLO} [pb]	h_1–h_2 interference σ_{NLO} [pb]
θ_1	700	0.028375(2)	−1.5261(2)	−0.002349(3)
	1000	0.028486(2)	−1.50471(9)	−0.001376(3)
	1500	0.029996(3)	−1.5634(2)	$-6.7(4)\times10^{-5}$
	3000	0.030686(2)	−1.5726(1)	0.000247(3)
θ_2	700	0.022579(2)	−1.3648(2)	−0.006329(3)
	1000	0.022676(2)	−1.34294(8)	−0.003343(2)
	1500	0.026972(2)	−1.4879(2)	−0.000465(3)
	3000	0.030061(3)	−1.5679(2)	−0.000289(3)

Table C.1. Integrated NLO cross-sections and corresponding K-factors for the process $pp\,(\to\{h_1,h_2\})\to t\bar{t}+X$ in the 1HSM for each benchmark point. The MC integration error is shown in brackets.

Differential distributions over the average p_T of the $t\bar{t}$ pair, $p_{T,\text{average}} = (p_{T,t} + p_{T,\bar{t}})/2$, for each 1HSM benchmark point are shown in Figure C.1 – C.8.

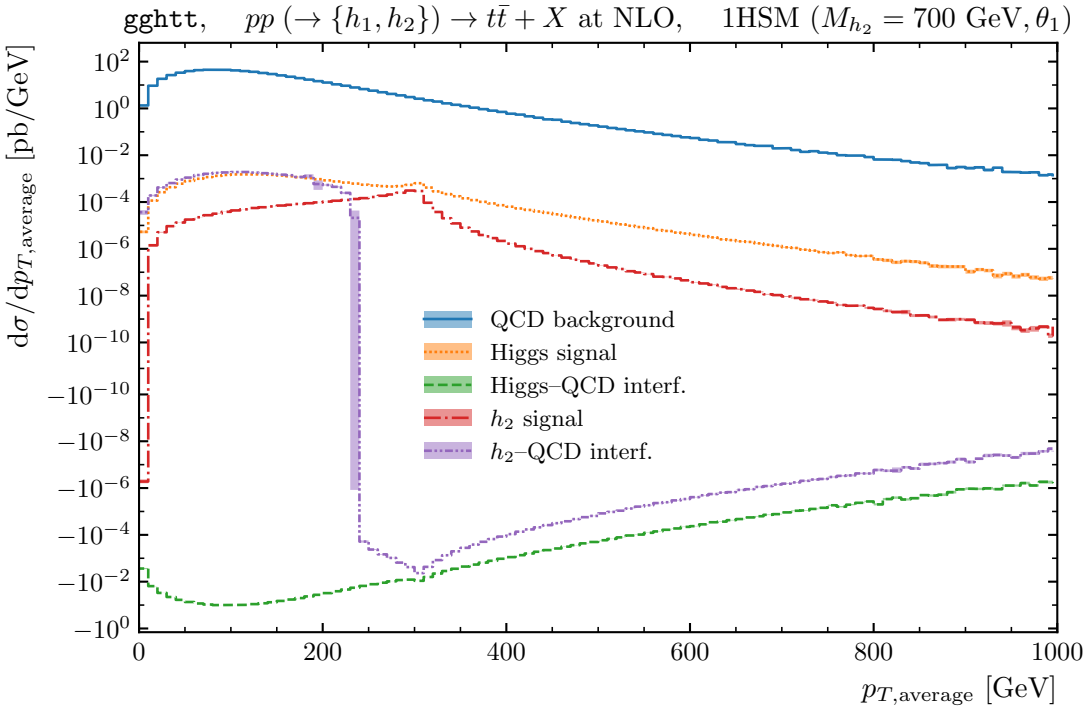

Figure C.1. The differential distributions in $p_{T,\text{average}}$ for the process $pp\,(\to\{h_1,h_2\}) \to t\bar{t}+X$ at NLO in the 1HSM extension for $M_{h_2} = 700$ GeV, $\theta = \theta_1 = \pi/15$.

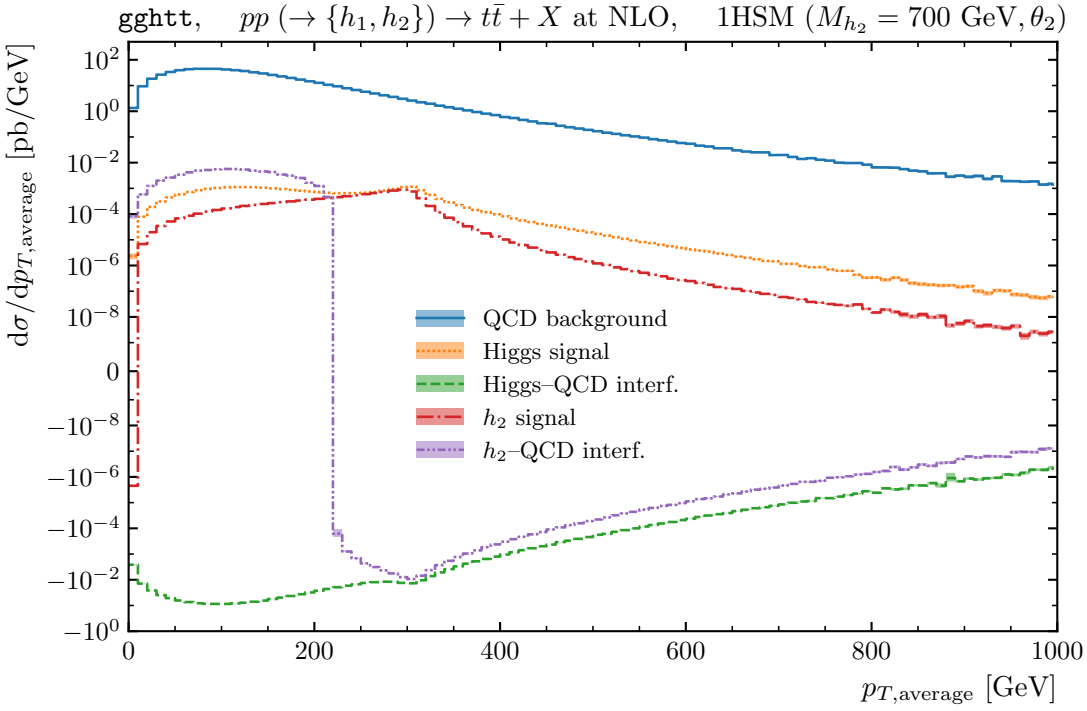

Figure C.2. The differential distributions in $p_{T,\text{average}}$ for the process $pp\,(\to\{h_1,h_2\}) \to t\bar{t}+X$ at NLO in the 1HSM extension for $M_{h_2} = 700$ GeV, $\theta = \theta_2 = \pi/8$.

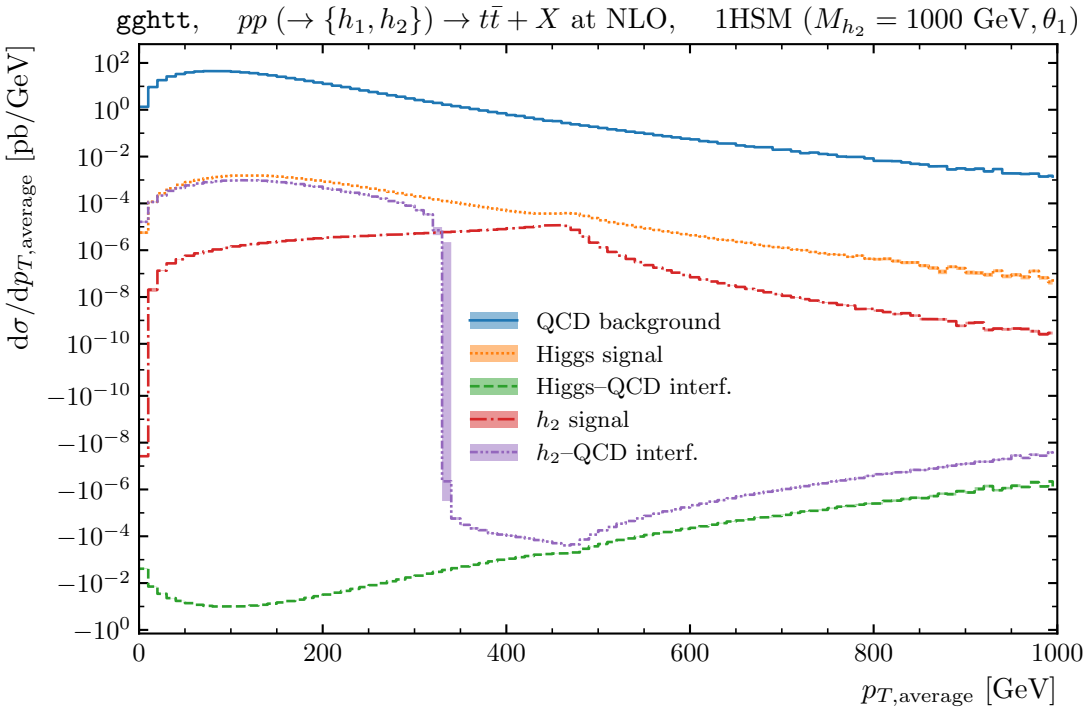

Figure C.3. The differential distributions in $p_{T,\mathrm{average}}$ for the process $pp\,(\to\{h_1,h_2\})\to t\bar{t}+X$ at NLO in the 1HSM extension for $M_{h_2}=1$ TeV, $\theta=\theta_1=\pi/15$.

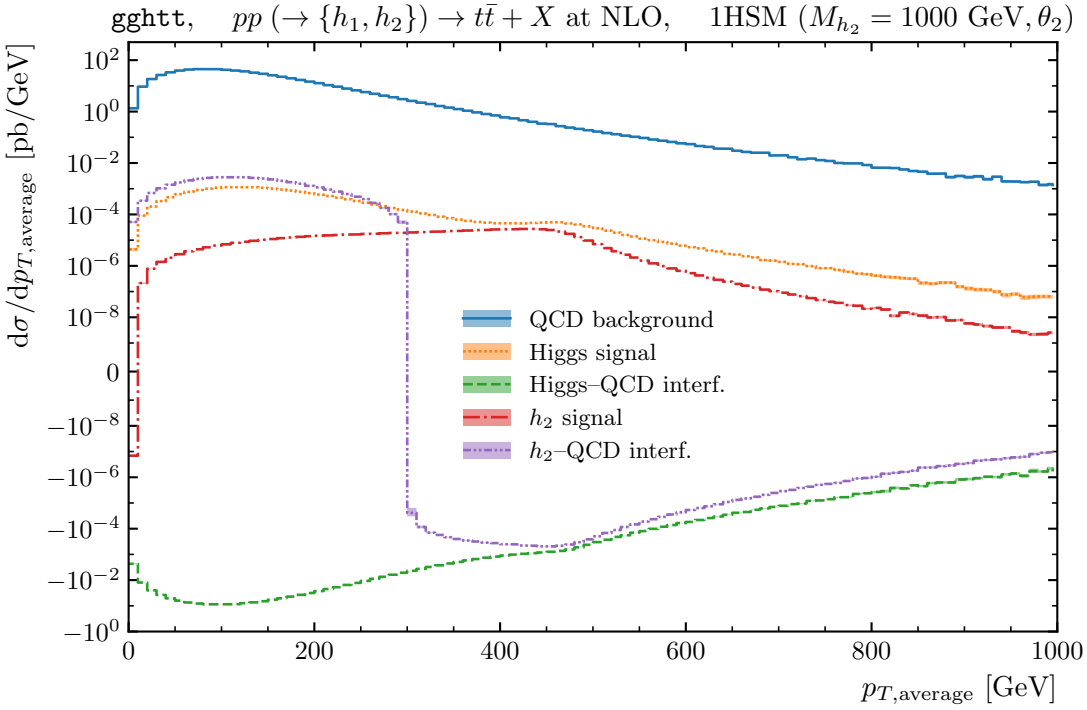

Figure C.4. The differential distributions in $p_{T,\mathrm{average}}$ for the process $pp\,(\to\{h_1,h_2\})\to t\bar{t}+X$ at NLO in the 1HSM extension for $M_{h_2}=1$ TeV, $\theta=\theta_2=\pi/8$.

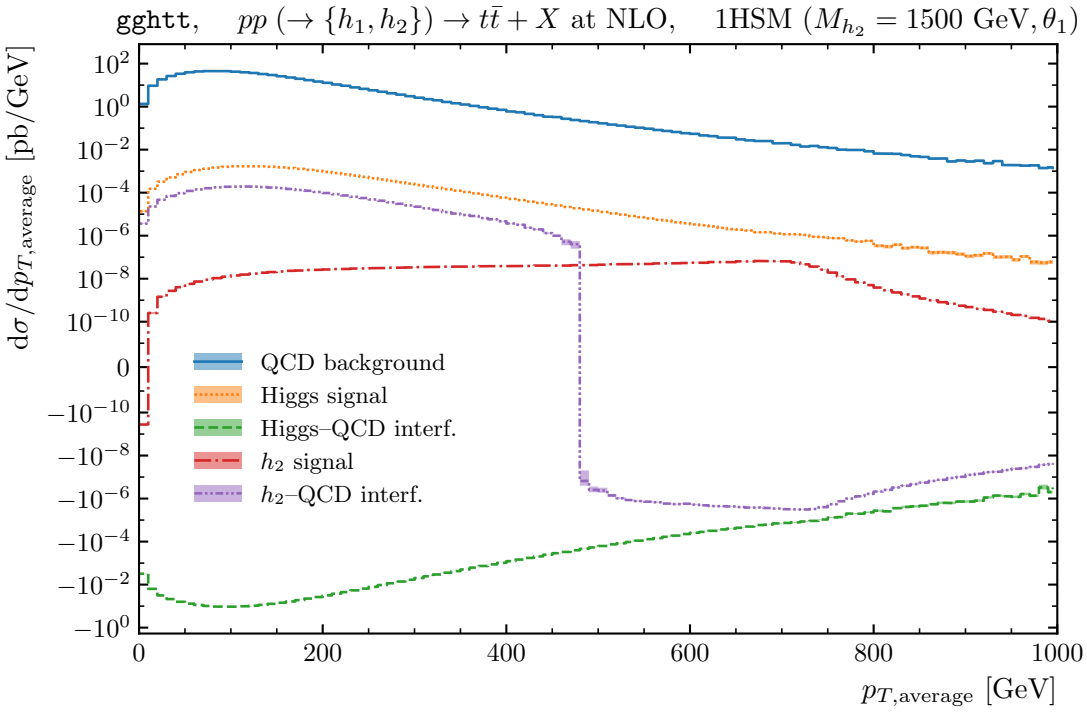

Figure C.5. The differential distributions in $p_{T,\mathrm{average}}$ for the process $pp\,(\to\{h_1,h_2\})\to t\bar{t}+X$ at NLO in the 1HSM extension for $M_{h_2}=1.5$ TeV, $\theta=\theta_1=\pi/22$.

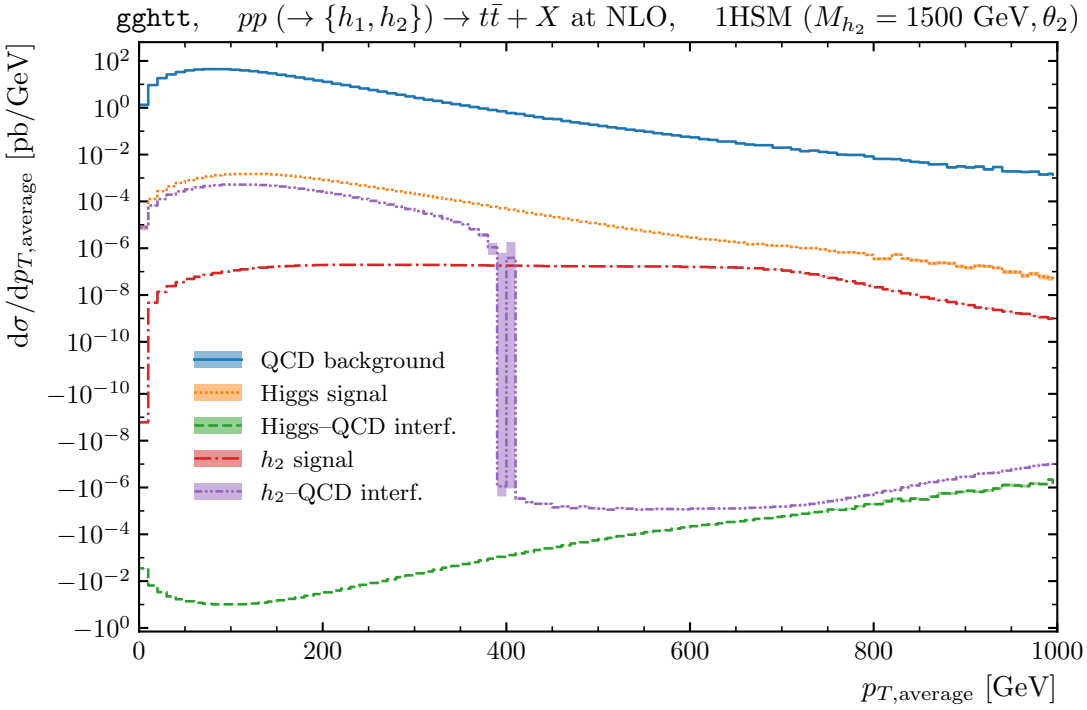

Figure C.6. The differential distributions in $p_{T,\mathrm{average}}$ for the process $pp\,(\to\{h_1,h_2\})\to t\bar{t}+X$ at NLO in the 1HSM extension for $M_{h_2}=1.5$ TeV, $\theta=\theta_2=\pi/12$.

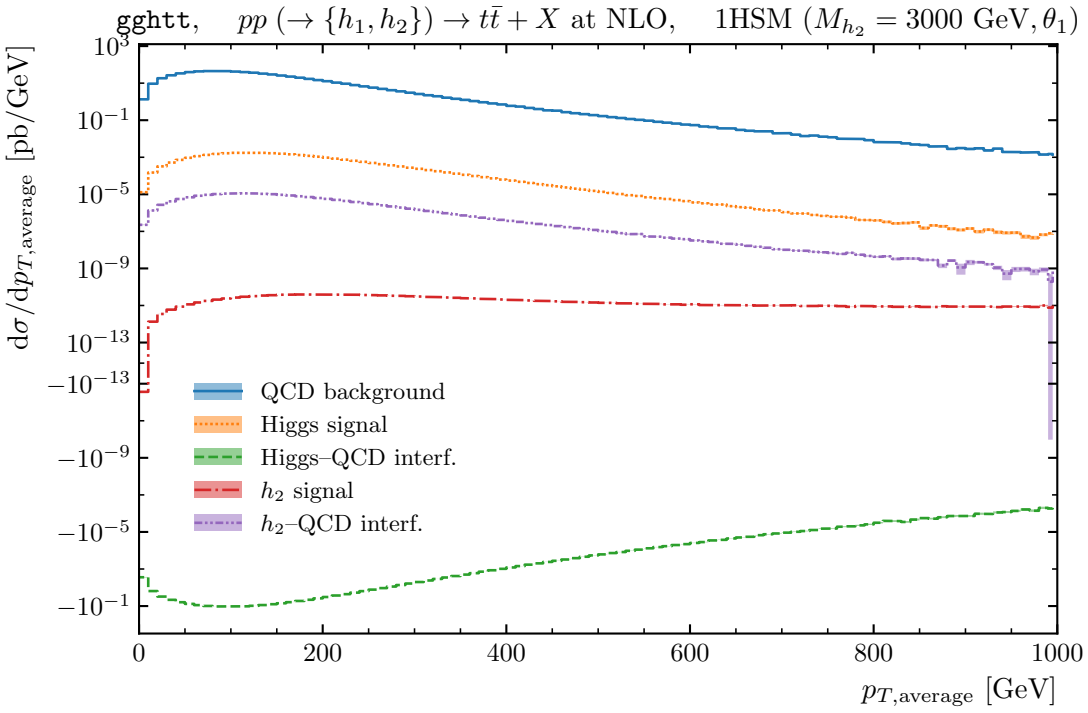

Figure C.7. The differential distributions in $p_{T,\mathrm{average}}$ for the process $pp\,(\to\{h_1,h_2\})\to t\bar{t}+X$ at NLO in the 1HSM extension for $M_{h_2}=3$ TeV, $\theta=\theta_1=\pi/45$.

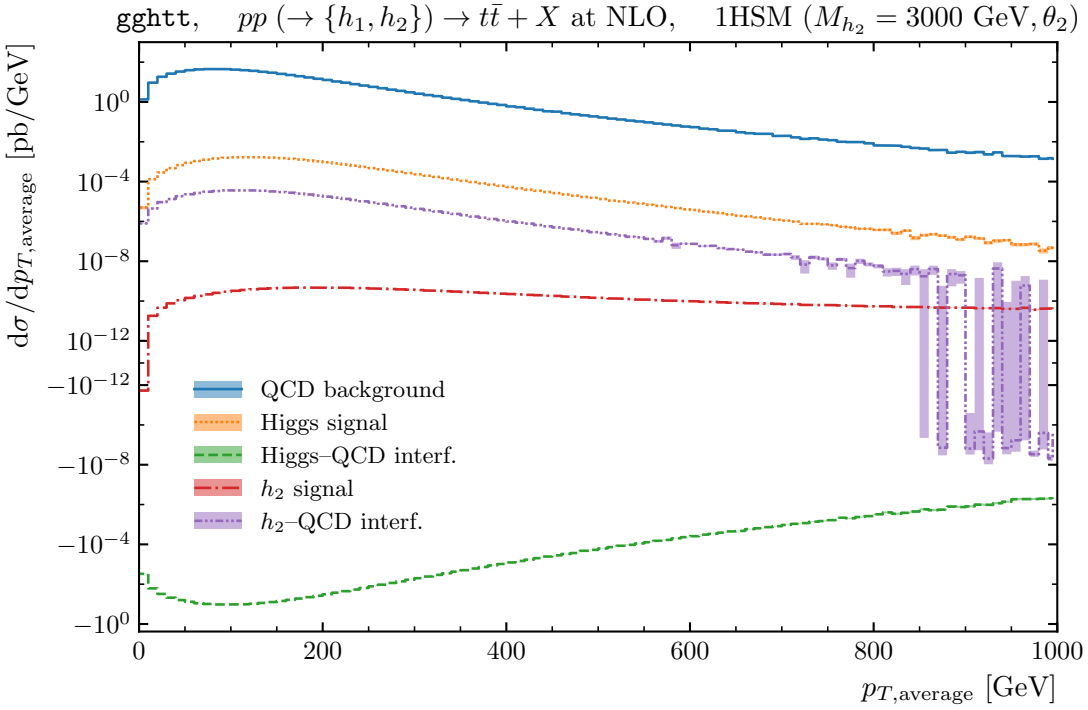

Figure C.8. The differential distributions in $p_{T,\mathrm{average}}$ for the process $pp\,(\to\{h_1,h_2\})\to t\bar{t}+X$ at NLO in the 1HSM extension for $M_{h_2}=3$ TeV, $\theta=\theta_2=\pi/24$.

Differential distributions over the transverse mass of the $t\bar{t}$ system, $M_{T,t\bar{t}}$, for each contribution in each benchmark point are shown in Figure C.9 – C.16.

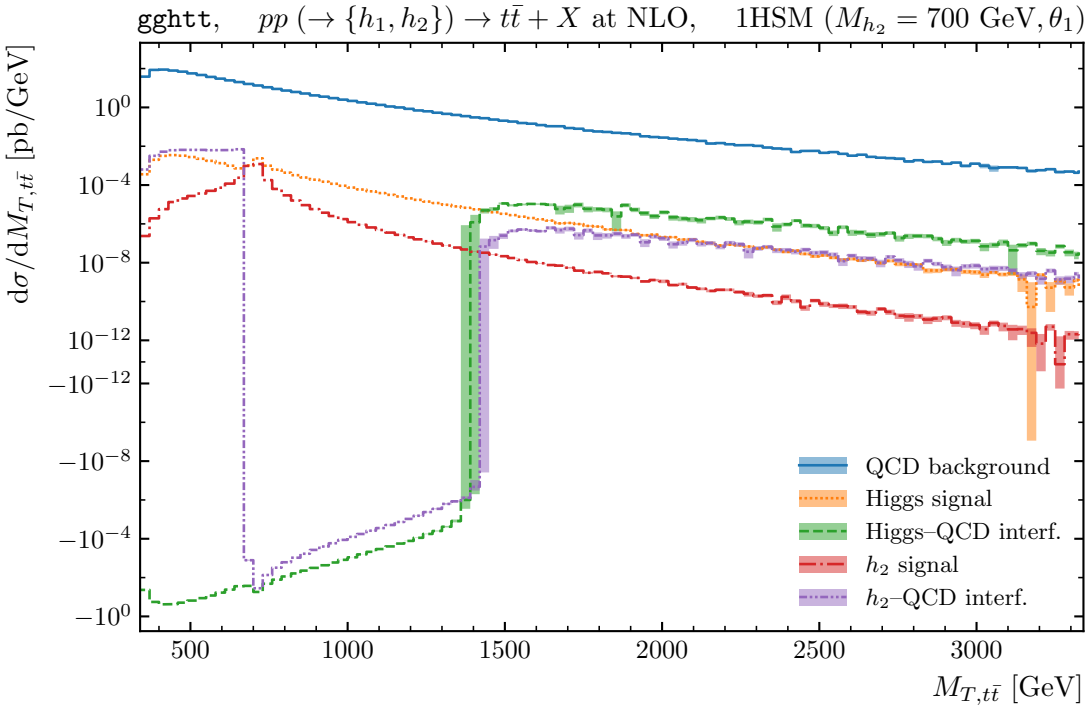

Figure C.9. The differential distributions in $M_{T,t\bar{t}}$ for the process $pp\,(\to\{h_1,h_2\})\to t\bar{t}+X$ at NLO in the 1HSM extension for $M_{h_2}=700$ GeV, $\theta=\theta_1=\pi/15$.

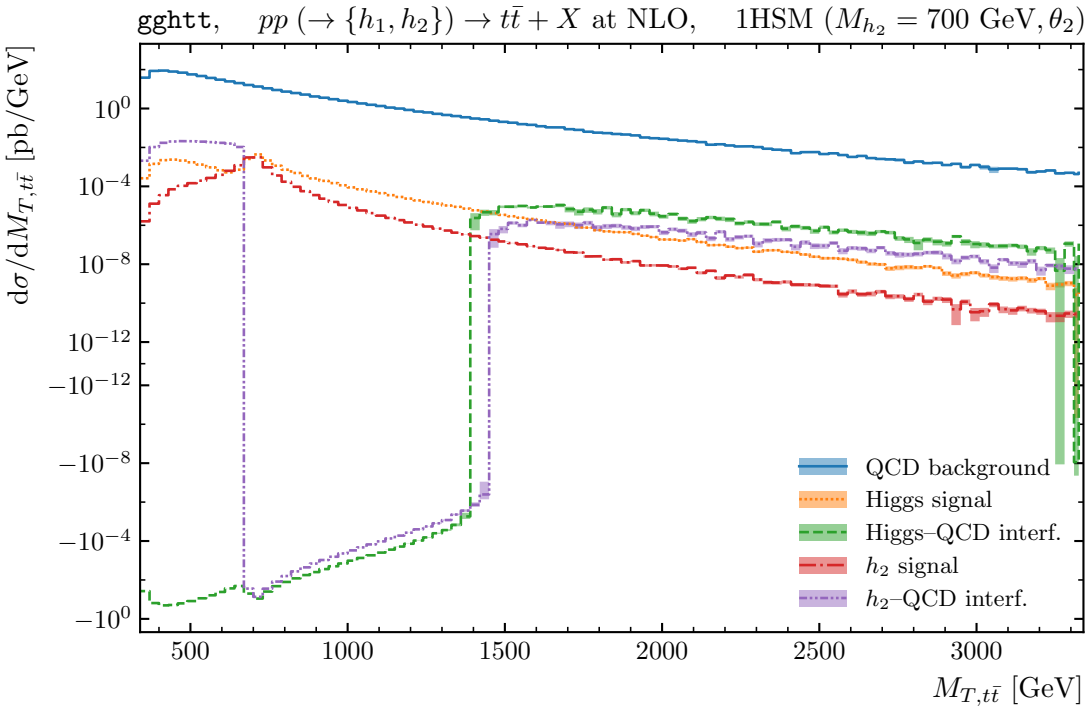

Figure C.10. The differential distributions in $M_{T,t\bar{t}}$ for the process $pp\,(\to\{h_1,h_2\})\to t\bar{t}+X$ at NLO in the 1HSM extension for $M_{h_2}=700$ GeV, $\theta=\theta_2=\pi/8$.

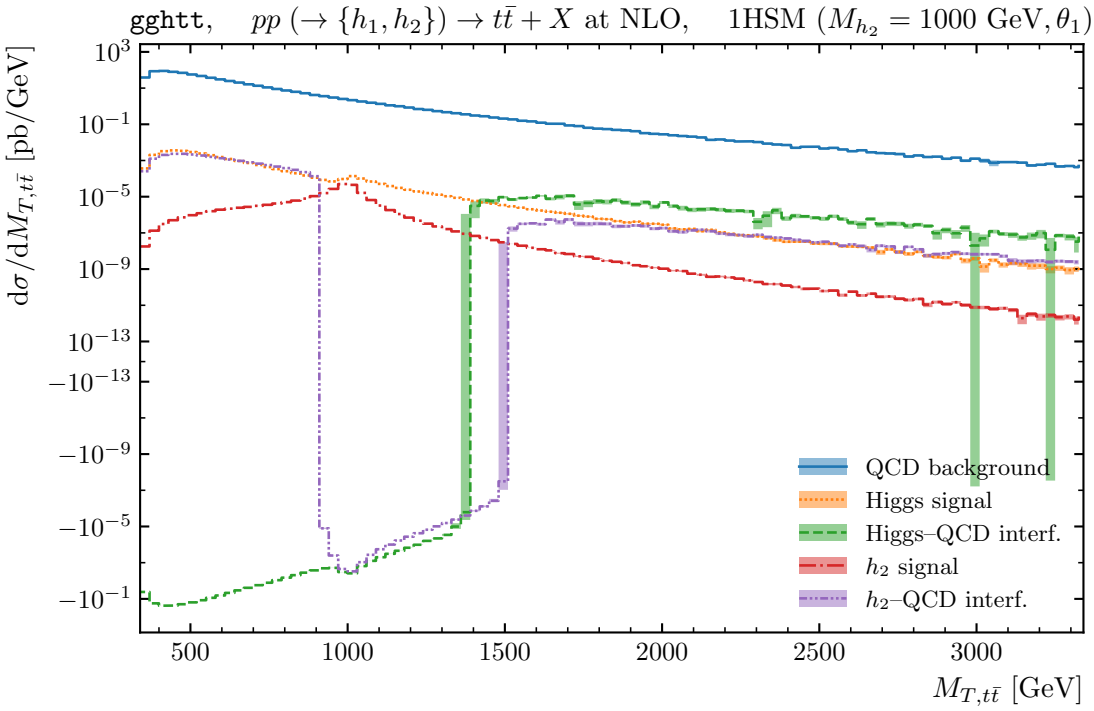

Figure C.11. The differential distributions in $M_{T,t\bar{t}}$ for the process $pp\,(\to\{h_1,h_2\})\to t\bar{t}+X$ at NLO in the 1HSM extension for $M_{h_2}=1$ TeV, $\theta=\theta_1=\pi/15$.

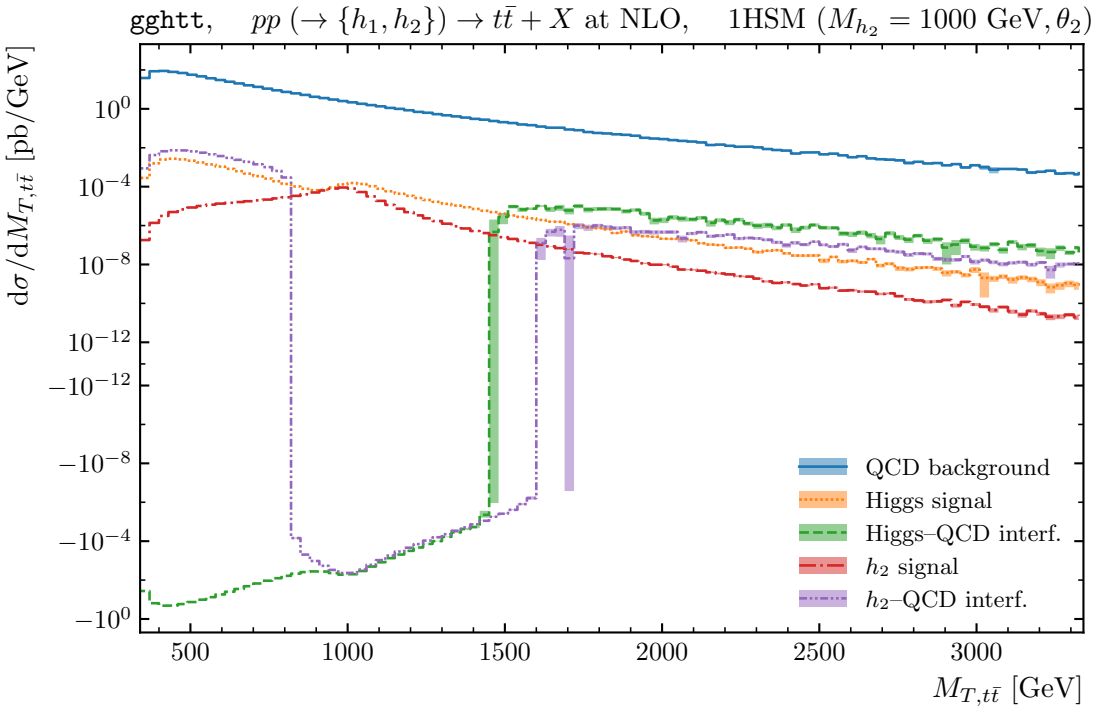

Figure C.12. The differential distributions in $M_{T,t\bar{t}}$ for the process $pp\,(\to\{h_1,h_2\})\to t\bar{t}+X$ at NLO in the 1HSM extension for $M_{h_2}=1$ TeV, $\theta=\theta_2=\pi/8$.

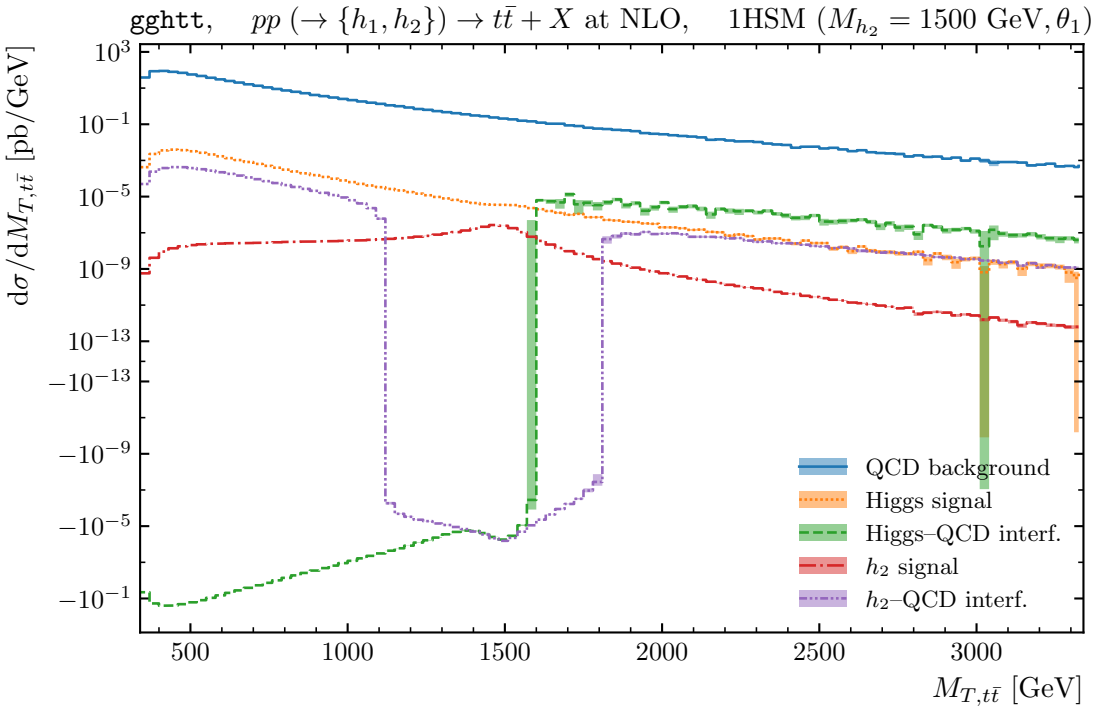

Figure C.13. The differential distributions in $M_{T,t\bar{t}}$ for the process $pp\,(\to\{h_1,h_2\})\to t\bar{t}+X$ at NLO in the 1HSM extension for $M_{h_2}=1.5$ TeV, $\theta=\theta_1=\pi/22$.

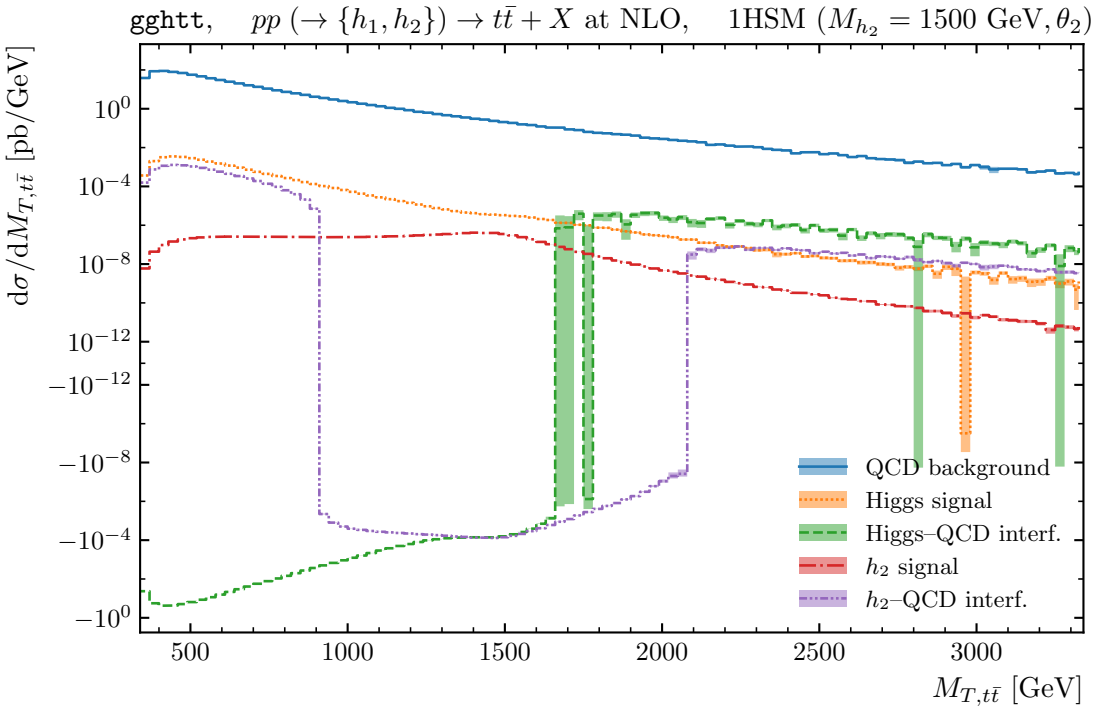

Figure C.14. The differential distributions in $M_{T,t\bar{t}}$ for the process $pp\,(\to\{h_1,h_2\})\to t\bar{t}+X$ at NLO in the 1HSM extension for $M_{h_2}=1.5$ TeV, $\theta=\theta_2=\pi/12$.

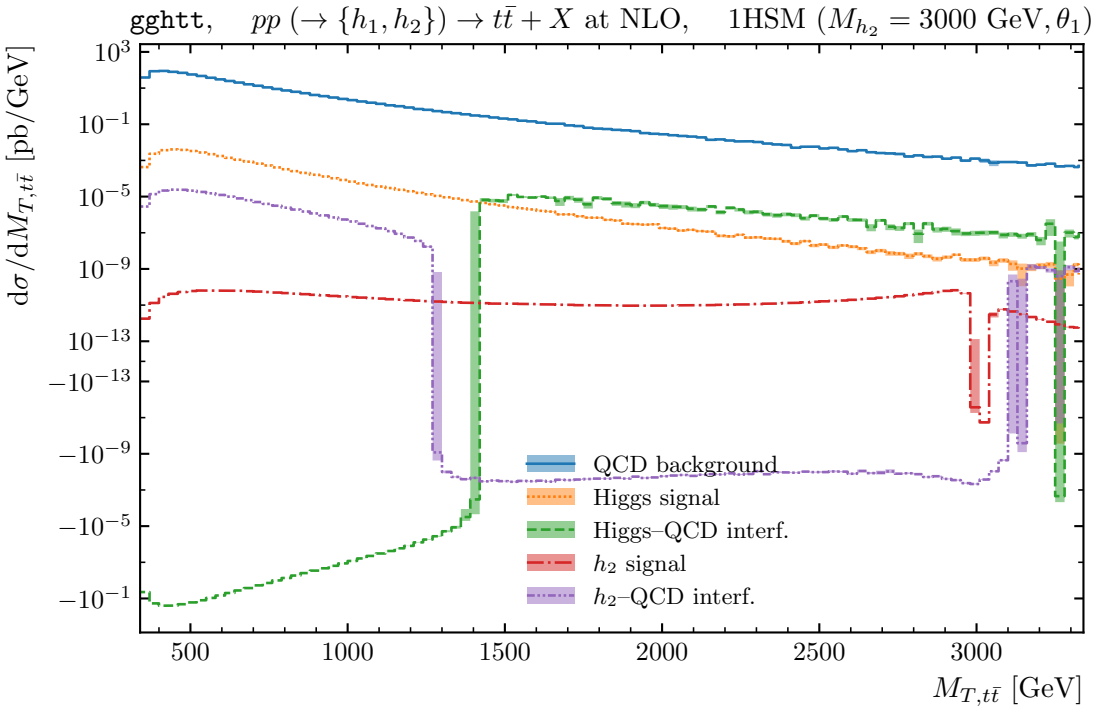

Figure C.15. The differential distributions in $M_{T,t\bar{t}}$ for the process $pp\,(\to\{h_1,h_2\})\to t\bar{t}+X$ at NLO in the 1HSM extension for $M_{h_2}=3$ TeV, $\theta=\theta_1=\pi/45$.

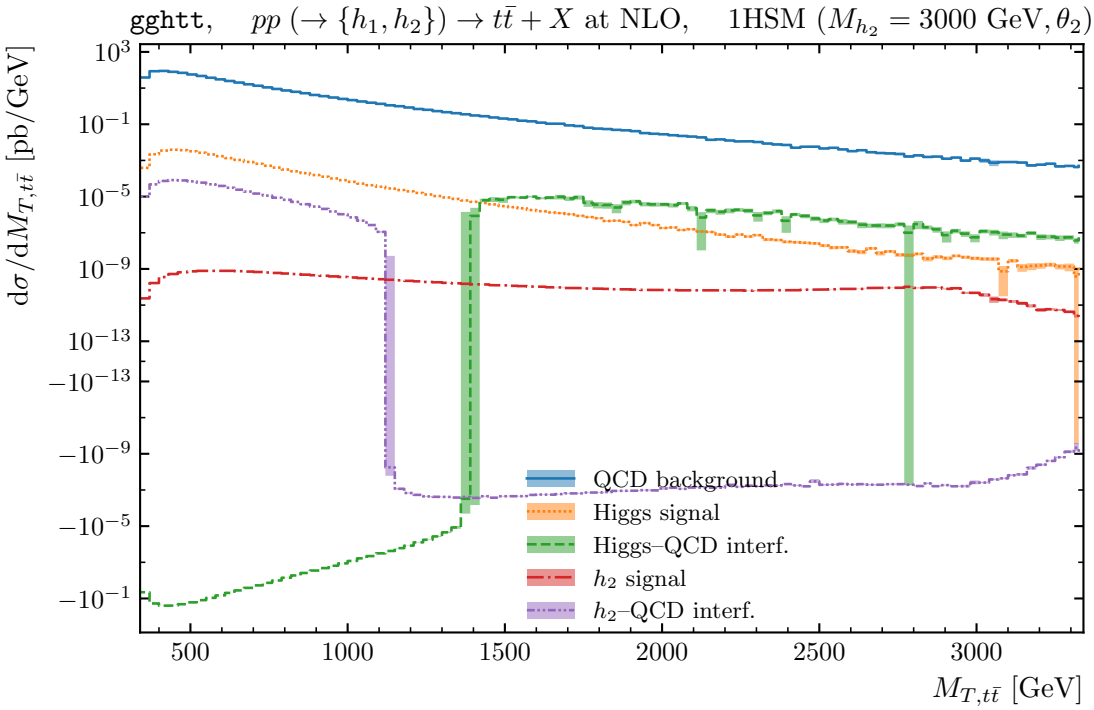

Figure C.16. The differential distributions in $M_{T,t\bar{t}}$ for the process $pp\,(\to\{h_1,h_2\})\to t\bar{t}+X$ at NLO in the 1HSM extension for $M_{h_2}=3$ TeV, $\theta=\theta_2=\pi/24$.

Bibliography

[1] F. J. Dyson, *From Eros to Gaia*. 1992.

[2] P. W. Anderson, "More Is Different," *Science* **177** no. 4047, (1972) 393–396. https://science.sciencemag.org/content/177/4047/393.

[3] C. Vafa, "The String landscape and the swampland," arXiv:hep-th/0509212.

[4] **ATLAS** Collaboration, G. Aad *et al.*, "Observation of a new particle in the search for the Standard Model Higgs boson with the ATLAS detector at the LHC," *Phys. Lett. B* **716** (2012) 1–29, arXiv:1207.7214 [hep-ex].

[5] **CMS** Collaboration, S. Chatrchyan *et al.*, "Observation of a New Boson at a Mass of 125 GeV with the CMS Experiment at the LHC," *Phys. Lett. B* **716** (2012) 30–61, arXiv:1207.7235 [hep-ex].

[6] P. Higgs, "Broken symmetries, massless particles and gauge fields," *Physics Letters* **12** no. 2, (1964) 132–133. https://www.sciencedirect.com/science/article/pii/0031916364911369.

[7] P. W. Higgs, "Broken Symmetries and the Masses of Gauge Bosons," *Phys. Rev. Lett.* **13** (Oct, 1964) 508–509. https://link.aps.org/doi/10.1103/PhysRevLett.13.508.

[8] P. W. Higgs, "Spontaneous Symmetry Breakdown without Massless Bosons," *Phys. Rev.* **145** (May, 1966) 1156–1163. https://link.aps.org/doi/10.1103/PhysRev.145.1156.

[9] F. Englert and R. Brout, "Broken Symmetry and the Mass of Gauge Vector Mesons," *Phys. Rev. Lett.* **13** (Aug, 1964) 321–323. https://link.aps.org/doi/10.1103/PhysRevLett.13.321.

[10] G. S. Guralnik, C. R. Hagen, and T. W. B. Kibble, "Global Conservation Laws and Massless Particles," *Phys. Rev. Lett.* **13** (Nov, 1964) 585–587. https://link.aps.org/doi/10.1103/PhysRevLett.13.585.

[11] J. Campbell, J. Huston, and F. Krauss, *The Black Book of Quantum Chromodynamics: A Primer for the LHC Era*. Oxford University Press, 12, 2017.

[12] M. Thomson, *Modern particle physics*. Cambridge University Press, New York, 2013.

[13] L. D. Faddeev and V. N. Popov, "Feynman Diagrams for the Yang-Mills Field," *Phys. Lett. B* **25** (1967) 29–30.

[14] R. P. Feynman, "The Theory of positrons," *Phys. Rev.* **76** (1949) 749–759.

[15] T. Tantau, *The TikZ and PGF Packages*. https://github.com/pgf-tikz/pgf.

[16] T. Ohl, "Drawing Feynman diagrams with Latex and Metafont," *Comput. Phys. Commun.* **90** (1995) 340–354, arXiv:hep-ph/9505351. https://www.ctan.org/pkg/feynmf.

[17] D. Binosi and L. Theussl, "JaxoDraw: A Graphical user interface for drawing Feynman diagrams," *Comput. Phys. Commun.* **161** (2004) 76–86, arXiv:hep-ph/0309015.

[18] A. V. Manohar, "Introduction to Effective Field Theories," arXiv:1804.05863 [hep-ph].

[19] J. R. Ellis, M. K. Gaillard, and D. V. Nanopoulos, "A Phenomenological Profile of the Higgs Boson," *Nucl. Phys. B* **106** (1976) 292.

[20] B. A. Kniehl and M. Spira, "Low-energy theorems in Higgs physics," *Z. Phys. C* **69** (1995) 77–88, arXiv:hep-ph/9505225.

[21] R. K. Ellis, W. J. Stirling, and B. R. Webber, *QCD and collider physics*, vol. 8. Cambridge University Press, 2, 2011.

[22] M. E. Peskin and D. V. Schroeder, *An Introduction to quantum field theory*. Addison-Wesley, Reading, USA, 1995.

[23] J. D. Hunter, "Matplotlib: A 2D graphics environment," *Computing in Science & Engineering* **9** no. 3, (2007) 90–95.

[24] L. J. Dixon and M. S. Siu, "Resonance continuum interference in the diphoton Higgs signal at the LHC," *Phys. Rev. Lett.* **90** (2003) 252001, arXiv:hep-ph/0302233.

[25] L. J. Dixon and Y. Li, "Bounding the Higgs Boson Width Through Interferometry," *Phys. Rev. Lett.* **111** (2013) 111802, arXiv:1305.3854 [hep-ph].

[26] E. W. N. Glover and J. J. van der Bij, "VECTOR BOSON PAIR PRODUCTION VIA GLUON FUSION," *Phys. Lett. B* **219** (1989) 488–492.

[27] E. W. N. Glover and J. J. van der Bij, "Z BOSON PAIR PRODUCTION VIA GLUON FUSION," *Nucl. Phys. B* **321** (1989) 561–590.

[28] G. Passarino, "Higgs Interference Effects in $gg \to ZZ$ and their Uncertainty," *JHEP* **08** (2012) 146, arXiv:1206.3824 [hep-ph].

[29] J. M. Campbell, R. K. Ellis, E. Furlan, and R. Röntsch, "Interference effects for Higgs boson mediated Z-pair plus jet production," *Phys. Rev. D* **90** no. 9, (2014) 093008, arXiv:1409.1897 [hep-ph].

[30] J. M. Campbell, R. K. Ellis, and C. Williams, "Gluon-Gluon Contributions to W+ W- Production and Higgs Interference Effects," *JHEP* **10** (2011) 005, arXiv:1107.5569 [hep-ph].

[31] M. Bonvini, F. Caola, S. Forte, K. Melnikov, and G. Ridolfi, "Signal-background interference effects for ggßHßW^+W^- beyond leading order," *Phys. Rev. D* **88** no. 3, (2013) 034032, arXiv:1304.3053 [hep-ph].

[32] N. Kauer, "Signal-background interference in gg -> H -> VV," *PoS* **RADCOR2011** (2011) 027, arXiv:1201.1667 [hep-ph].

[33] C. G. Bollini and J. J. Giambiagi, "Dimensional Renormalization: The Number of Dimensions as a Regularizing Parameter," *Nuovo Cim. B* **12** (1972) 20–26.

[34] G. 't Hooft and M. J. G. Veltman, "Regularization and Renormalization of Gauge Fields," *Nucl. Phys. B* **44** (1972) 189–213.

[35] G. Passarino and M. J. G. Veltman, "One Loop Corrections for e+ e- Annihilation Into mu+ mu- in the Weinberg Model," *Nucl. Phys. B* **160** (1979) 151–207.

[36] G. Ossola, C. G. Papadopoulos, and R. Pittau, "Reducing full one-loop amplitudes to scalar integrals at the integrand level," *Nucl. Phys. B* **763** (2007) 147–169, arXiv:hep-ph/0609007.

[37] G. Ossola, C. G. Papadopoulos, and R. Pittau, "CutTools: A Program implementing the OPP reduction method to compute one-loop amplitudes," *JHEP* **03** (2008) 042, arXiv:0711.3596 [hep-ph].

[38] G. Kallen and J. S. Toll, "Momentum Space Analyticity Properties of the Bergman-Weil Integral for the Three Point Function," *J. Math. Phys.* **6** (1965) 1885–1901.

[39] Z. Bern, L. J. Dixon, D. C. Dunbar, and D. A. Kosower, "Fusing gauge theory tree amplitudes into loop amplitudes," *Nucl. Phys. B* **435** (1995) 59–101, arXiv:hep-ph/9409265.

[40] Z. Bern, L. J. Dixon, D. C. Dunbar, and D. A. Kosower, "One loop n point gauge theory amplitudes, unitarity and collinear limits," *Nucl. Phys. B* **425** (1994) 217–260, arXiv:hep-ph/9403226.

[41] Z. Bern, L. J. Dixon, and D. A. Kosower, "On-Shell Methods in Perturbative QCD," *Annals Phys.* **322** (2007) 1587–1634, arXiv:0704.2798 [hep-ph].

[42] F. Cascioli, P. Maierhofer, and S. Pozzorini, "Scattering Amplitudes with Open Loops," *Phys. Rev. Lett.* **108** (2012) 111601, arXiv:1111.5206 [hep-ph].

[43] F. Buccioni, S. Pozzorini, and M. Zoller, "On-the-fly reduction of open loops," *Eur. Phys. J. C* **78** no. 1, (2018) 70, arXiv:1710.11452 [hep-ph].

[44] S. Kallweit, J. M. Lindert, P. Maierhöfer, S. Pozzorini, and M. Schönherr, "NLO electroweak automation and precise predictions for W+multijet production at the LHC," *JHEP* **04** (2015) 012, arXiv:1412.5157 [hep-ph].

[45] F. Buccioni, J.-N. Lang, J. M. Lindert, P. Maierhöfer, S. Pozzorini, H. Zhang, and M. F. Zoller, "OpenLoops 2," *Eur. Phys. J. C* **79** no. 10, (2019) 866, arXiv:1907.13071 [hep-ph].

[46] F. del Aguila and R. Pittau, "Recursive numerical calculus of one-loop tensor integrals," *JHEP* **07** (2004) 017, arXiv:hep-ph/0404120.

[47] J. Alwall, R. Frederix, S. Frixione, V. Hirschi, F. Maltoni, O. Mattelaer, H. S. Shao, T. Stelzer, P. Torrielli, and M. Zaro, "The automated computation of tree-level and next-to-leading order differential cross sections, and their matching to parton shower simulations," *JHEP* **07** (2014) 079, arXiv:1405.0301 [hep-ph]. https://launchpad.net/mg5amcnlo.

[48] J. Davies, F. Herren, and M. Steinhauser, "Top Quark Mass Effects in Higgs Boson Production at Four-Loop Order: Virtual Corrections," *Phys. Rev. Lett.* **124** no. 11, (2020) 112002, arXiv:1911.10214 [hep-ph].

[49] F. Bloch and A. Nordsieck, "Note on the Radiation Field of the electron," *Phys. Rev.* **52** (1937) 54–59.

[50] T. Kinoshita, "Mass singularities of Feynman amplitudes," *J. Math. Phys.* **3** (1962) 650–677.

[51] T. D. Lee and M. Nauenberg, "Degenerate Systems and Mass Singularities," *Phys. Rev.* **133** (1964) B1549–B1562.

[52] S. Frixione, Z. Kunszt, and A. Signer, "Three jet cross-sections to next-to-leading order," *Nucl. Phys. B* **467** (1996) 399–442, arXiv:hep-ph/9512328.

[53] S. Frixione, "A General approach to jet cross-sections in QCD," *Nucl. Phys. B* **507** (1997) 295–314, arXiv:hep-ph/9706545.

[54] Z. Nagy and D. E. Soper, "General subtraction method for numerical calculation of one loop QCD matrix elements," *JHEP* **09** (2003) 055, arXiv:hep-ph/0308127.

[55] S. Catani and M. H. Seymour, "A General algorithm for calculating jet cross-sections in NLO QCD," *Nucl. Phys. B* **485** (1997) 291–419, arXiv:hep-ph/9605323. [Erratum: Nucl.Phys.B 510, 503–504 (1998)].

[56] S. Catani, S. Dittmaier, M. H. Seymour, and Z. Trocsanyi, "The Dipole formalism for next-to-leading order QCD calculations with massive partons," *Nucl. Phys. B* **627** (2002) 189–265, arXiv:hep-ph/0201036.

[57] S. Catani and M. Grazzini, "An NNLO subtraction formalism in hadron collisions and its application to Higgs boson production at the LHC," *Phys. Rev. Lett.* **98** (2007) 222002, arXiv:hep-ph/0703012.

[58] A. Gehrmann-De Ridder, T. Gehrmann, and E. W. N. Glover, "Antenna subtraction at NNLO," *JHEP* **09** (2005) 056, arXiv:hep-ph/0505111.

[59] C. Anastasiou, C. Duhr, F. Dulat, F. Herzog, and B. Mistlberger, "Higgs Boson Gluon-Fusion Production in QCD at Three Loops," *Phys. Rev. Lett.* **114** (2015) 212001, arXiv:1503.06056 [hep-ph].

[60] A. Buckley *et al.*, "General-purpose event generators for LHC physics," *Phys. Rept.* **504** (2011) 145–233, arXiv:1101.2599 [hep-ph].

[61] P. Skands, "Introduction to QCD," in *Theoretical Advanced Study Institute in Elementary Particle Physics: Searching for New Physics at Small and Large Scales*. 7, 2012. arXiv:1207.2389 [hep-ph].

[62] D. R. Green, *High P(T) physics at hadron colliders*, vol. 22. 2005.

[63] T. Gleisberg, S. Hoeche, F. Krauss, M. Schonherr, S. Schumann, F. Siegert, and J. Winter, "Event generation with SHERPA 1.1" *JHEP* **02** (2009) 007, arXiv:0811.4622 [hep-ph].

[64] T. Sjöstrand, S. Ask, J. R. Christiansen, R. Corke, N. Desai, P. Ilten, S. Mrenna, S. Prestel, C. O. Rasmussen, and P. Z. Skands, "An introduction to PYTHIA 8.2" *Comput. Phys. Commun.* **191** (2015) 159–177, arXiv:1410.3012 [hep-ph].

[65] M. Bahr *et al.*, "Herwig++ Physics and Manual," *Eur. Phys. J. C* **58** (2008) 639–707, arXiv:0803.0883 [hep-ph].

[66] A. Buckley, J. Ferrando, S. Lloyd, K. Nordström, B. Page, M. Rüfenacht, M. Schönherr, and G. Watt, "LHAPDF6: parton density access in the LHC precision era," *Eur. Phys. J. C* **75** (2015) 132, arXiv:1412.7420 [hep-ph]. https://lhapdf.hepforge.org/.

[67] G. P. Salam and J. Rojo, "A Higher Order Perturbative Parton Evolution Toolkit (HOPPET)," *Comput. Phys. Commun.* **180** (2009) 120–156, arXiv:0804.3755 [hep-ph]. https://hoppet.hepforge.org/.

[68] T. Gleisberg and S. Hoeche, "Comix, a new matrix element generator," *JHEP* **12** (2008) 039, arXiv:0808.3674 [hep-ph].

[69] A. Djouadi, J. Kalinowski, and M. Spira, "HDECAY: A Program for Higgs boson decays in the standard model and its supersymmetric extension," *Comput. Phys. Commun.* **108** (1998) 56–74, arXiv:hep-ph/9704448.

[70] A. Djouadi, J. Kalinowski, M. Muehlleitner, and M. Spira, "HDECAY: Twenty$_{++}$ years after," *Comput. Phys. Commun.* **238** (2019) 214–231, arXiv:1801.09506 [hep-ph].

[71] A. Bredenstein, A. Denner, S. Dittmaier, and M. M. Weber, "Precise predictions for the Higgs-boson decay H —> WW/ZZ —> 4 leptons," *Phys. Rev. D* **74** (2006) 013004, arXiv:hep-ph/0604011.

[72] A. Bredenstein, A. Denner, S. Dittmaier, and M. M. Weber, "Precision calculations for the Higgs decays H —> ZZ/WW —> 4 leptons," *Nucl. Phys. B Proc. Suppl.* **160** (2006) 131–135, arXiv:hep-ph/0607060.

[73] A. Bredenstein, A. Denner, S. Dittmaier, and M. M. Weber, "Radiative corrections to the semileptonic and hadronic Higgs-boson decays H —> W W / Z Z —> 4 fermions," *JHEP* **02** (2007) 080, arXiv:hep-ph/0611234.

[74] S. Höche and S. Prestel, "The midpoint between dipole and parton showers," *Eur. Phys. J. C* **75** no. 9, (2015) 461, arXiv:1506.05057 [hep-ph].

[75] N. Fischer, S. Prestel, M. Ritzmann, and P. Skands, "Vincia for Hadron Colliders," *Eur. Phys. J. C* **76** no. 11, (2016) 589, arXiv:1605.06142 [hep-ph].

[76] J. M. Campbell and R. K. Ellis, "An Update on vector boson pair production at hadron colliders," *Phys. Rev. D* **60** (1999) 113006, arXiv:hep-ph/9905386.

[77] J. M. Campbell, R. K. Ellis, and C. Williams, "Vector boson pair production at the LHC," *JHEP* **07** (2011) 018, arXiv:1105.0020 [hep-ph].

[78] J. M. Campbell, R. K. Ellis, and W. T. Giele, "A Multi-Threaded Version of MCFM," *Eur. Phys. J. C* **75** no. 6, (2015) 246, arXiv:1503.06182 [physics.comp-ph].

[79] J. Campbell and T. Neumann, "Precision Phenomenology with MCFM," *JHEP* **12** (2019) 034, arXiv:1909.09117 [hep-ph].

[80] P. Nason, "A New method for combining NLO QCD with shower Monte Carlo algorithms," *JHEP* **11** (2004) 040, arXiv:hep-ph/0409146.

[81] S. Frixione, P. Nason, and C. Oleari, "Matching NLO QCD computations with Parton Shower simulations: the POWHEG method," *JHEP* **11** (2007) 070, arXiv:0709.2092 [hep-ph].

[82] S. Alioli, P. Nason, C. Oleari, and E. Re, "A general framework for implementing NLO calculations in shower Monte Carlo programs: the POWHEG BOX," *JHEP* **06** (2010) 043, arXiv:1002.2581 [hep-ph].

[83] V. N. Gribov and L. N. Lipatov, "Deep inelastic e p scattering in perturbation theory," *Sov. J. Nucl. Phys.* **15** (1972) 438–450.

[84] G. Altarelli and G. Parisi, "Asymptotic Freedom in Parton Language," *Nucl. Phys. B* **126** (1977) 298–318.

[85] Y. L. Dokshitzer, "Calculation of the Structure Functions for Deep Inelastic Scattering and e+ e- Annihilation by Perturbation Theory in Quantum Chromodynamics.," *Sov. Phys. JETP* **46** (1977) 641–653.

[86] J. Pumplin, D. Stump, R. Brock, D. Casey, J. Huston, J. Kalk, H. L. Lai, and W. K. Tung, "Uncertainties of predictions from parton distribution functions. 2. The Hessian method," *Phys. Rev. D* **65** (2001) 014013, arXiv:hep-ph/0101032.

[87] **NNPDF** Collaboration, R. D. Ball *et al.*, "Parton distributions for the LHC Run II," *JHEP* **04** (2015) 040, arXiv:1410.8849 [hep-ph].

[88] M. H. Seymour, *Predictions for Higgs and Electroweak Boson Production.* PhD thesis, Churchill College, University of Cambridge, 10, 1992. http://www.hep.manchester.ac.uk/u/seymour/thesis/.

[89] A. Papaefstathiou, "How-to: write a parton-level Monte Carlo particle physics event generator," *Eur. Phys. J. Plus* **135** no. 6, (2020) 497, arXiv:1412.4677 [hep-ph].

[90] M. Dobbs and J. B. Hansen, "The HepMC C++ Monte Carlo event record for High Energy Physics," *Comput. Phys. Commun.* **134** (2001) 41–46.

[91] A. Buckley, P. Ilten, D. Konstantinov, L. Lönnblad, J. Monk, W. Pokorski, T. Przedzinski, and A. Verbytskyi, "The HepMC3 event record library for Monte Carlo event generators," *Comput. Phys. Commun.* **260** (2021) 107310, arXiv:1912.08005 [hep-ph].

[92] J. Alwall *et al.*, "A Standard format for Les Houches event files," *Comput. Phys. Commun.* **176** (2007) 300–304, arXiv:hep-ph/0609017.

[93] G. P. Lepage, "VEGAS: AN ADAPTIVE MULTIDIMENSIONAL INTEGRATION PROGRAM,".

[94] G. P. Lepage, "Adaptive multidimensional integration: VEGAS enhanced," *J. Comput. Phys.* **439** (2021) 110386, arXiv:2009.05112 [physics.comp-ph].

[95] A. Lind and A. Banfi, "H1jet, a fast program to compute transverse momentum distributions," *Eur. Phys. J. C* **81** no. 1, (2021) 72, arXiv:2011.04694 [hep-ph].

[96] H1JET is available at https://h1jet.hepforge.org/ and https://github.com/alexander-lind/H1jet.

[97] C. Grojean, E. Salvioni, M. Schlaffer, and A. Weiler, "Very boosted Higgs in gluon fusion," *JHEP* **05** (2014) 022, arXiv:1312.3317 [hep-ph].

[98] A. Azatov and A. Paul, "Probing Higgs couplings with high p_T Higgs production," *JHEP* **01** (2014) 014, arXiv:1309.5273 [hep-ph].

[99] **ATLAS** Collaboration, G. Aad *et al.*, "CP Properties of Higgs Boson Interactions with Top Quarks in the $t\bar{t}H$ and tH Processes Using $H \to \gamma\gamma$ with the ATLAS Detector," *Phys. Rev. Lett.* **125** no. 6, (2020) 061802, arXiv:2004.04545 [hep-ex].

[100] **CMS** Collaboration, A. M. Sirunyan *et al.*, "Measurements of $\mathrm{t\bar{t}}H$ Production and the CP Structure of the Yukawa Interaction between the Higgs Boson and Top Quark in the Diphoton Decay Channel," *Phys. Rev. Lett.* **125** no. 6, (2020) 061801, arXiv:2003.10866 [hep-ex].

[101] F. Maltoni, E. Vryonidou, and C. Zhang, "Higgs production in association with a top-antitop pair in the Standard Model Effective Field Theory at NLO in QCD," *JHEP* **10** (2016) 123, arXiv:1607.05330 [hep-ph].

[102] A. Banfi, A. Martin, and V. Sanz, "Probing top-partners in Higgs+jets," *JHEP* **08** (2014) 053, arXiv:1308.4771 [hep-ph].

[103] **CMS** Collaboration, A. M. Sirunyan *et al.*, "Search for dark matter produced with an energetic jet or a hadronically decaying W or Z boson at $\sqrt{s} = 13$ TeV," *JHEP* **07** (2017) 014, arXiv:1703.01651 [hep-ex].

[104] **ATLAS** Collaboration, M. Aaboud *et al.*, "Constraints on mediator-based dark matter and scalar dark energy models using $\sqrt{s} = 13$ TeV pp collision data collected by the ATLAS detector," *JHEP* **05** (2019) 142, arXiv:1903.01400 [hep-ex].

[105] R. V. Harlander, S. Liebler, and H. Mantler, "SusHi: A program for the calculation of Higgs production in gluon fusion and bottom-quark annihilation in the Standard Model and the MSSM," *Comput. Phys. Commun.* **184** (2013) 1605–1617, arXiv:1212.3249 [hep-ph].

[106] R. V. Harlander, S. Liebler, and H. Mantler, "SusHi Bento: Beyond NNLO and the heavy-top limit," *Comput. Phys. Commun.* **212** (2017) 239–257, arXiv:1605.03190 [hep-ph]. https://sushi.hepforge.org.

[107] A. Banfi, F. Caola, F. A. Dreyer, P. F. Monni, G. P. Salam, G. Zanderighi, and F. Dulat, "Jet-vetoed Higgs cross section in gluon fusion at N^{3}LO+NNLL with small-R resummation," *JHEP* **04** (2016) 049, arXiv:1511.02886 [hep-ph]. https://jetvheto.hepforge.org/.

[108] M. Spira, A. Djouadi, D. Graudenz, and P. M. Zerwas, "Higgs boson production at the LHC," *Nucl. Phys. B* **453** (1995) 17–82, arXiv:hep-ph/9504378.

[109] U. Baur and E. Glover, "Higgs Boson Production at Large Transverse Momentum in Hadronic Collisions," *Nucl. Phys. B* **339** (1990) 38–66.

[110] G. Corcella, I. Knowles, G. Marchesini, S. Moretti, K. Odagiri, P. Richardson, M. Seymour, and B. Webber, "HERWIG 6: An Event generator for hadron

emission reactions with interfering gluons (including supersymmetric processes)," *JHEP* **01** (2001) 010, arXiv:hep-ph/0011363.

[111] J. F. Gunion and H. E. Haber, "The CP conserving two Higgs doublet model: The Approach to the decoupling limit," *Phys. Rev. D* **67** (2003) 075019, arXiv:hep-ph/0207010.

[112] A. Banfi, A. Bond, A. Martin, and V. Sanz, "Digging for Top Squarks from Higgs data: from signal strengths to differential distributions," *JHEP* **11** (2018) 171, arXiv:1806.05598 [hep-ph].

[113] A. Banfi, B. M. Dillon, W. Ketaiam, and S. Kvedaraite, "Composite Higgs at high transverse momentum," *JHEP* **01** (2020) 089, arXiv:1905.12747 [hep-ph].

[114] S. Buehler and C. Duhr, "CHAPLIN - Complex Harmonic Polylogarithms in Fortran," *Comput. Phys. Commun.* **185** (2014) 2703–2713, arXiv:1106.5739 [hep-ph]. https://chaplin.hepforge.org/.

[115] A. Alloul, N. D. Christensen, C. Degrande, C. Duhr, and B. Fuks, "FeynRules 2.0 - A complete toolbox for tree-level phenomenology," *Comput. Phys. Commun.* **185** (2014) 2250–2300, arXiv:1310.1921 [hep-ph].

[116] T. Hahn, "Generating Feynman diagrams and amplitudes with FeynArts 3," *Comput. Phys. Commun.* **140** (2001) 418–431, arXiv:hep-ph/0012260. http://www.feynarts.de.

[117] R. Mertig, M. Bohm, and A. Denner, "FEYN CALC: Computer algebraic calculation of Feynman amplitudes," *Comput. Phys. Commun.* **64** (1991) 345–359.

[118] V. Shtabovenko, R. Mertig, and F. Orellana, "New Developments in FeynCalc 9.0" *Comput. Phys. Commun.* **207** (2016) 432–444, arXiv:1601.01167 [hep-ph].

[119] V. Shtabovenko, R. Mertig, and F. Orellana, "FeynCalc 9.3: New features and improvements," *Comput. Phys. Commun.* **256** (2020) 107478, arXiv:2001.04407 [hep-ph]. https://feyncalc.github.io.

[120] I. Brivio, M. Gavela, L. Merlo, K. Mimasu, J. No, R. del Rey, and V. Sanz, "ALPs Effective Field Theory and Collider Signatures," *Eur. Phys. J. C* **77** no. 8, (2017) 572, arXiv:1701.05379 [hep-ph]. https://feynrules.irmp.ucl.ac.be/wiki/ALPsEFT.

[121] N. Kauer, A. Lind, P. Maierhöfer, and W. Song, "Higgs interference effects at the one-loop level in the 1-Higgs-Singlet extension of the Standard Model," *JHEP* **07** (2019) 108, arXiv:1905.03296 [hep-ph].

[122] https://github.com/alexander-lind/gghtt.

[123] T. Binoth and J. J. van der Bij, "Influence of strongly coupled, hidden scalars on Higgs signals," *Z. Phys. C* **75** (1997) 17–25, arXiv:hep-ph/9608245.

[124] R. M. Schabinger and J. D. Wells, "A Minimal spontaneously broken hidden sector and its impact on Higgs boson physics at the large hadron collider," *Phys. Rev. D* **72** (2005) 093007, arXiv:hep-ph/0509209.

[125] B. Patt and F. Wilczek, "Higgs-field portal into hidden sectors," arXiv:hep-ph/0605188.

[126] M. Bowen, Y. Cui, and J. D. Wells, "Narrow trans-TeV Higgs bosons and H —> hh decays: Two LHC search paths for a hidden sector Higgs boson," *JHEP* **03** (2007) 036, arXiv:hep-ph/0701035.

[127] V. Barger, P. Langacker, M. McCaskey, M. J. Ramsey-Musolf, and G. Shaughnessy, "LHC Phenomenology of an Extended Standard Model with a Real Scalar Singlet," *Phys. Rev. D* **77** (2008) 035005, arXiv:0706.4311 [hep-ph].

[128] V. Barger, P. Langacker, M. McCaskey, M. Ramsey-Musolf, and G. Shaughnessy, "Complex Singlet Extension of the Standard Model," *Phys. Rev. D* **79** (2009) 015018, arXiv:0811.0393 [hep-ph].

[129] G. Bhattacharyya, G. C. Branco, and S. Nandi, "Universal Doublet-Singlet Higgs Couplings and phenomenology at the CERN Large Hadron Collider," *Phys. Rev. D* **77** (2008) 117701, arXiv:0712.2693 [hep-ph].

[130] S. Dawson and W. Yan, "Hiding the Higgs Boson with Multiple Scalars," *Phys. Rev. D* **79** (2009) 095002, arXiv:0904.2005 [hep-ph].

[131] S. Bock, R. Lafaye, T. Plehn, M. Rauch, D. Zerwas, and P. M. Zerwas, "Measuring Hidden Higgs and Strongly-Interacting Higgs Scenarios," *Phys. Lett. B* **694** (2011) 44–53, arXiv:1007.2645 [hep-ph].

[132] P. J. Fox, D. Tucker-Smith, and N. Weiner, "Higgs friends and counterfeits at hadron colliders," *JHEP* **06** (2011) 127, arXiv:1104.5450 [hep-ph].

[133] C. Englert, T. Plehn, D. Zerwas, and P. M. Zerwas, "Exploring the Higgs portal," *Phys. Lett. B* **703** (2011) 298–305, arXiv:1106.3097 [hep-ph].

[134] C. Englert, J. Jaeckel, E. Re, and M. Spannowsky, "Evasive Higgs Maneuvers at the LHC," *Phys. Rev. D* **85** (2012) 035008, arXiv:1111.1719 [hep-ph].

[135] B. Batell, S. Gori, and L.-T. Wang, "Exploring the Higgs Portal with 10/fb at the LHC," *JHEP* **06** (2012) 172, arXiv:1112.5180 [hep-ph].

[136] C. Englert, T. Plehn, M. Rauch, D. Zerwas, and P. M. Zerwas, "LHC: Standard Higgs and Hidden Higgs," *Phys. Lett. B* **707** (2012) 512–516, arXiv:1112.3007 [hep-ph].

[137] R. S. Gupta and J. D. Wells, "Higgs boson search significance deformations due to mixed-in scalars," *Phys. Lett. B* **710** (2012) 154–158, arXiv:1110.0824 [hep-ph].

[138] M. J. Dolan, C. Englert, and M. Spannowsky, "New Physics in LHC Higgs boson pair production," *Phys. Rev. D* **87** no. 5, (2013) 055002, arXiv:1210.8166 [hep-ph].

[139] B. Batell, D. McKeen, and M. Pospelov, "Singlet Neighbors of the Higgs Boson," *JHEP* **10** (2012) 104, arXiv:1207.6252 [hep-ph].

[140] J. M. No and M. Ramsey-Musolf, "Probing the Higgs Portal at the LHC Through Resonant di-Higgs Production," *Phys. Rev. D* **89** no. 9, (2014) 095031, arXiv:1310.6035 [hep-ph].

[141] R. Coimbra, M. O. P. Sampaio, and R. Santos, "ScannerS: Constraining the phase diagram of a complex scalar singlet at the LHC," *Eur. Phys. J. C* **73** (2013) 2428, arXiv:1301.2599 [hep-ph].

[142] S. Profumo, M. J. Ramsey-Musolf, C. L. Wainwright, and P. Winslow, "Singlet-catalyzed electroweak phase transitions and precision Higgs boson studies," *Phys. Rev. D* **91** no. 3, (2015) 035018, arXiv:1407.5342 [hep-ph].

[143] H. E. Logan, "Hiding a Higgs width enhancement from off-shell gg(→h*)→ZZ measurements," *Phys. Rev. D* **92** no. 7, (2015) 075038, arXiv:1412.7577 [hep-ph].

[144] C.-Y. Chen, S. Dawson, and I. M. Lewis, "Exploring resonant di-Higgs boson production in the Higgs singlet model," *Phys. Rev. D* **91** no. 3, (2015) 035015, arXiv:1410.5488 [hep-ph].

[145] R. Costa, A. P. Morais, M. O. P. Sampaio, and R. Santos, "Two-loop stability of a complex singlet extended Standard Model," *Phys. Rev. D* **92** (2015) 025024, arXiv:1411.4048 [hep-ph].

[146] A. Falkowski, C. Gross, and O. Lebedev, "A second Higgs from the Higgs portal," *JHEP* **05** (2015) 057, arXiv:1502.01361 [hep-ph].

[147] V. Martín Lozano, J. M. Moreno, and C. B. Park, "Resonant Higgs boson pair production in the $hh \to b\bar{b}\,WW \to b\bar{b}\ell^+\nu\ell^-\overline{\nu}$ decay channel," *JHEP* **08** (2015) 004, arXiv:1501.03799 [hep-ph].

[148] S. Kanemura, M. Kikuchi, and K. Yagyu, "Radiative corrections to the Higgs boson couplings in the model with an additional real singlet scalar field," *Nucl. Phys. B* **907** (2016) 286–322, arXiv:1511.06211 [hep-ph].

[149] S. Kanemura, M. Kikuchi, and K. Yagyu, "One-loop corrections to the Higgs self-couplings in the singlet extension," *Nucl. Phys. B* **917** (2017) 154–177, arXiv:1608.01582 [hep-ph].

[150] S. Kanemura, M. Kikuchi, K. Sakurai, and K. Yagyu, "H-COUP: a program for one-loop corrected Higgs boson couplings in non-minimal Higgs sectors," *Comput. Phys. Commun.* **233** (2018) 134–144, arXiv:1710.04603 [hep-ph].

[151] I. M. Lewis and M. Sullivan, "Benchmarks for Double Higgs Production in the Singlet Extended Standard Model at the LHC," *Phys. Rev. D* **96** no. 3, (2017) 035037, arXiv:1701.08774 [hep-ph].

[152] J. A. Casas, D. G. Cerdeño, J. M. Moreno, and J. Quilis, "Reopening the Higgs portal for single scalar dark matter," *JHEP* **05** (2017) 036, arXiv:1701.08134 [hep-ph].

[153] L. Altenkamp, M. Boggia, and S. Dittmaier, "Precision calculations for $h \to WW/ZZ \to 4$ fermions in a Singlet Extension of the Standard Model with Prophecy4f," *JHEP* **04** (2018) 062, arXiv:1801.07291 [hep-ph].

[154] G. M. Pruna and T. Robens, "Higgs singlet extension parameter space in the light of the LHC discovery," *Phys. Rev. D* **88** no. 11, (2013) 115012, arXiv:1303.1150 [hep-ph].

[155] T. Robens and T. Stefaniak, "Status of the Higgs Singlet Extension of the Standard Model after LHC Run 1," *Eur. Phys. J. C* **75** (2015) 104, arXiv:1501.02234 [hep-ph].

[156] T. Robens and T. Stefaniak, "LHC Benchmark Scenarios for the Real Higgs Singlet Extension of the Standard Model," *Eur. Phys. J. C* **76** no. 5, (2016) 268, arXiv:1601.07880 [hep-ph].

[157] A. Ilnicka, T. Robens, and T. Stefaniak, "Constraining Extended Scalar Sectors at the LHC and beyond," *Mod. Phys. Lett. A* **33** no. 10n11, (2018) 1830007, arXiv:1803.03594 [hep-ph].

[158] **ATLAS** Collaboration, M. Aaboud *et al.*, "Search for Heavy Higgs Bosons A/H Decaying to a Top Quark Pair in pp Collisions at $\sqrt{s} = 8$ TeV with the ATLAS Detector," *Phys. Rev. Lett.* **119** no. 19, (2017) 191803, arXiv:1707.06025 [hep-ex].

[159] **ATLAS** Collaboration, M. Aaboud *et al.*, "Search for heavy particles decaying into top-quark pairs using lepton-plus-jets events in proton–proton collisions at $\sqrt{s} = 13$ TeV with the ATLAS detector," *Eur. Phys. J. C* **78** no. 7, (2018) 565, arXiv:1804.10823 [hep-ex].

[160] N. Kauer and G. Passarino, "Inadequacy of zero-width approximation for a light Higgs boson signal," *JHEP* **08** (2012) 116, arXiv:1206.4803 [hep-ph].

[161] D. Dicus, A. Stange, and S. Willenbrock, "Higgs decay to top quarks at hadron colliders," *Phys. Lett. B* **333** (1994) 126–131, arXiv:hep-ph/9404359.

[162] W. Bernreuther, P. Galler, C. Mellein, Z. G. Si, and P. Uwer, "Production of heavy Higgs bosons and decay into top quarks at the LHC," *Phys. Rev. D* **93** no. 3, (2016) 034032, arXiv:1511.05584 [hep-ph].

[163] B. Hespel, F. Maltoni, and E. Vryonidou, "Signal background interference effects in heavy scalar production and decay to a top-anti-top pair," *JHEP* **10** (2016) 016, arXiv:1606.04149 [hep-ph].

[164] W. Bernreuther, P. Galler, Z.-G. Si, and P. Uwer, "Production of heavy Higgs bosons and decay into top quarks at the LHC. II: Top-quark polarization and spin correlation effects," *Phys. Rev. D* **95** no. 9, (2017) 095012, arXiv:1702.06063 [hep-ph].

[165] M. Carena and Z. Liu, "Challenges and opportunities for heavy scalar searches in the $t\bar{t}$ channel at the LHC," *JHEP* **11** (2016) 159, arXiv:1608.07282 [hep-ph].

[166] A. Djouadi, J. Ellis, A. Popov, and J. Quevillon, "Interference effects in $t\bar{t}$ production at the LHC as a window on new physics," *JHEP* **03** (2019) 119, arXiv:1901.03417 [hep-ph].

[167] **LHC Higgs Cross Section Working Group** Collaboration, J. R. Andersen *et al.*, "Handbook of LHC Higgs Cross Sections: 3. Higgs Properties," arXiv:1307.1347 [hep-ph].

[168] R. Harlander and P. Kant, "Higgs production and decay: Analytic results at next-to-leading order QCD," *JHEP* **12** (2005) 015, arXiv:hep-ph/0509189.

[169] A. Djouadi, M. Spira, and P. M. Zerwas, "QCD corrections to hadronic Higgs decays," *Z. Phys. C* **70** (1996) 427–434, arXiv:hep-ph/9511344.

[170] D. Buarque Franzosi, E. Vryonidou, and C. Zhang, "Scalar production and decay to top quarks including interference effects at NLO in QCD in an EFT approach," *JHEP* **10** (2017) 096, arXiv:1707.06760 [hep-ph].

[171] K. Kudashkin, K. Melnikov, and C. Wever, "Two-loop amplitudes for processes $gg \to Hg, qg \to Hq$ and $q\bar{q} \to Hg$ at large Higgs transverse momentum," *JHEP* **02** (2018) 135, arXiv:1712.06549 [hep-ph].

[172] A. Denner, S. Dittmaier, and M. Roth, "Nonfactorizable photonic corrections to e+ e- —> W W —> four fermions," *Nucl. Phys. B* **519** (1998) 39–84, arXiv:hep-ph/9710521.

[173] W. Beenakker, F. A. Berends, and A. P. Chapovsky, "One loop QCD interconnection effects in pair production of top quarks," *Phys. Lett. B* **454** (1999) 129–136, arXiv:hep-ph/9902304.

[174] V. S. Fadin, V. A. Khoze, and A. D. Martin, "How suppressed are the radiative interference effects in heavy instable particle production?," *Phys. Lett. B* **320** (1994) 141–144, arXiv:hep-ph/9309234.

[175] A. van Hameren, "Kaleu: A General-Purpose Parton-Level Phase Space Generator," arXiv:1003.4953 [hep-ph].

[176] M. Czakon, C. G. Papadopoulos, and M. Worek, "Polarizing the Dipoles," *JHEP* **08** (2009) 085, arXiv:0905.0883 [hep-ph].

[177] A. Denner, S. Dittmaier, and L. Hofer, "Collier: a fortran-based Complex One-Loop LIbrary in Extended Regularizations," *Comput. Phys. Commun.* **212** (2017) 220–238, arXiv:1604.06792 [hep-ph].

[178] A. van Hameren, "OneLOop: For the evaluation of one-loop scalar functions," *Comput. Phys. Commun.* **182** (2011) 2427–2438, arXiv:1007.4716 [hep-ph].

[179] E. Bagnaschi, G. Degrassi, P. Slavich, and A. Vicini, "Higgs production via gluon fusion in the POWHEG approach in the SM and in the MSSM," *JHEP* **02** (2012) 088, arXiv:1111.2854 [hep-ph].

[180] F. Maltoni, "Basics of QCD for the LHC: pp $\to$ H + X as a case study," in *2011 European School of High-Energy Physics*. 2014. https://cds.cern.ch/record/2008764.

[181] U. Aglietti, R. Bonciani, G. Degrassi, and A. Vicini, "Analytic Results for Virtual QCD Corrections to Higgs Production and Decay," *JHEP* **01** (2007) 021, arXiv:hep-ph/0611266.

[182] **LHC Higgs Cross Section Working Group** Collaboration, D. de Florian *et al.*, "Handbook of LHC Higgs Cross Sections: 4. Deciphering the Nature of the Higgs Sector," arXiv:1610.07922 [hep-ph].

[183] J. Butterworth *et al.*, "PDF4LHC recommendations for LHC Run II," *J. Phys. G* **43** (2016) 023001, arXiv:1510.03865 [hep-ph].

[184] N. D. Christensen and C. Duhr, "FeynRules - Feynman rules made easy," *Comput. Phys. Commun.* **180** (2009) 1614–1641, arXiv:0806.4194 [hep-ph].

[185] C. Degrande, C. Duhr, B. Fuks, D. Grellscheid, O. Mattelaer, and T. Reiter, "UFO - The Universal FeynRules Output," *Comput. Phys. Commun.* **183** (2012) 1201–1214, arXiv:1108.2040 [hep-ph].

[186] R. Vogt, "The Usage of the K factor in heavy ion physics," *Acta Phys. Hung. A* **17** (2003) 75, arXiv:hep-ph/0207359.

[187] R. J. Barlow, *Statistics: A Guide to the Use of Statistical Methods in the Physical Sciences*. Wiley, 12, 1993.

[188] **ATLAS** Collaboration, "Luminosity determination in pp collisions at $\sqrt{s} = 13$ TeV using the ATLAS detector at the LHC,".

[189] I. Zurbano Fernandez *et al.*, "High-Luminosity Large Hadron Collider (HL-LHC): Technical design report,".

[190] **ATLAS** Collaboration, M. Aaboud *et al.*, "Measurements of gluon-gluon fusion and vector-boson fusion Higgs boson production cross-sections in the $H \to WW^* \to e\nu\mu\nu$ decay channel in pp collisions at $\sqrt{s} = 13$ TeV with the ATLAS detector," *Phys. Lett. B* **789** (2019) 508–529, arXiv:1808.09054 [hep-ex].

[191] **CMS** Collaboration, A. M. Sirunyan *et al.*, "Measurements of the Higgs boson width and anomalous HVV couplings from on-shell and off-shell production in the four-lepton final state," *Phys. Rev. D* **99** no. 11, (2019) 112003, arXiv:1901.00174 [hep-ex].

[192] G. Bevilacqua, H. B. Hartanto, M. Kraus, T. Weber, and M. Worek, "Off-shell vs on-shell modelling of top quarks in photon associated production," *JHEP* **03** (2020) 154, arXiv:1912.09999 [hep-ph].

[193] J. M. Campbell, R. K. Ellis, and F. Tramontano, "Single top production and decay at next-to-leading order," *Phys. Rev. D* **70** (2004) 094012, arXiv:hep-ph/0408158.

[194] K. Melnikov, M. Schulze, and A. Scharf, "QCD corrections to top quark pair production in association with a photon at hadron colliders," *Phys. Rev. D* **83** (2011) 074013, arXiv:1102.1967 [hep-ph].

[195] **Particle Data Group** Collaboration, M. Tanabashi *et al.*, "Review of Particle Physics," *Phys. Rev. D* **98** no. 3, (2018) 030001.

[196] **CMS** Collaboration, V. Khachatryan *et al.*, "Measurements of t t-bar spin correlations and top quark polarization using dilepton final states in pp collisions at sqrt(s) = 8 TeV," *Phys. Rev. D* **93** no. 5, (2016) 052007, arXiv:1601.01107 [hep-ex].

[197] **ATLAS** Collaboration, M. Aaboud *et al.*, "Measurements of top-quark pair spin correlations in the $e\mu$ channel at $\sqrt{s} = 13$ TeV using pp collisions in the ATLAS detector," *Eur. Phys. J. C* **80** no. 8, (2020) 754, arXiv:1903.07570 [hep-ex].

[198] **D0** Collaboration, V. M. Abazov *et al.*, "Measurement of Spin Correlation between Top and Antitop Quarks Produced in $p\bar{p}$ Collisions at $\sqrt{s} = 1.96$ TeV," *Phys. Lett. B* **757** (2016) 199–206, arXiv:1512.08818 [hep-ex].

[199] **CDF** Collaboration, T. Aaltonen *et al.*, "Measurement of $t\bar{t}$ Spin Correlation in $p\bar{p}$ Collisions Using the CDF II Detector at the Tevatron," *Phys. Rev. D* **83** (2011) 031104, arXiv:1012.3093 [hep-ex].

[200] W. Bernreuther, A. Brandenburg, Z. G. Si, and P. Uwer, "Top quark spin correlations at hadron colliders: Predictions at next-to-leading order QCD," *Phys. Rev. Lett.* **87** (2001) 242002, arXiv:hep-ph/0107086.

[201] M. Jezabek and J. H. Kuhn, "Lepton Spectra from Heavy Quark Decay," *Nucl. Phys. B* **320** (1989) 20–44.

[202] A. Czarnecki, M. Jezabek, and J. H. Kuhn, "Lepton Spectra From Decays of Polarized Top Quarks," *Nucl. Phys. B* **351** (1991) 70–80.

[203] S. J. Parke, "Top Quark Spin Correlations - Theory," *Nuovo Cim. C* **035N3** (2012) 111–114, arXiv:1202.2345 [hep-ph].

[204] G. Mahlon and S. J. Parke, "Spin Correlation Effects in Top Quark Pair Production at the LHC," *Phys. Rev. D* **81** (2010) 074024, arXiv:1001.3422 [hep-ph].